5th International Workshop on Photonics applied to Electromagnetic Measurement

PEM 2023

November 27–28, 2023

Hokkaido University, Hokkaido, Japan

Hybrid of on site and web

Technical Digest

https://www.ieice.org/˜pem/link/6_pem2023/pem2023.html

Sponsored by
Technical committee on Photonics-applied Electromagnetic Measurement

IEICE
Communications
Society

Workshop Outline

Dates:

November 27(Mon.)–28(Tue.), 2023 (Hybrid of on site and web)

Venue:

Frontier Research in Applied Sciences Building
Hokkaido University, Hokkaido, Japan

Major Topic Areas:

1. Basic theory/techniques related to PEM
2. Systems for PEM
3. Applications of PEM
4. Competitive/complementary technologies to PEM

Awards:

Student Best Presentation Award
given to a student for outstanding contributed papers presented in the PEM workshop 2023.

PEM Best Paper Award
given to a researcher for outstanding contributed papers presented in the PEM workshop 2023.

Presentation Time (including discussion)**:**

Keynote Address: 45 min.
Invited Talk: 35 min.
Regular Talk: 20 min.

Sponsor:

Technical committee on Photonics-applied Electromagnetic Measurement, IEICE Communications Society

Website:

https://www.ieice.org/~pem/link/6_pem2023/pem2023.html

Workshop Committees

Workshop Chair: Ai-ichiro Sasaki (Kindai University, Japan)

Local Steering Committee: Takashi Hikage (Hokkaido University, Japan)

Finance Chair: Jun Katsuyama (Yokogawa Electric, Japan)

Secretaries: Yuanfeng She (AIST, Japan)
Shota Yamazaki (NICT, Japan)

Technical Program Committee Chair:
Akihisa Tsuchiya (KISTEC, Japan)

Technical Program Committee:
Shitaro Hisatake (Gifu University, Japan)
Atsushi Kanno (Nagoya Institute of Technology, Japan)
Sven Kühn (IT'IS Foundation, ETH Zürich, Switzerland)
Kyung Hyun Park (ETRI, South Korea)
Yuanfeng She (AIST, Japan)
Kimihiro Tajima (NTT Advanced Technology Corp., Japan)
Yoshiki Yanagisawa (High-Tech Corp., Japan)

Advisory Committee：
Qiang Chen (Tohoku University, Japan)
Satoru Kurokawa (AIST, Japan)
Niels Kuster (ETH Zürich, Switzerland)
Hiroshi Murata (Mie University, Japan)
Maya Mizuno (NICT, Japan)
Teruo Onishi (NICT, Japan)

Keynote & Invited Speakers

Keynote Speaker

Prof. Qiang Chen (Tohoku University, Japan)

Qiang Chen received the B.E. degree from Xidian University, Xi'an, China, in 1986, the M.E. and D.E. degrees from Tohoku University, Sendai, Japan, in 1991 and 1994, respectively. He is currently Chair Professor of Electromagnetic Engineering Laboratory with the Department of Communications Engineering, Faculty of Engineering, Tohoku University. His primary research interests include antennas, microwave and millimeter wave, electromagnetic measurement, and computational electromagnetics.

He received the Best Paper Award and Zen-ichi Kiyasu Award from the Institute of Electronics, Information and Communication Engineers (IEICE). He served as the Chair of IEICE Technical Committee on Photonics-applied Electromagnetic Measurement from 2012 to 2014, the Chair of IEICE Technical Committee on Wireless Power Transfer from 2016 to 2018, the Chair of IEEE Antennas and Propagation Society Tokyo Chapter from 2017 to 2018, the Chair of IEICE Technical Committee on Antennas and Propagation from 2019 to 2021. IEICE Fellow.

Invited Speaker

Dr. Takahiro Kaji (NICT, Japan)

Takahiro Kaji received the Ph. D. degree in engineering from Osaka University in 2009. In 2009, he joined National Institute of Information and Communications Technology (NICT) after working as a specially appointed assistant professor at Osaka University. From 2015 to 2022, he was a senior researcher at NICT. Since 2023, he has been a research manager at NICT. He was co-recipient of the Maejima Hisoka Award in 2023. He is engaged in research and development of ultra-high-speed wireless-optical signal conversion devices using electro-optic polymers.

Invited Speaker

Prof. Ikufumi Katayama (Yokohama National University, Japan)

Ikufumi Katayama earned his PhD of Science from Kyoto University 2006, and studied broadband terahertz time-domain spectroscopy in Osaka University as an assistant professor. He then moved to Yokohama National University in 2007, where he is now enrolled as a professor in the department of physics, graduate school of engineering science. His research especially focuses on visualizing terahertz waveforms using various kinds of singleshot spectroscopy, and on demonstrating observation of terahertz radiations from electronic devices and laser ablation processes. He also develops ultrafast coherent phonon spectroscopy and the terahertz scanning tunneling microscopes to reveal ultrafast and nanoscale dynamics of materials.

Invited Speaker

Dr. Sven Kühn (IT'IS Foundation, Switzerland)

Sven Kühn received his Dipl. Ing. (MSc) in Information and Communication Technologies from Chemnitz University of Technology, Germany, in 2004 and his Ph.D. from the Swiss Federal Institute of Technology (ETH Zurich), Switzerland, in 2009.

Sven joined Schmid & Partners Engineering AG (SPEAG) in 2009 as the Head of Sensor Technologies. During his tenure, he played a crucial role in introducing the TDS sensor platform to the market and developed the ICEy near-field scanning system. In 2011, he assumed leadership of the hardware R&D team at SPEAG.

Since 2022, Sven has been Director of HW R&D at SPEAG. In this role, he oversees the hardware research and development efforts, driving innovation within the company. Additionally, he serves as the technical manager of the ISO17025-accredited calibration laboratory, ensuring adherence to the highest standards.

Invited Speaker

Prof. Niels Kuster (IT'IS Foundation, ETH Zurich, Switzerland)

Niels Kuster is the founder and Director of the Foundation for Research on Information Technologies in Society (IT’IS) in Zurich, Switzerland, and Associate Professor of the Department of Information Technology and Electrical Engineering at Swiss Federal Institute of Technology (ETH) in Zurich. His research covers many aspects of electromagnetics and computational life sciences, and focus, in particular, on the modeling of both internal and external physical factors that affect human physiology. These include electromagnetic fields (e.g. MR safety assessments), tissue heating and cooling (e.g. hyperthermia and ablation), acoustics in biology (e.g. focused ultrasound/pressure waves), biofluid dynamics (e.g. blood flow and aneurysm), biomechanics (e.g. bone, ligaments, and arterial walls), and dynamic tissue models (e.g. nerve models and tumor growth).

Kuster founded several spin-off companies to convert the most promising research results into high-quality commercial technologies, products, and services, and to provide researchers with a platform for innovative and productive research to develop and commercially exploit their knowledge. He has published over 200 peer-reviewed publications on measurement techniques, computational electromagnetics, dosimetry, exposure assessments, and bioexperimentation. He is a member of several standardization bodies and serves as a consultant on the safety of mobile communications for government agencies around the globe.

Invited Speaker

Prof. Hiroshi Murata (Mie University, Japan)

Hiroshi Murata received the D.Eng. degree in electrical engineering from Osaka University in 1998 for studies on the nonlinear optical waveguides and their applications to all-optical functional devices. In 1991, he joined the Department of Electrical Engineering, Faculty of Engineering Science, Osaka University. In 2018, he moved to the Area of Electric and Electronic Engineering, Graduate School of Engineering, Mie University, where currently he is a Professor.

His research interests include integrated optics, nonlinear optics, and microwave photonics. He is the author or co-author of more than 260 scientific publications in these areas and also holds several patents.

He was the Technical Program Committee Chair of MWP/APMP 2014, an Associate Editor of the IEICE Electronics Express in 2009-2012, and the Guest Editors of the Journal Advances in OptoElectronics in 2007-2008 and the IEICE Transaction on Electronics in 2014-2015. He is also a member of IEEE Photonics and MTT societies, EuMA, OSA, OSJ, JSAP and IEICE of Japan.

He was the recipient of the 35th European Microwave Conference (EuMC) Microwave Prize in 2005.

Invited Speaker

Prof. Motoyuki Sato (Tohoku University, Japan)

Motoyuki Sato received the B.E., M.E degrees, and Dr. Eng. degree in information engineering from Tohoku University, Sendai, Japan, in 1980, 1982 and 1985, respectively. Since 1997 he has been a professor at Tohoku University until his retirement in 2023. He was a distinguished professor of Tohoku University 2007-2011, the director of Center for Northeast Asian Studies, Tohoku University 2009-2013.

His current interests include transient electromagnetics and antennas, radar polarimetry, ground penetrating radar (GPR), borehole radar, electromagnetic induction sensing, GB-SAR and MIMO radar systems. He developed GPR sensors ALIS for humanitarian demining, and they are used in mine affected countries including Cambodia and Ukraine.

He served the technical chair of GPR1996 in Sendai and the general chair of IGARSS2011 Sendai-Vancouver.

PEM 2023 Workshop Program

Monday, November 27, 2023

11:00 **Opening Remarks**
Ai-ichiro Sasaki (Kindai Univ.)

Session 1 Nov. 27 (Mon.) 11:10–11:55

Chair: Ai-ichiro Sasaki (Kindai Univ.)

M-1 **[Keynote Address]**
11:10 **Development of Reconfigurable Reflectarray Antennas**
Qiang Chen (Tohoku Univ.)

11:55–13:10 **Lunch break**

Session 2 Nov. 27 (Mon.) 11:10–11:55

Chair: Shota Yamazaki (NICT)

M-2 **[Invited Talk]**
13:10 **Realtime Terahertz Waveform Detection Using Chirped Pulse Upconversion Spectroscopy**
○Ikufumi Katayama (Yokohama National Univ.), Ryo TAMAKI (Yokohama National Univ./KISTEC)

M-3 **[Regular Talk]**
13:45 **Design of Sub-THz Signal Generation Device Based on Optical Difference Frequency Generation Using T-Branch $LiTaO_3$ and Al_2O_3 Rectangular Waveguide**
○Ken Paramayudha, Yui Otagaki, Hiroshi Murata (Mie Univ.)

M-4 **[Regular Talk]**
14:05 **Wireless Terminal Localization Experiment Using Radio-over-Fiber Links**
Hiroto Terai, Yui Otagaki, ○Hiroshi Murata (Mie Univ.)

14:25–14:40 **Coffee break**

Session 3　Nov. 27 (Mon.) 14:40–15:55

Chair: Kimihiro Tajima (NTT-AT)

M-5　**[Invited Talk]**

14:40　**EM Measurement through Optical Fiber**

–Applications to Archaeological Survey of the Pyramid and Humanitarian demining–

Motoyuki Sato (Tohoku Univ.)

M-6　**[Regular Talk]**

15:15　**Non-invasive temperature measurement of the porcine cornea-equivalent phantom in THz frequency band**

○Shota Yamazaki, Maya Mizuno, Tomoaki Nagaoka (NICT)

M-7　**[Regular Talk]**

15:35　**Fundamental Study on THz Irradiation Power Control Using Wire Grids**

○Maya Mizuno (NICT), Yoshinori Tatematsu, Masafumi Fukunari (Univ. of Fukui), Shota Yamazaki (NICT), Yukihisa Suzuki, Atsushi Sugimoto (TMU), Tomoaki Nagaoka (NICT)

15:55–16:10　**Coffee break**

Session 4　Nov. 27 (Mon.) 16:10–17:10

Chair: Maya Mizuno (NICT)

M-8　**[Regular Talk]**

16:10　**Interference-Induced Voltage Measurement for EMI Assessment of Implantable Medical Devices by Exposure to 5G Frequency Radio Wave using Electro-Optical Converter**

○Funa Tsumura, Shuhei Waki, Takashi Hikage(Hokkaido Univ.), Yoshitoshi Tochikura, Takahiro Iyama, Junji Higashiyama, Yasunori Suzuki (NTT DOCOMO INC.)

M-9　**[Regular Talk]**

16:30　**Spatial Synthetic Vertical Local Exposure System to Investigate Thermo-Physiological and Cellular Function Changes Induced by Millimeter-Wave Exposure**

○Kaito Sugimura, Sakura Tsuruga, Takashi Hikage (Hokkaido Univ.), Hiroshi Masuda, Tatsuya Ishitake (Kurume Univ.), Kun Li (The Univ. of Electro-Communications), Akiko Nagai (Aichi Gakuin Univ.)

M-10　**[Regular Talk]**

16:50　**Comparisons of Averaging Mass of Localized SAR in Estimating Temperature Increase at the Edges of Implanted Metal Plates within the Cellular Radio Frequency Band**

○Shuhei Waki, Funa Tsumura, Takashi Hikage (Hokkaido Univ.), Tomoaki Nagaoka (NICT)

Tuesday, November 28, 2023

Session 5　Nov. 28 (Tue.) 9:30–10:40

Chair: Takashi Hikage (Hokkaido Univ.)

T-1　**[Invited Talk]**

09:30　**Advanced Millimeter-Wave Electro-Optic Modulator Using Antenna-Coupled Electrode –Applications for Precise Field Measurement and Signal Processing–**

Hiroshi Murata (Mie Univ.)

T-2　**[Invited Talk]**

10:05　**Photonic Electromagnetic Sensor Technology from DC to THz**

Sven Kühn, Ninad Chitnis, Niels Kuster (IT'IS Foundation, ETH Zurich)

10:40–10:55　**Coffee break**

Session 6　Nov. 28 (Tue.) 10:55–11:55

Chair: Shuji Taue (Kochi Univ. of Tech.)

T-3　**[Regular Talk]**

10:55　**Electric Field Distribution Measurement of Indoor Local 5G Using SDR Device**

〇Daiki Imai (AGU), Akihisa Tsuchiya, Hideaki Sugama (KISTEC), Osamu Hashimoto, Ryosuke Suga (AGU)

T-4　**[Regular Talk]**

11:15　**Improvement of Prediction Accuracy of Magnetic Field‐Based Positioning with a High‐Isolation Relay Circuit**

〇Kouga Miyaji, Ai-ichiro Sasaki (Kindai Univ.)

T-5　**[Regular Talk]**

11:35　**Development of Magnetic Measurement and Source Localization System with a Drone and AI –Aiming for Magnetic Material Detection–**

〇Yu Takemoto, Sunao Sadahiro, Yoshimi Hatsukade (Kindai Univ.)

11:55–13:10　**Lunch break**

Session 7　Nov. 28 (Tue.) 13:10–14:45

Chair: Akihisa Tsuchiya (KISTEC)

T-6 **[Invited Talk]**

13:10 **Development of Antenna-Coupled Optical Modulators Using Electro-Optic Polymer Waveguides**

Takahiro Kaji (NICT)

T-7 **[Regular Talk]**

13:45 **Measurement of Antenna Radiation Pattern using Single-Cut Method with Optical Fiber**

〇Yuanfeng She, Michitaka Ameya (AIST)

T-8 **[Regular Talk]**

14:05 **Image-Sensor-Based Microwave Electric-Field Imaging System Using $LiNbO_3$ Sensor**

〇Kiyotaka Sasagawa, Ryoma Okada (NAIST), Maya Mizuno (NICT), Hironari Takehara (NAIST), Makito Haruta (NAIST/Chitose Inst. Sci. Tech.), Hiroyuki Tashiro (NAIST/Kyushu Univ.), Jun Ohta (NAIST)

T-9 **[Regular Talk]**

14:25 **36-GHz electric field imaging using an electro-optic imaging system based on polarization CMOS image sensor**

〇Ryoma Okada (NAIST), Maya Mizuno (NICT), Hironari Takehara (NAIST),
Makito Haruta (NAIST/Chitose Inst. Sci. Tech.), Hiroyuki Tashiro (NAIST/Kyushu Univ.), Jun Ohta, Kiyotaka Sasagawa (NAIST)

Award Ceremony & Closing Remarks　Nov. 28 (Tue.) 14:45–15:05

14:45-14:55 **Award Ceremony**

Akihisa Tsuchiya (KISTEC)

14:55-15:05 **Closing Remarks**

Qiang Chen (Tohoku Univ.)

Contact
Technical committee on Photonics-applied Electromagnetic Measurement
E-mail：pem-executive@mail.ieice.org

Issue date: November 22 2023
IEICE Technical committee on Photonics-applied Electromagnetic Measurement

[Keynote Address] Development of Reconfigurable Reflectarray Antennas

Qiang Chen, Wen Wu, Xianbo Cao, and Xiaotong Li
Department of Communications Engineering, Tohoku University, 980-8579, Sendai, Japan
*Corresponding author: qiang.chen.a5@tohoku.ac.jp

Abstract – This paper reviews the recent development of reconfigurable reflectarray (RRA) antennas, with a focus on addressing challenges related to bandwidth limitations, uncontrollable reflection amplitude across the aperture, and cost constraints in large aperture applications. Three novel designs are introduced to successfully resolve these issues, presenting operating principles and measured performance. The magnetoelectric (ME) dipole based RRA achieves promising performance in gain bandwidth; the introduction of time modulation (TM) technique enhances RRA design, enabling tunability in the amplitude of the reflection coefficient; and the use of liquid crystal (LC) as the substrate, instead of PCB, proves effective in reducing costs in large apertures.

Keywords – Reconfigurable reflectarray (RRA); wideband; time-modulated reflectarray (TMRA); liquid crystal(LC)

1. Introduction

The reconfigurable reflectarray (RRA) antenna is one of the key technology for 5G/B5G wireless communication. However, several challenges hinder its large-scale deployment, including: 1. The conventional RRA suffers from narrow bandwidth. 2. Only phase tuning is available without an amplitude control method for each unit cell. 3. The cost increases dramatically when the physical aperture size and the quantity of unit cell increase, primarily due to the high price of the single PIN diode and large surface PCB. In this paper, three designs are demonstrated to address these issue.

2. 1-bit wideband RRA design

The proposed unit cell consists of two parts: the upper part is an electromagnetic resonant section, which functions as a magnetoelectric (ME) dipole [2], and the lower part is the DC bias circuit, as shown in Fig. 1.

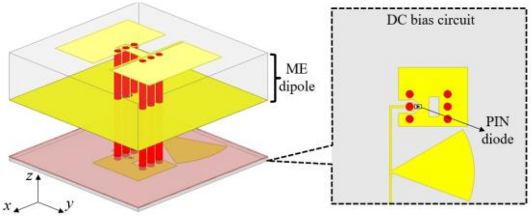

Figure 1. Geometry of the 1-bit wideband RRA unit cell based on ME dipole.

The ME dipole ensures wideband performance in resonance, while frequency independent switching enables 1-bit operation within a broad frequency range. The incident EM wave is received by the ME dipole, and the power is subsequently propagated through the metallic via hole at the center of the ME dipole. The 1-bit function is achieved by switching the via between 'open' and 'short' statuses, which is physically realized by a PIN diode located between the end of via and the surrounding ground. The DC bias circuit is provided by a high impedance microstrip line. This microstrip line includes a metal fan-shaped open stub positioned at a distance of λ/4 from the PIN diode, where λ is the microstrip wavelength corresponding to the center frequency.

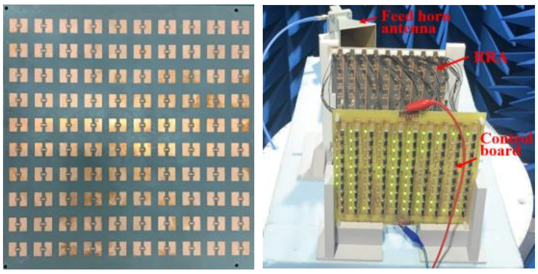

(a) (b)

Figure 2. The wideband RRA prototype (a) Top view (b) Measurement setup

The prototype of the proposed wideband reconfigurable reflectarray (RRA) is fabricated with a 10×10 unit cell configuration, as shown in Fig. 2(a). DC power is supplied by a separate control board equipped with 10×10 switch buttons. Each unit cell is equipped with an LED diode to indicate the PIN diode's operating status, as illustrated in Fig. 2(b). The measured far field pattern is depicted in Fig. 3. The 1-dB gain bandwidth exceeds 30% when the collimation beam scans at 15° in the E-plane, reaching a peak gain of 17.6 dBi at 8.5 GHz.

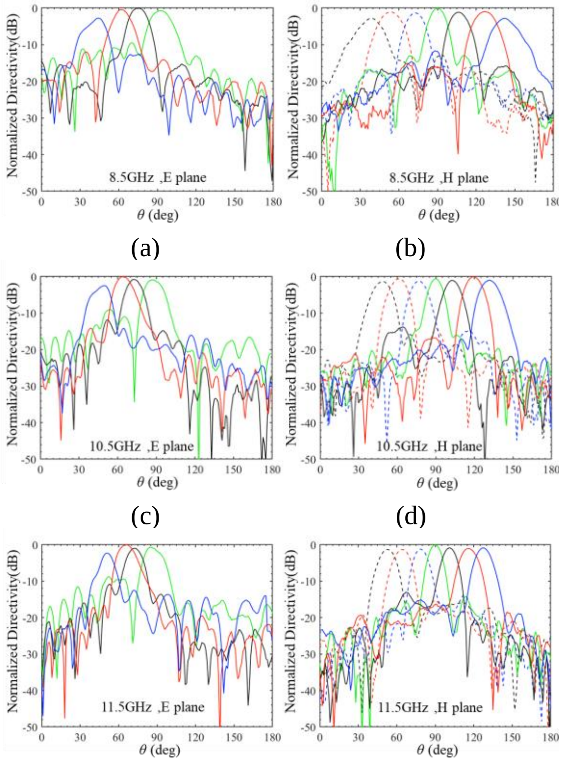

(a) (b)

(c) (d)

(e) (f)

Figure 3. Measured radiation patterns of the proposed array: (a) E-plane at 8.5 GHz, (b) E-plane at 8.5 GHz, and (c) E-plane at 10.5 GHz; and (d) H-plane at 10.5 GHz, (e) H-plane at 11.5 GHz, and (f) H-plane at 11.5 GHz

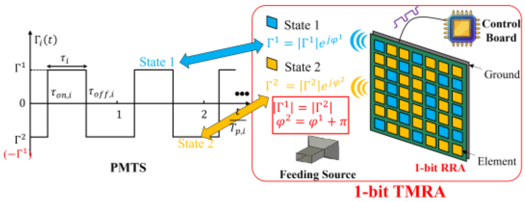

Figure 4. Concept of 1-bit TMRA.

In summary, the proposed 1-bit electrically controlled RRA offers advantage in gain bandwidth based on ME dipole using 2-layer PCB. The collimation beam can dynamically steer up to 45°.

3. 1-bit TMRA design

The time-modulated reflectarray(TMRA) refers to a new type of RRA that flexibly controls the reflection characteristics by varying the reflection coefficients in the time domain according to a specific time sequence to generate the equivalent reflection coefficient in the frequency domain. It is a concept expansion of time-modulated antenna array (TMAA) [3]. Previous studies of TMRA used strong/weak reflection states of RRA to realize high/low logic states of time sequence, which makes them inefficient and impractical in the actual applications. By contrast, we propose a novel and efficient TMRA configuration based on the two strong reflection states with the same amplitudes and opposite phases of the 1-bit RRA. The corresponding relationship between 1-bit TMRA and phase modulation time sequence (PMTS) is shown in Fig. 4.

The corresponding Fourier coefficients of PMTS, which are the equivalent reflection coefficients of each element, can be mathematically expressed as follows:

$$a_{i,h}(t) = \frac{1}{T_{p,i}} \int_0^{T_{p,i}} \Gamma_i(t) e^{-j2\pi h F_{p,i} t}\, dt$$
$$= \begin{cases} 2\tau_i sinc(\pi h \tau_i) e^{-j\pi h(\tau_{off,i}+\tau_{on,i})}, & h \neq 0 \\ 2\tau_i - 1, & h = 0 \end{cases} \qquad (1)$$

It can be found that time modulation (TM) introduces an amplitude control ability at the carrier frequency, and the equivalent amplitude excitation is determined by duration time. Fig. 5(a) shows the structure of 1-bit TMRA element. The PIN diode is

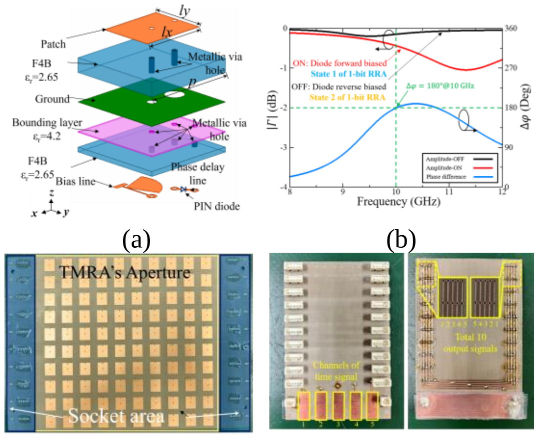

Figure 5. Design of 1-bit TMRA. (a) Element structure. (b) Simulated Γ of element. (c) Photo of 10×10 1-bit TMRA prototype. (d) Photo of designed control board.

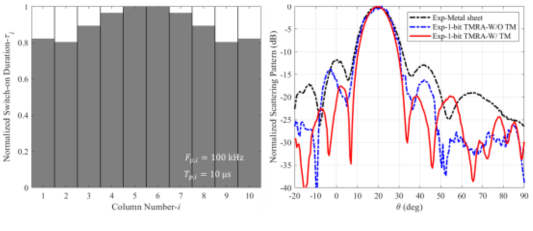

Figure 6. Experimental results. (a) Switch-on duration τ_i. (b) Measured normalized scattering patterns.

inserted to the phase delay line (PDL) and two reflection states can be obtained by forward of reverse bias the diode. By carefully designing the PDL's length and diode's position, two 1-bit reflection states can be realized. The simulated reflection coefficients are shown in Fig. 5(b), it can be found that the 1-bit frequency point is 10 GHz and the amplitudes are almost same. Then, 10×10 1-bit TMRA prototype and control board was designed and fabricated, respectively. The photos are shown in Fig. 5(c)(d).

The scattering patterns were measured in the microwave chamber, where transmitting and receiving antennas were placed in the far-field region of array. Fig. 6(a) shows the duration time distribution for realizing a 20 dB Chebyshev pattern. The dark zone represents diode is forward biased. The measured results are shown in Fig. 6(b). Note that the results of the metal sheet are plotted as a benchmark. It is found that the side-lobe levels (SLLs) are significantly reduced by TM. Specifically, except for the first SLL (2° direction) on the left side of the main beam, the other three SLLs near the main beam are -22.53 dB (-7.5° direction), -19.74 dB (38.5° direction), and -19.74 dB (54.5° direction) respectively. The experimental target of 20 dB Chebyshev pattern is basically achieved.

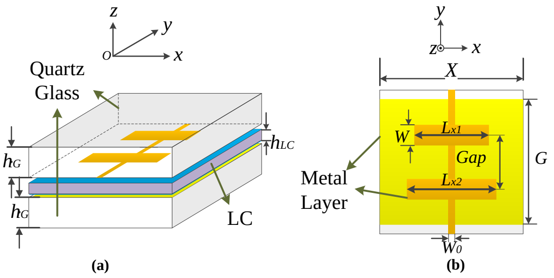

Figure 7. Geometry of the LC RA unit. (a)3D view. (b)Top view.

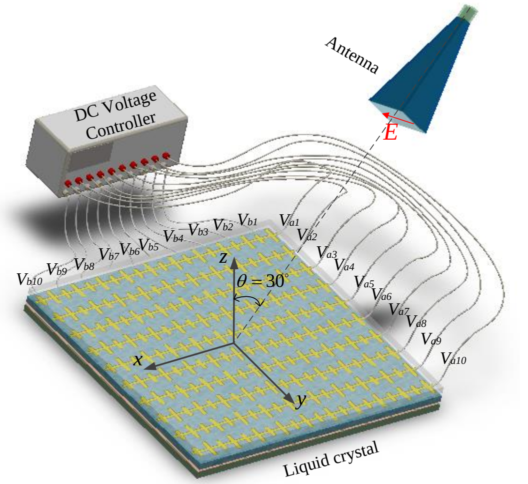

Figure 8. LC RA antenna system.

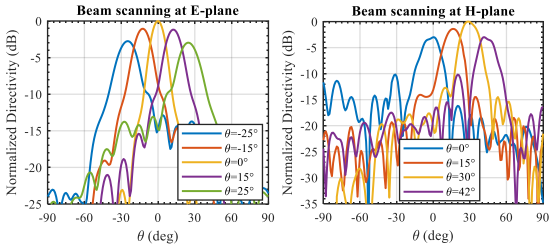

(a) (b)

Figure 9. Steering beams of LC RA.

In summary, the TM function of the proposed 1-bit TMRA is verified by successfully realizing of beam-shaping. Moreover, it can also realize beam-steering function due to the 1-bit RRA structure. Compared to previous TMRA, the proposed 1-bit TMRA is more versatile, higher efficient and more practical.

4. Liquid crystal RA design

The two-finger structure is deployed as patch layer in LC RA unit cell, as shown in Fig. 7. There are five layers in LC RA unit from top to bottom: quartz glass (ε_r = 3.2, tanδ = 0.002), the patch layer, LC, metalized ground layer with a slot, quartz glass. The LC used in the design is LC-BYE7, its material parameters[4] are used as follows: relative permittivity changes from $\varepsilon_{r,\perp}$ = 2.1 to $\varepsilon_{r,//}$ = 3.2, loss tangent varies from tan$\delta_\perp$ = 0.014 to tan$\delta_{//}$ = 0.004.

The LC RA system is shown in Fig. 8, horn antenna is placed offset upon RA. In LC RA, we propose a scheme of electrode connection: the finger structure are connected in one column by bias lines and the grounds are connected in one row, thus the phase of reflected wave from RA can be controlled in two mutually orthogonal directions: when the voltage electrodes connected to the ground are set $V_{b1} = V_{b2} = V_{b3} = \cdots = V_b$, the voltage electrodes form DC voltage module connected to patch layer are set different values V_{a1}, V_{a2}, V_{a3}, $\cdots$, V_{a10}, so the phase of RA element can vary in direction y; if the voltage electrodes connected to the patch layer are the same $V_{a1} = V_{a2} = V_{a3} = \cdots = V_a$, and the discrete ground sections are biased with different voltages V_{b1}, V_{b2}, V_{b3}, $\cdots$, V_{b10}, the phase of RA element will change in direction x.

To achieve beam steering in the H-plane, a progressive phase distribution in the xOz plane is required as the following proposed scheme: all voltage electrodes connected to the patch are set to the same value V_a, while the ground layers are biased with varying voltages V_{b1}, V_{b2}, $\cdots$, V_{b10}. This configuration provides control over the phase of the reflected wave from each column along the x-direction. As a result, beam steering in the H-plane can be achieved, ranging from 0° to 42° relative to the z-axis (see Fig. 9(a)), with a maximum radiation intensity decrease of 3.0 dB. On the other hand, when the electrodes connected to the ground are biased at the same voltage V_b, and the ground layers are biased with varying voltages V_{a1}, V_{a2},…, V_{a10}, orthogonal beam steering is attainable. In this case, the steered beam in the E-plane can cover a range from -30° to 30°.

In summary, a beam-steerable LC RA has been successfully realized. The application of orthogonal bias voltage to the electrodes allows for independent phase control of each unit cell, enabling beam scanning in both the E-plane and H-plane.

Conclusions

Certain bottleneck issues in reconfigurable reflectarray (RRA) design, including bandwidth limitations, amplitude taper control challenges, and cost issues in large aperture dimensions, have been addressed through the introduction of specific solutions. The inclusion of ME dipole elements, time modulation, and the integration of liquid crystal materials have provided effective remedies for these challenges, respectively.

Acknowledgment

The research was supported by the Program on Open Innovation Platform with Enterprises, Research Institute and Academia (OPERA), JST, under Grant JPMJOP1852, and by the Ministry of Internal Affairs and Communications in Japan (JPJ000254).

References

[1] R. Flamini et al., “Toward a Heterogeneous Smart Electromagnetic Environment for Millimeter-Wave Communications: An Industrial Viewpoint,” *IEEE Trans. Antennas Propag*, vol. 70, no. 10, pp. 8898-8910, Oct. 2022.

[2] K.-M. Luk and B. Wu, “The magnetoelectric dipole—A wideband antenna for base stations in mobile communications,” Proc. IEEE, vol. 100, no. 7, pp. 2297–2307, Jul. 2012.

[3] W. Kummer, A. Villeneuve, T. Fong, and F. Terrio, "Ultra-low sidelobes from time-modulated arrays," *IEEE Trans. Antennas Propag*, vol. 11, no. 6, pp. 633-639, 1963.

[4] G. Perez-Palomino et al., "Design and Experimental Validation of Liquid Crystal-Based Reconfigurable Reflectarray Elements With Improved Bandwidth in F-Band," *IEEE Trans. Antennas Propag*, vol. 61, no. 4, pp. 1704-1713, Apr. 2013.

[Invited Talk] Realtime Terahertz Waveform Detection Using Chirped Pulse Upconversion Spectroscopy

Ikufumi KATAYAMA[1*], and Ryo TAMAKI [1,2]
[1] Department of Physics, Yokohama National University, 240-8501 Yokohama,
[2] Kanagawa Institute of Industrial Science and Technology, 243-0435 Ebina, Japan Japan
*Corresponding author: katayama-ikufumi-bm@ynu.ac.jp

Abstract – Terahertz frequency range is one of the frontiers for optical science and technology where applications to high-speed wireless communications, imaging, and materials characterization are considered promising. Although the method to detect waveforms of the terahertz radiation is indispensable for these applications, the realtime detection is still difficult because the detection bandwidth of realtime oscilloscopes that based on the conventional electronics is lower than the terahertz frequency range. Here, we demonstrate the detection of terahertz waveforms using electro-optic sampling method by chirped pulse upconversion spectroscopy with dispersion compensation. We recorded the pulse-to-pulse waveforms of up-converted terahertz signal without significant waveform distortion, demonstrating the promising capability of the method for future terahertz applications.

Keywords – terahertz; singleshot; ultrafast; chirped pulse, upconversion

1. Introduction

Terahertz waves (10^{12} Hz, wavelength: 300 μm, energy: 34 cm^{-1}, 48 meV) are high-frequency electromagnetic waves that are difficult to be detected with conventional electronics because the frequency is much higher than the detection bandwidth [1]. Some high-sensitivity terahertz detectors such as bolometers, Schottky barrier diodes and pyroelectric detectors can detect the intensity of terahertz radiation, but the waveform is still difficult to be measured precisely. For the applications such as the broadband wireless communications, imaging, and materials characterization, it is desired to develop a method to detect the waveform of the terahertz radiation.

One of the promising ways of detecting the terahertz waveform is the use of ultrashort pulsed lasers and the electrooptic (EO) sampling method. In the EO sampling, the terahertz radiation and the probe pulses are simultaneously shined on an EO crystal, and the polarization rotation induced by the electric field of terahertz pulses is measured. However, repeated measurements are required for the observation of the terahertz waveforms because ultrashort probe pulses can only detect the electric field strength at the timing when the probe pulses are shined. It is therefore required to develop a singleshot spectroscopy for realtime detection of the terahertz waveforms using an ultrashort laser pulse and EO sampling [2].

In this work, we developed a new way of detecting the realtime terahertz waveforms by combining the time-encoding technique with chirped pulse upconversion spectroscopy. We measured sum frequency generation between the modulated probe signals and chirped readout pulses whose frequency chirp is adjusted to compensate the chirp for the probe pulses. The method is promising for future terahertz technology because it offers a way of detecting terahertz waveforms in realtime without any significant distortions.

2. Singleshot methods

There are several ways to detect the terahertz waveforms in realtime using ultrashort pulses and EO sampling as shown in Fig. 1. First one (Fig. 1(a)) is to cross the terahertz wave with probe pulses obliquely on the EO crystal [3]. This way the temporal delay between the terahertz pulses and the probe depends on the position at the EO crystal, and therefore, the image of the polarization rotation at the EO crystal induced by the terahertz waves directly

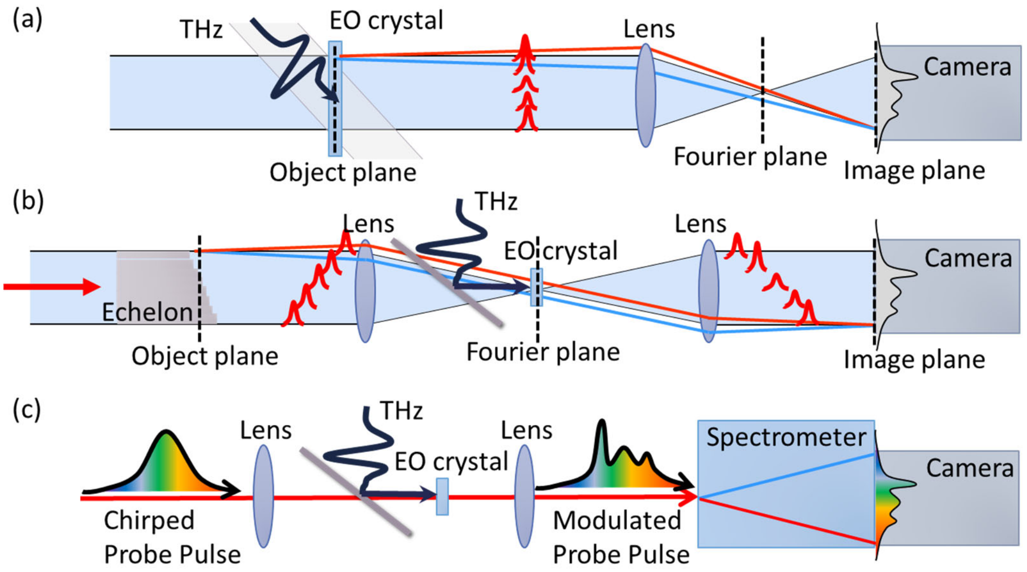

Figure 1. Various types of singleshot terahertz spectroscopy. (a) Oblique crossing method, mapping temporal information to the position on the EO crystal. (b) An echelon prism maps the temporal information to the incident angles to the EO crystal. (c) Chirped probe pulses are used to map the temporal information to the wavelength.

corresponds to the waveform. The drawbacks of this method are the needs for a large single crystal to measure sufficient time window and for an imaging optics and a camera to acquire the polarization rotation image that limits the detection speed of the measurement.

The second way (Fig. 1(b)) is to use a stair-step optics such as dual echelon prisms or reflective echelon mirror to divide the single probe pulse into many probe pulses [4]. This way, we can focus the probe pulses to the EO crystal. The surface of the echelons is imaged onto a camera to precisely obtain the terahertz waveform. However, it is required to align the imaging optics for the measurement and to use an camera, which limits the measurement speed. It is also difficult to change the time window for the measurement because it is determined by the shape of echelon optics used in the experiment.

The third way of realizing the realtime waveform measurement (Fig. 1(c)), which is used in this work, is the use of chirped probe pulse for the detection, which is so-called time-encoding method [5]. In this case, the temporal information is encoded on each wavelength of the probe, and therefore, we can obtain the terahertz waveform by resolving the spectrum of the probe pulses. The probe can be tightly focused on the EO crystal, and the time-window of the measurement is easily tuned by controlling the dispersion of the probe. The spectrum can be obtained either by a spectrometer and a camera, or by the time-stretching method that uses highly dispersive media such as the long optical fiber and a single photodiode. The latter realizes high-repetition measurement.

However, the time-encoding technique suffers from severe signal distortion due to the interference of the signals and the probe pulses. The aim of this work is to reduce the distortion by chirped-pulse up-conversion spectroscopy and to demonstrate the accurate terahertz detection using the proposed method [6].

3. Principle and Experimental setup

The schematic of the method used in this work is summarized in Fig. 2. In the conventional time-encoding technique, we modulate the chirped probe pulses with terahertz waves and the resultant polarization rotation is detected in the spectral domain as shown in Fig. 2(a). In this case, the terahertz modulation forms the sidebands (sum and difference frequency signals) around the chirped probe pulses which will interfere

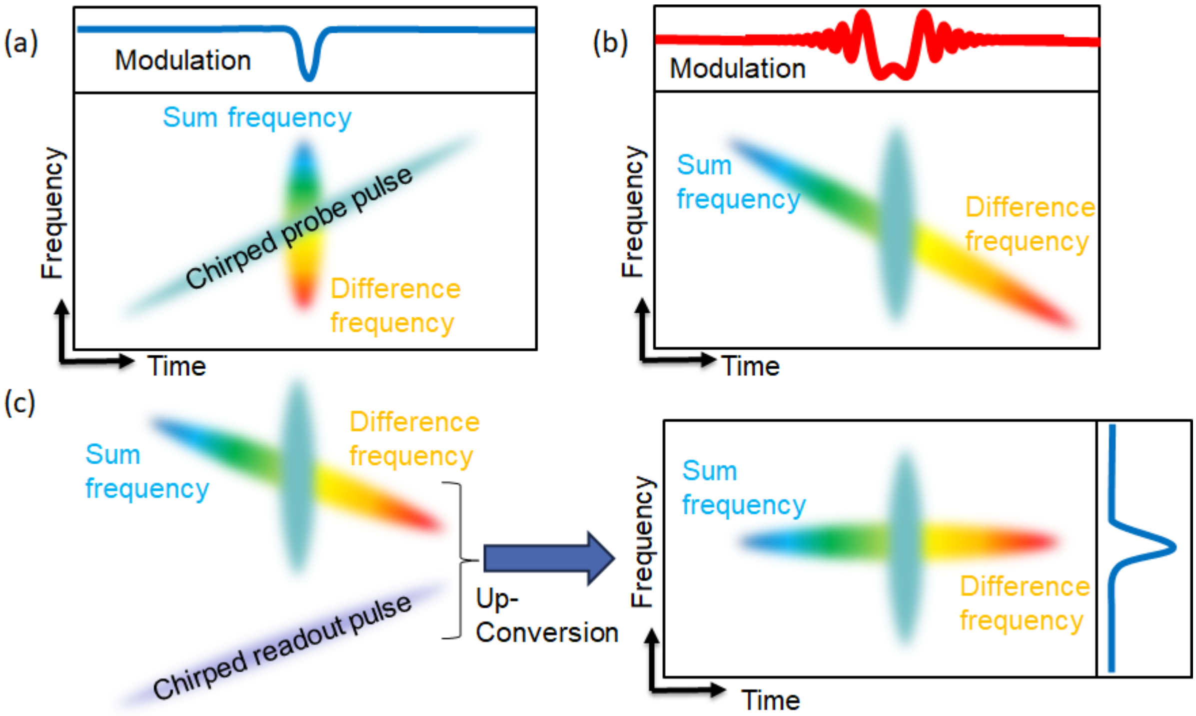

Figure 2. Principle of the chirped pulse upconversion spectroscopy. (a) Time-frequency mapping of the time-encoding technique. Rainbow ellipse is the sideband signals (sum and difference frequency generation) generated by the ultrafast modulation of probe pulses. (b) Probe pulses after the time-encoding and the phase compensation. (c) Time-frequency mapping of the upconverted signal. The phase compensated probe pulse is upconverted with chirped readout pulse to map the modulation to the spectral domain.

with the different spectral components of the original probe pulses. Because of this interference, we see many fringes in the spectra of the probe and the waveform is strongly distorted compared with the original modulation waveforms.

Because of this waveform distortion, the temporal resolution of the time-encoding technique is estimated to be the square root of the product of transfer-limited pulse duration of the probe pulses and the pulse duration of the chirped probe pulses. Thus, if we increase the pulse duration of the probe to expand the time-window of the measurement, it significantly reduces the temporal resolution of the system, limiting the applications of time-encoding technique to spectroscopy.

To reduce this limitation, we inserted the upconversion process before measuring the spectrum of the probe pulses. We first compensate the chirp of the probe pulses as shown in Fig. 2(b), and as a result the phase-compensated modulation signal is oppositely chirped to the chirped probe pulses. Then, sum frequency signal of the phase-compensated probe pulses with the chirped readout pulses is generated by the upconversion process as shown in Fig. 2(c). In the resultant upconverted signal, the modulated signal (sum and difference frequency in Fig. 2(a)) is converted to a single frequency as shown by a rainbow ellipse in Fig. 2(c). By comparing the original modulation and the final up-converted signal, we notice that the temporal and spectral axes are completely flipped. Therefore, the spectral information of the upconverted signal directly corresponds to the temporal information. This method is one of the so-called time lens technique that enables to magnifies the temporal information of the optical pulses.

To implement the concept of the chirped pulse up-conversion spectroscopy with dispersion compensation, we used the experimental setup as shown in Fig. 3. We used a Ti:sapphire regenerative amplifier (1 kHz repetition rate, 2 mJ pulse energy and 800 nm center wavelength) to generate terahertz waves and to detect the waveform

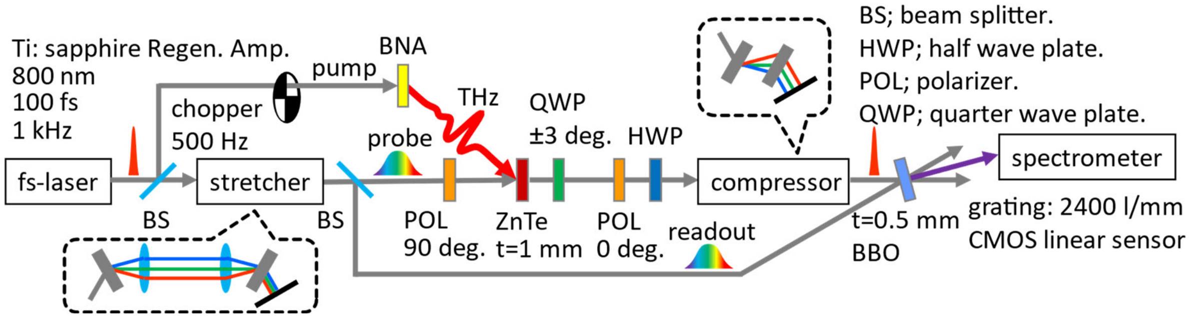

Figure 3. Experimental setup for chirped upconversion spectroscopy with dispersion compensation. Two polarizers before and after the EO crystals are set cross polarized, and phase offset is induced by a QWP crystal to enhance the sensitivity of EO sampling (phase offset method).

in realtime. We prepared the chirped probe pulses using the grating pair stretcher, and the terahertz signal is encoded using a 2-mm-thick ZnTe (110) as an EO crystal. Then the polarization rotated signals are phase compensated by a grating pair compressor and directed to the BBO crystal. The sum frequency signal between the compensated probe pulses and the readout pulses is generated at the BBO crystal the is detected by a home-made spectrometer. Terahertz waves are generated by an organic nonlinear crystal N-benzyl-2-methyl-4-nitroaniline (BNA). To enhance the sensitivity of the terahertz waveforms, we employ the phase offset EO sampling with the offset angle of 3 degrees.

4. Experimental Results

Figure 4(a) shows the experimental result of the chirped pulse up-conversion spectroscopy with the accumulation time of about 1 second. The obtained signals with positive and negative phase offsets are plotted. For comparison, we also plot the observed waveforms obtained by conventional stage scan method as shown in Fig. 4(b). By subtracting the waveform obtained with the positive phase offset by that with the negative phase offset, the precise terahertz waveform can be acquired as shown in Fig. 4(c). The comparison between the waveforms of upconversion spectroscopy and the stage scan method illustrates a good agreement between them, indicating little signal distortion in the chirped pulse upconversion spectroscopy with dispesion compensation.

By applying Fourier transformation to the obtained terahertz waveforms, detected bandwidth of the terahertz waves are almost similar for both methods. Since chirped pulse upconversion spectroscopy bases on the singleshot detection of the terahertz waves, it can be applied to high frequency wireless communications, high-speed imaging, and material characterization.

We can also demonstrate singleshot detection of the terahertz waveform, just by reducing the accumulation time of the measurement. In this case, the noise floor of the waveforms becomes larger, and the minimum detectable electric field strength is in the order of 100 V/cm. This could originate from the pulse-to-pulse fluctuation of the intensity of the probe laser because we acquire the reference spectrum separately in the experiment shown in Fig. 4. This effect will be reduced by taking the reference spectrum simultaneously with the signal, which will further reduce the signal to noise ratio of the measurement.

Finally, one of the important benefit of the chirped pulse upconversion spectroscopy is that the method can be combined with sophisticated fiber technology such as the signal amplification and the time-stretchning methods. For example, if we combine this technique with Yb-doped fiber laser, we could implement whole the setup with fibers, making the terahertz measurement more robust and reliable.

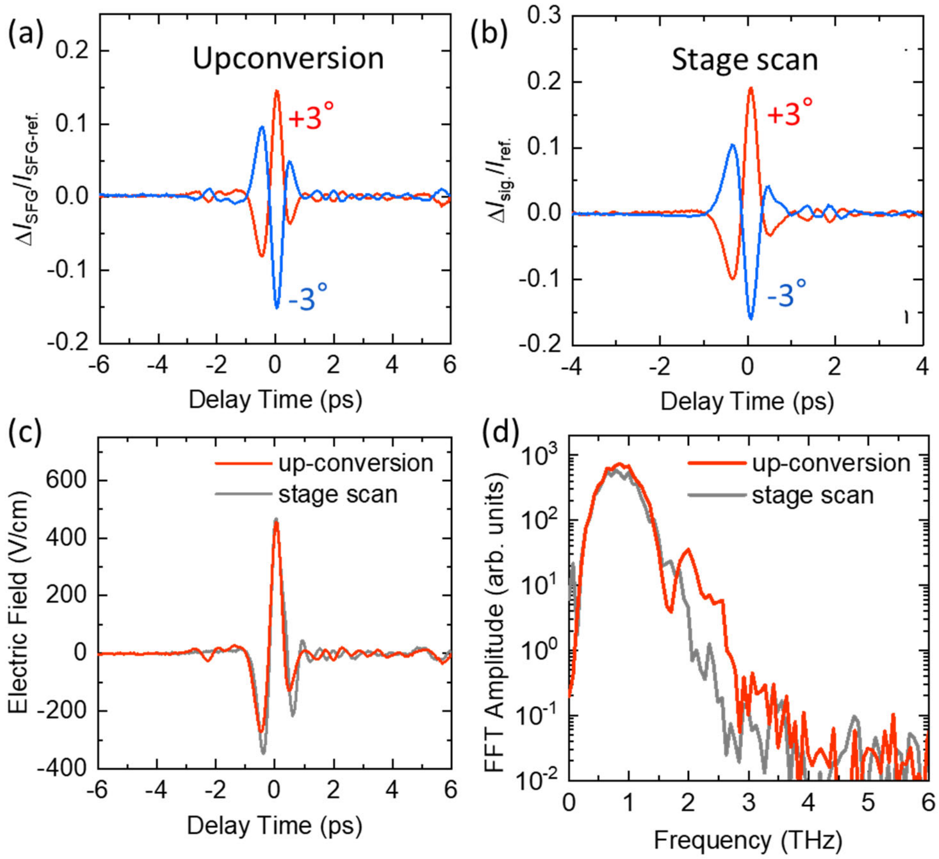

Figure 4. Experimental results of the chirped pulse upconversion spectroscopy with dispersion compensation and comparison with the conventional stage scan method. (a) Terahertz signals obtained with chirped pulse upconversion spectroscopy. (b) Terahertz signals obtained with conventional stage scan method. (c) Obtained terahertz electric field waveforms. (d) Fourier spectra of the obtained terahertz waveforms.

5. Summary

We demonstrate the chirped pulse upconversion spectroscopy with dispersion compensation for the realtime measurement of terahertz waveforms. The obtained waveforms agree with those obtained by the conventional stage scan method indicating significantly reduced waveform distorsion of the time-encoding technique. The proposed method, therefore, is promising for future diagnostic for electric field waveforms in the terahertz frequency region.

References

[1] Tonouchi M. Cutting-edge terahertz technology. Nat. Photon. 2007; 1: 97-105.

[2] Teo S. M, Ofori-Okai B. K, Werley C. A, Nelson K. A. Invited Article: Single-shot THz detection techniques optimized for multidimensional THz spectroscopy. Rev. Sci. Instrum. 2015; 86(5): 051301.

[3] Shan J, Weling A. S, Knoesel E, Bartels L, Bonn M, Nahata A, Reider G. A, Heinz T. F. Single-shot measurement of terahertz electromagnetic pulses by use of electro-optic sampling. Opt. Lett. 2000; 25(6): 426-428.

[4] Minami Y, Hayashi Y, Takeda J, Katayama I. Single-shot measurement of a terahertz electric-field waveform using a reflective echelon mirror. Appl. Phys. Lett. 2013; 103: 051103.

[5] Jiang Z, Zhang X.-C. Single-shot spatiotemporal terahertz field imaging. Opt. Lett. 1998; 23: 1114-1116.

[6] Tamaki R, Suzuki M, Kusaba S, Takeda J, Katayama I, Ultrafast time-resolved spectroscopy via chirped-pulse up-conversion with dispersion compensation. Submitted.

Design of Sub-THz Signal Generation Device Based on Optical Difference Frequency Generation Using T-Branch $LiTaO_3$ and Al_2O_3 Rectangular Waveguide

Ken Paramayudha[1,2*], Yui Otagaki[1], and Hiroshi Murata[1]
[1]Graduate School of Engineering, Mie University, Tsu-city, Mie, Japan
[2]Research Center for Telecommunication, National Research and Innovation Agency (BRIN), Bandung, Indonesia
*Corresponding author: 422DE01@m.mie-u.ac.jp

Abstract – A new device for sub-THz signal generation based on optical difference frequency generation (DFG) is proposed. Periodically poled *z*-cut $LiTaO_3$ crystal is utilized to generate sub-THz signals by nonlinear optic effect with quasi-phase matching (QPM) between the lightwaves and generated signal. The crystal is located inside a rectangular waveguide which acts as a resonant cavity to enhance the output DFG signal power. Analysis results show that the proposed structure can obtain up to 6×10^4 field enhancement at the target frequency of 100 GHz. For the generated signal coupling, a T-branch $LiTaO_3$ and Al_2O_3 rectangular waveguide is designed, with a coupling enhancement of approximately 11 dB compared to an $LiTaO_3$ and air-filled T-branch waveguide. We believe the proposed device is promising for integration with external sub-THz circuits.

Keywords – coupling enhancement, difference frequency generation, lithium tantalate ($LiTaO_3$), aluminium oxide (Al_2O_3), rectangular waveguide.

1. Introduction

The sub-terahertz (sub-THz) radio spectrum is attractive for numerous advanced applications such as remote sensing and high-speed wireless communications [1]. For these applications, the generation of efficient sub-THz signals is thus become a significant concern. Difference frequency generation (DFG) based on the second order nonlinear optical effect is one potential candidate for this signal generation.

In the past, various approaches for DFG based millimeter-wave (MMW) and sub-THz signal generation have been reported [2,3,4]. However, a challenge has been observed in effectively coupling the generated DFG signals to other devices operating in the and MMW and THz frequency ranges. Efficient coupling is crucial to ensure the seamless transmission and utilization of the sub-THz signals in practical applications. To overcome the limitations by the coupling, in this work we propose a novel device structure to improve the coupling efficiency between the DFG device and external sub-THz circuits.

2. Device Structure

The proposed device structure is depicted in Figure 1. The device is divided into two parts, the main waveguide for the optical DFG signal generation and the side branch part for the signal coupling. In the main DFG waveguide, a periodically poled *z*-cut $LiTaO_3$ nonlinear crystal with a width of *a* and a height of *b* is utilized. Other nonlinear optical crystal such as $LiNbO_3$ or $KNbO_3$ are also applicable. The periodically poled structure is designed for the quasi-phase

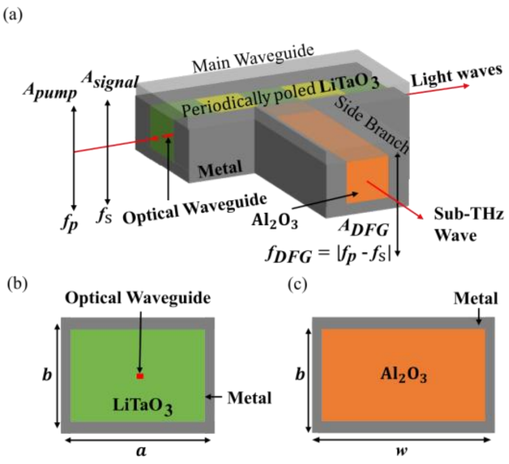

Figure 1. Proposed device structure. (a) 3D-view, and cross-section of (b) main waveguide and (c) side branch waveguide.

matching (QPM) between the optical wave and the generated sub-THz wave. To guide the optical wave inside the crystal, one or a few single-mode optical waveguides are fabricated.

For the generated wave coupling purpose, an Al_2O_3 filled side metal branch with a width of w is included. By using Al_2O_3 ceramics with a dielectric constant $\varepsilon_r = 9.8$, the generated signal from the DFG in $LiTaO_3$ ($\varepsilon_r = 41.1$) can be efficiently coupled for integration with external sub-THz circuits.

3. Analysis

One important point of the DFG-based sub-THz signal generation device is the use of a single guided-mode structure, which allows for the generation of the signals without loss or unwanted radiation. To achieve this condition, the dimension of the rectangular waveguide should be carefully chosen for the desired output frequency.

From the calculated dispersion characteristics that is shown in Figure 2, it is confirmed that the cross section ($a \times b$ = 0.36 mm × 0.2 mm) of the main DFG waveguide only supports a TE_{10} mode at the targeted frequency f_{DFG} of 100 GHz, with an effective index n_{MMW}^{eff} = 4.87.

For the optical waveguide, the wavelength of the operational light is configured to be $\lambda = 1.55$ µm. To obtain a single mode optical waveguide, both the core width and the depth are set to be 3 µm. The light waves group index then can be found as $n_g = 2.17$. Consequently, the polarization reversal period, $2L$, is calculated using following equation [2],

$$2L = c/f_{DFG}(n_{MMW}^{eff} - n_g) \tag{1}$$

with c is the light velocity in vacuum, the polarization reversal period is obtained as 11.1 mm. The complete design parameters of the proposed device are summarized in Table 1.

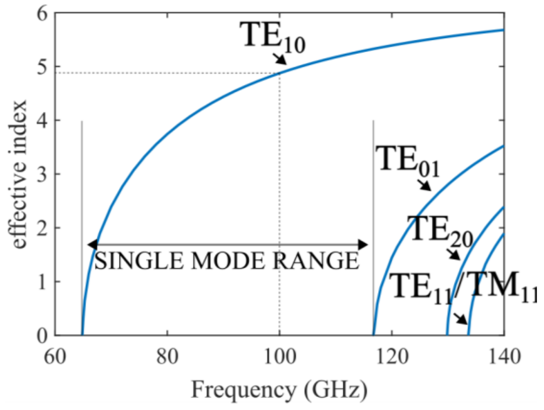

Figure 2. Dispersion curves of the main rectangular waveguide. The cross-sectional size (a x b) is 0.36 × 0.2 mm^2.

The resonance and coupling characteristics were analyzed in detail by use of CST Studio Suite 2023. The setup and the results of the E-field simulation is shown in Figure 3. At the main waveguide, input port 1 is attached at the $LiTaO_3$ cross-section, while the other end of the waveguide is set to be an open port. To see the coupling efficiency, the cross-section of the Al_2O_3 at the end of the side branch waveguide is defined as an output port 2 (Figure 3(a)). For this scenario, the total length (L_t) of the main waveguide is set to be 11.1 mm or about 10 times polarization

Table 1. Parameters of the Designed Device

Material	
Nonlinear optical crystal	z-cut $LiTaO_3$ 0.2 mm thick
Waveguide metal	Al
T-branch waveguide filling	Al_2O_3
Sub-THz waveguide	
Operational frequency	100 GHz
Main waveguide cross section ($a \times b$)	0.36 mm × 0.2 mm
T-branch waveguide cross section ($w \times b$)	0.55 mm × 0.2 mm
TE_{10} mode effective index n_{MMW}^{eff}	4.87
Optical waveguide	
Operational light wavelength	~1.55 µm
Lightwave group index n_g	2.17
Polarization reversal period: $2L$	1.11 mm

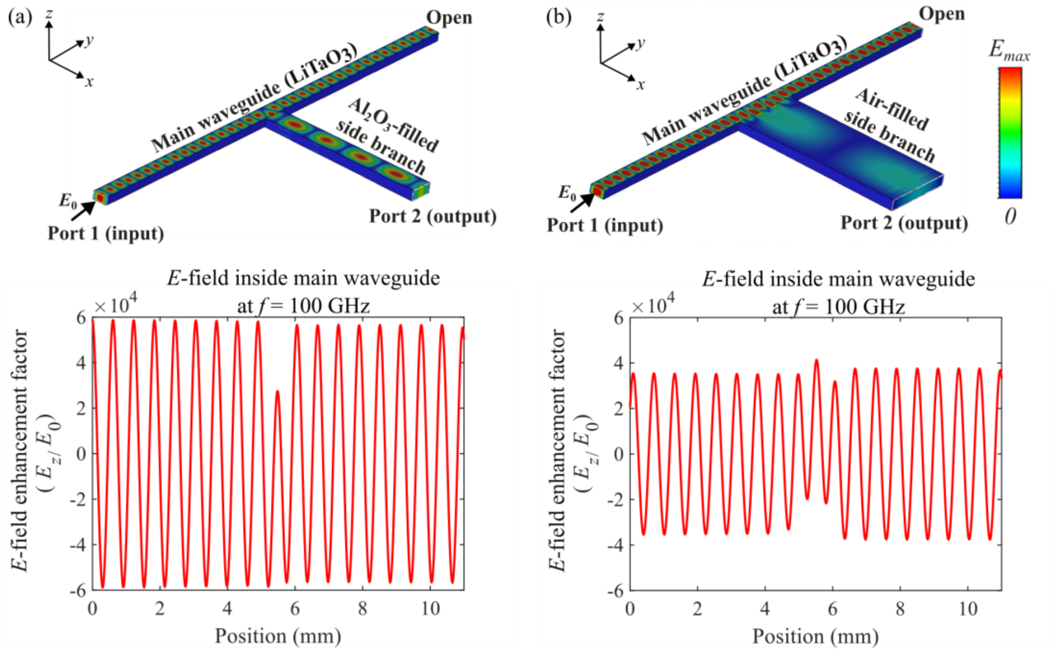

Figure 3. Instantaneous *E*-field simulation results. (a) Proposed T-branch $LiTaO_3$ and Al_2O_3 rectangular waveguide and (b) $LiTaO_3$ rectangular waveguide with air-filled side branch for a comparison.

reversal period for the QPM. As a comparison, an air-filled side branch waveguide with width of w = 17.2 mm and height of b = 0.2 mm is also simulated (Figure 3(b)). The width of this air-filled side branch waveguide is determined so that its cutoff frequency matches that of the proposed Al_2O_3 side branch waveguide.

Owing to the large difference of dielectric constant between $LiTaO_3$ crystal and the air, the wave that propagate inside the crystal is partly reflected at the end of the main waveguide (open port at Figure 3) and become a standing wave. Because of this, the main waveguide then can be seen as a resonator cavity with a maximum *E*-field enhancement factor up to approximately 6×10^4 as seen in Figure 3(a) for the Al_2O_3 side branch case, while for air-filled side branch waveguide is about 4×10^4 as depicted in Figure 3(b). Figure 4 shows the total frequency response which is calculated with consideration of the QPM condition and the resonance cavity characteristics.

From Figure 5 it is obtained that the coupling efficiency of the proposed device is approximately -0.9 dB at a frequency of 100 GHz. The coupling enhancement compared to the $LiTaO_3$ rectangular waveguide with air-filled side branch waveguide is approximately 11 dB, which is rather significant. This is due to the Al_2O_3 ceramics act as a matching layer for the wave generated in the $LiTaO_3$ and enable the wave to be coupled into the side branch waveguide. The results suggest that the proposed device is promising for integration with external sub-THz circuits.

One potential external sub-THz device to

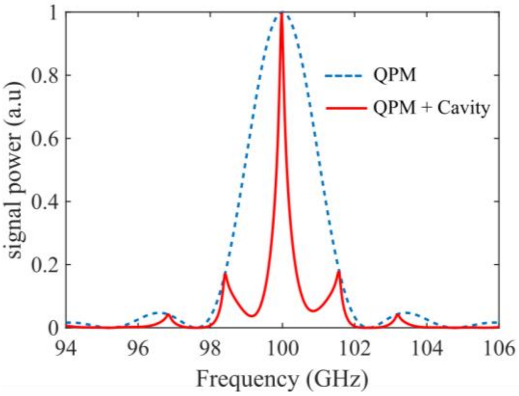

Figure 4. Calculated frequency response of the designed device, assuming total length L_t = 11.1 mm.

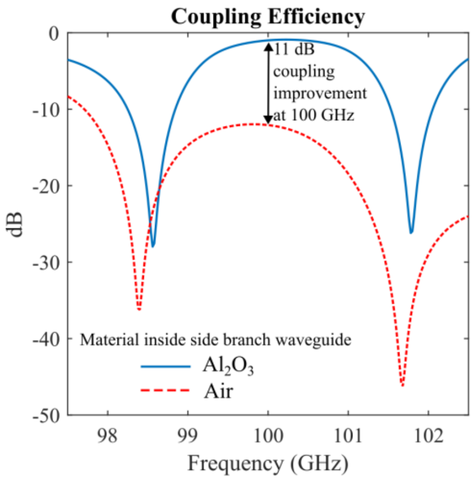

Figure 5. Coupling efficiency of the proposed device compared to the $LiTaO_3$ rectangular waveguide with air-filled side branch.

be integrated with the proposed device is Al_2O_3-based antenna, as illustrated in Figure 6. The addition of an antenna at the end of the side branch waveguide can open up various advanced applications such as wireless beamforming [5], optical-based antenna measurement systems [6], and hybrid optical-THz communication system [7].

4. Conclusion

A new device structure for coupling enhancement of sub-THz signal generation device based on optical DFG is proposed. The simulated results show that using a Al_2O_3 ceramics inside a side branch waveguide, a significant coupling increasement can be achieved. The coupling enhancement is about 11 dB over the $LiTaO_3$ rectangular waveguide DFG device with air-filled side branch. In the near future, we plan to fabricate the proposed device and do further experiments.

Acknowledgment

This work was supported in part by the research and development project entitled with 'THz and optical wireless aggregation research & development for B5G (Toward-B5G)' from NICT, Japan.

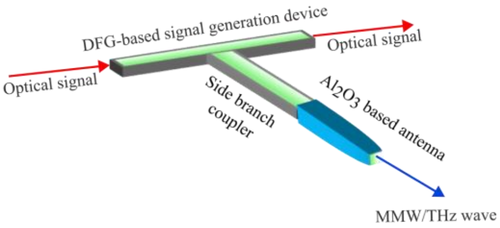

Figure 6. Future integration of the proposed devices that can be utilized for various advanced applications.

References

[1] Fujishima M. Overview of sub-terahertz communication and 300 GHz CMOS transceivers. IEICE Electronics Express, 2020 paper ID 18.20212002.

[2] Ngo QH, Murata H, Okamura Y. Microwave signal generation device using difference frequency generation in a $LiTaO_3$ rectangular waveguide. Journal of Lightwave Technology, vol. 28, no. 19, pp. 2791-2799, 2010.

[3] Takashima Y, Maejima Y, Murata H, Okamura Y, Kanno A, Kawanishi T. Millimeter-wave signal generation device using optical difference frequency generation in $LiTaO_3$ crystal suspended to rectangular waveguide. MWP and APMP Conference Proceedings, 2014, pp. 153-156.

[4] Takashima Y, Maejima Y, Murata H, Okamura Y, Kanno A, Kawanishi T. Optical DFG-based 60 GHz signal generation by using a $LiTaO_3$ rectangular waveguide. IEICE Electronics Express, 2014, Vol. 11, No. 12, pp 20140381.

[5] Ito K, Kato K. Remote beamforming scheme with fixed wavelength allocation for radio-over-fiber systems: application to two-dimensional array. IEICE Communications Express, 2020, paper ID 2022XBL0149.

[6] Kurokawa S, Ameya M, Hirose M. W-band millimeter-wave antenna measurement system using an optical fiber link millimeter-wave generator. 2022 International Symposium on Antennas and Propagation (ISAP), Sydney, Australia, 2022, pp. 355-356.

[7] Zhang L et al. Hybrid fiber–THz fronthaul supporting up to 16384-QAM-OFDM with the delta-sigma modulation. Optics Letters, 2022, 47, 4307-4310.

Wireless Terminal Localization Experiment Using Radio-over-Fiber Links

Hiroto TERAI, Yui OTAGAKI and Hiroshi MURATA

Graduate School of Engineering, Mie University 1577 Kurima-Machiya-Cho, Tsu-City 514-8507 Japan
*Corresponding author: murata@elec.mie-u.ac.jp

Abstract – Experiments for the identification of a wireless terminal position using the radio-over-fiber (RoF) technique were reported. Good accuracy below 10 cm in the terminal localization experiments was obtained using four broad-band antennas and RoF links. This is effective for the application to future Beyond-5G/6G mobile communication systems with massive connectivity.

Keywords – mobile terminal, localization, radio-over-fiber, TDOA

1. Introduction

Mobile wireless communication technologies become indispensable for a lot of communication systems and DX applications in the world. In Japan, the 5th generation (5G) mobile communication services have been opened from wireless carrier companies. Then, research and studies on new technologies for the Beyond-5G/6G mobile communication technologies are now underway in the world.

In the future Beyond-5G/6G mobile communication systems, massive terminal connectivity is required to be increased over 10 times compared to the 5G system. In order to meet this challenging requirement for the connectivity, the identification of each wireless terminal position becomes rather important, we believe.

In this paper, terminal localization experiments using radio-over-fiber (RoF) links are reported [1]-[3]. RoF links are rather useful to transfer wireless signal information precisely with a small transmission loss and small distortion. Accuracy with a few centimeters was obtained in the terminal localization experiments.

2. Localization Experiment

Figure 1 illustrates the basic principle of the terminal localization by use of the time difference of arrival (TDOA) method [1], [2]. The position of the wireless mobile terminal can be identified by measuring and calculating the differences of the wireless signal arrival times detected in each remote antenna unit (RAU). As shown in Fig. 1, at least three RAUs are required to identify the position of the terminal in the measurement plane.

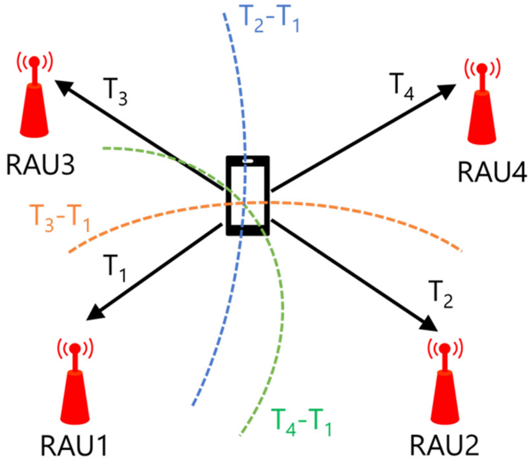

Figure 1. Principle of the TDOA method for terminal localization.

By using the RoF links, an experiment for TDOA method was carried out. The experimental set-up for terminal localization is shown in Fig. 2.

A standard dipole antenna connected on a metal pole was used as a test terminal (TX). A test wireless signal was supplied from a measurement equipment (VNA) to the TX and emitted to the surrounding space. 4-remote antennas (RAU1, RAU2, RAU3 and RAU4) were set around the TX to detect the emitted signal. The signal from each RAU was converted to an optical signal and transferred back the VNA via RoF links.

RoF links were composed of standard silica single-mode fiber (SM fiber) cables of ~10 m, DFB lasers, and high-speed photodiode (~10 GHz). The DFB lasers are integrated with a Bias-Tee circuit for high-speed direct modulation up-to ~10 GHz and a temperature controlling unit.

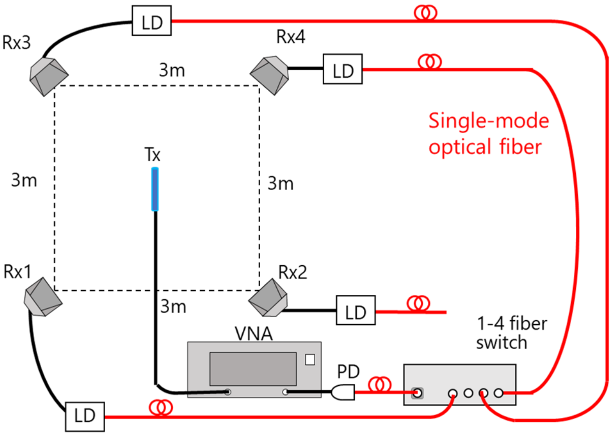

Figure 2. Experimental set-up.

3. Measured Results

Typical examples of the measured results are shown in Fig. 3. Clear signals emitted from TX were measured and identified by RAUs through the RoF links (Fig. 3(b)). The accuracy of the TX position identification was about 5 cm using a test signal with a relatively wide frequency bandwidth of ~8 GHz.

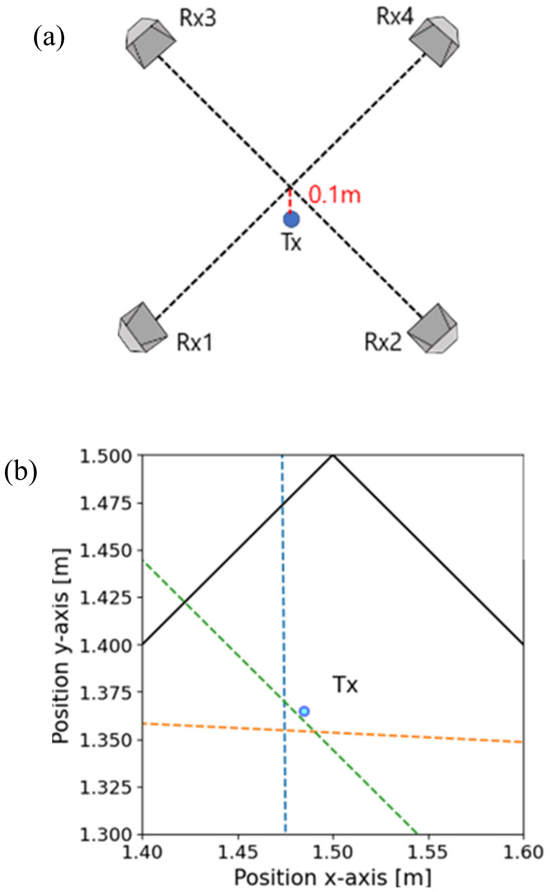

Figure 3. (a) Detailed configuration of the TX antenna and 4-RAUs. (b) Measured TX antenna position.

4. Conclusions

Basic performance of the RoF-based wireless terminal localization was verified successfully. RoF links are rather useful to measure microwave/millimeter-wave wireless signals with small distortion compared to standard metal cables. Further experiment for the localization in a 3-dimentional position with muti-terminals are now underway.

Acknowledgements

This work was supported in part by the research and development project entitled with ‘THz and optical wireless aggregation research & development for B5G (Toward-B5G)' from NICT, Japan.

References

[1] Kakubari Y, Yonemoto N, MMW mobile terminal positioning using remote receivers. 2017 IEEE Conference on Antenna Measurements and Applications (CAMA) Dec. 04-06, 2017, Tsukuba, Japan, pp. 341-344.

[2] Kakubari Y, Koga T, Yonemoto N, Aircraft Surveillance System using Radio over Fiber Technology, The Review of Laser Engineering, 2020; 46(1): 32-37. (in Japanese).

[3] Otagaki Y, Terai H, Murata H, Basic experiment of mobile terminal localization using RoF link, IEICE Spring Meeting, C-14-14, 2023. (in Japanese).

[Invited Talk] EM Measurement through Optical Fiber

(Applications to Archaeological Survey of the Pyramid and Humanitarian demining)

Motoyuki SATO
Professor Emeritus, Tohoku University, 980-8576 Sendai, Japan
ALISys Co., Ltd,, 980-8579 Sendai, Japan

motoyuki.sato.b3@tohoku.ac.jp

Abstract – We have conducted research on electromagnetic field measurement methods using various types of photonics applications. It includes the use of optical signal link and optical electric field sensors, especially to imaging radar, including Ground Penetrating Radar (GPR). In this report, we demonstrate the use of borehole radar for three-dimensional environmental measurement and the use of bistatic radar for detection of subsurface objects such as landmines, and application to archaeological survey for the great pyramid in Egypt. In all these applications, signal transmission through optical fiber has a great advantage to improve the signal quality, and it makes it possible to have subsurface information.

Keywords – Optical electric field sensor, Imaging radar, Borehole radar, Bistatic radar, Ground Penetrating Radar

1. Introduction

Photonics applied to electromagnetic measurement contributed to many applications in radar technology. We have investigated the use of the optical signal link and the optical EM field sensor for ground penetrating radar (GPR). Replacing conventional metal cables and components by equipment using applied photonics technology, we find many advantages,

The analog optical signal link can be used to extend the RF signal port, and can be used for synchronization of a long distance and also to avoid EM interferences with metallic structures such as cables. The optical electric field sensors are small size and can move without power supply, and having few metal parts is useful to avoid any EM interferences. In addition, extremely wideband systems are available. These features are important for radar-based imaging.

In this report, we will introduce some examples which cannot be achieved without the technology of transmitting RF signal by optical fiber.

2. Photonics Technology Applied to Ground Penetrating Radar (GPR)

Ground Penetrating Radar (GPR) is a geophysical exploration method that is quite useful for shallow subsurface survey. A GPR system is composed from a transmitter and receiver components connected to transmit and receive antennas, and a control unit as shown in Fig.1. RF radar signal and the synchronization signal must be connected among these units, but these units and antennas are located very close to each other, and close to the subsurface targets to be detected.

Figure 1. GPR system using metallic cables.

If we use metallic cables including coaxial cables, electromagnetic wave of the transmitted signal may induce current on the surface of the cables and causes interference to the radar measurement, which include the deformation of the antenna pattern and artifacts in the radar images. If we use optical fibers instead of metallic cables, these problems can be removed, and thus modern GPR systems are adopting optical fiber for this purpose.

On the other hand, if we replace receiving antenna and receiver units by an electric field sensor, the receiver unit can be much smaller than conventional radar systems. And if we use RF-Optical signal link, we can increase the flexibility of location of the transmit and receive antennas, which are quite useful for bistatic radar configurations. In the following sections, we will demonstrate examples.

3. Archaeological Survey by Borehole Radar

Borehole radar is one form of GPR, where we measure subsurface objects and the distribution of subsurface cracks around the borehole by lowering a radar device housed in a water-resistant sonde into an excavated borehole with a diameter of about 10 cm or less. Due to the size limitation of the downhole sonde, we must use a specialized system.

Due to strong attenuation of EM wave in shallow soil, the maximum depth of GPR survey using the frequency range of 100MHz and a few GHz from the ground surface is limited to a few meters. If we can use a borehole, borehole radar can approach to the deeper targets.

A simple borehole radar uses a metallic cable for suspending a borehole radar sonde in a borehole and supply power and transmit signal. However, these cables can induce current the cable surface and cause many problems.

It is also known that a water-filled borehole can be a good wave guide for electromagnetic wave, and if a metallic cable is located in a borehole, wither water-filled or air-filled, it works as a good wave guide [1].

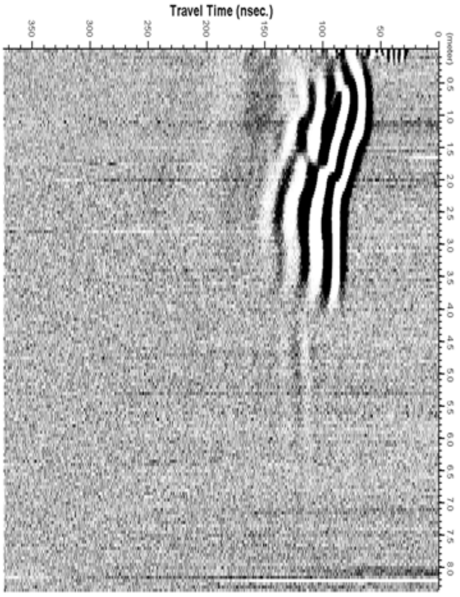

Figure 2. Cross-hole borehole radar signal through the base of rock bridge in Takanawa,

We conducted cross-hole borehole radar measurement for the investigation of the basement of the rock bridge at Takanawa, Tokyo, which was built 150 years ago for the first railroad system in Japan. The basement was filled with soil, and 2 boreholes drilled on the different sides of the bridge were used for measurement. We found that a borehole radar suspended by a metallic cable is strongly influenced by a reflection of the ground surface, which transmit on the metallic cable shades all the reflected signal from the objects. We used a borehole radar system which used optical fibers for radar suspension and signal transmission, can acquired a good quality radar signal which transmitted through the bridge basement as shown in Fig.2, and we used it for the structure analysis, and the new design of exhibition of the historical architecture.

4. Directional Borehole Radar

A borehole radar can use antennas, which can be extended in boreholes, and it has an advantage of using relatively frequency lower than 100MHz to achieve longer penetration depth. The dipole antenna for the lower frequency can be longer than an few meters, and it is very difficult to use on the ground surface. However, a simple dipole antenna is omnidirectional in a borehole. In order to use borehole radar more effectively, we have developed a system shown in Fig.3 that provides directivity by arranging antennas in an array around the circumference of a borehole and three-dimensionally visualizes underground cracks, which are groundwater flow paths [2]-[6] . Mutual coupling of adjacent array antenna elements has a negative effect on directivity synthesis, but by using an optical electric field sensor, we were able to reduce the number of metal components other than the antenna elements and obtain directivity close to the ideal.

Furthermore, when measuring in boreholes at a depth of 50 m or more, metal cables are commonly used for power supply, but metal cables that are close to the antenna can also significantly distort antenna directivity. This problem was also solved by using a photoelectric field sensor.

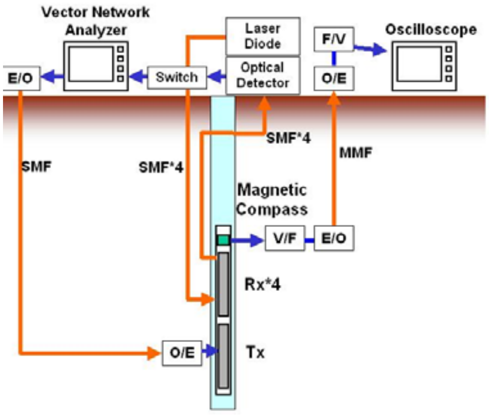

Figure 3. Directional Borehole Radar System.

We demonstrated that underground cracks can be visualized in three dimensions using a prototype directional borehole radar with a diameter of 9 cm and a length of 4 m as shown in Fig.4. Groundwater flow occurs through underground cracks, and borehole radar has been shown to be extremely effective as a method for measuring groundwater in underground applications.

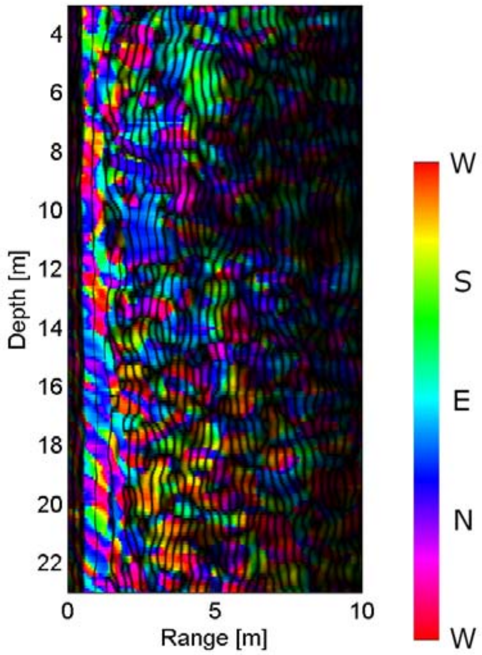

Figure 4. 3D subsurface structure measured by a directional borehole radar.

5. Bistatic Radar for Detection of Buried Mines

GPR is widely used to detect buried objects. We are applying GPR for detection of buried landmines.

We are currently conducting practical landmine detection using GPR in mine affected countries including Cambodia, Colombia, Bosnia and Herzegovina and Ukraine. Fig.5 show the training of Ukraine deminers for the operation of GPR landmine detection sensor ”ALIS (advanced Landmine Imaging System)” which we have developed[7].

Figure 5. Landmine detection training by Ukraine deminers.

ALIS is equipped with a conventional type stand-alone GPR. ALIS has been used in minefields in mine affected countries, but we think smaller sensor benefits in many practical situations. We believe that bistatic radar is a good candidate of an effective next-generation landmine detection radar.

We developed a buried object detection radar that uses bistatic radar in which the transmitter and receiver are located separately as shown in Fig.6 [8]. Here, the transmitting antenna is fixed and radio waves are emitted to the area where buried objects are to be detected. An optical electric field sensor is used as the receiving antenna, and only a small receiver that combines the antenna element and optical electric field sensor scans the measurement target area. The measured data is subjected to synthetic aperture processing to create a three-dimensional visualization of the underground.

In this system, the receiver must capture weak reflected waves from underground, but the electromagnetic field from the transmitting antenna is much stronger and arrives at almost the same time, making it difficult to separate the two waves. First, by using an optical electric field sensor, it is possible to minimize the scattering of transmitted waves by the antenna itself. Also, since the small sensor is small, there is less danger when scanning the ground where landmines are buried. We experimentally demonstrated that by utilizing the difference in the direction of arrival of the transmitted wave and the reflected wave and by using a spatial filter (FK filter), it is possible to separate the two waves and image buried objects as shown in Fig.7.

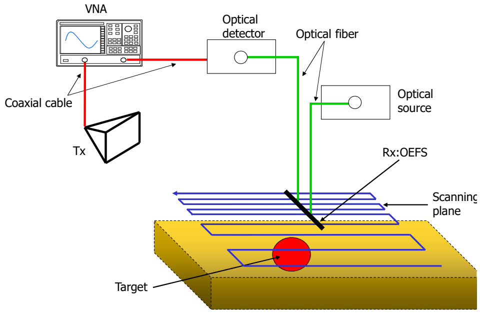

Figure 6. Bistatic GPR system for landmine detection.

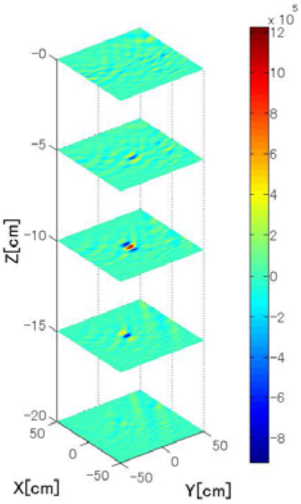

Figure 7. 3D Image of a buried landmine by bistatic GPR.

6. Application to Survey inside the Great Pyramid in Egypt

We have investigated GPR survey in the Great Pyramid in Giza, Egypt since 2018. The aim of this GPR survey is investigation of the inner structure of the great pyramid. After some GPR surveys inside the pyramid by using conventional commercial GPR, we started to develop a low frequency GPR system, which works in bistatic mode. We are trying to use frequency 10-50MHz, which are extremely low as GPR, to avoid internal reflection by the small gap between rock blocks.

Figure 8. The great pyramid in Egypt.

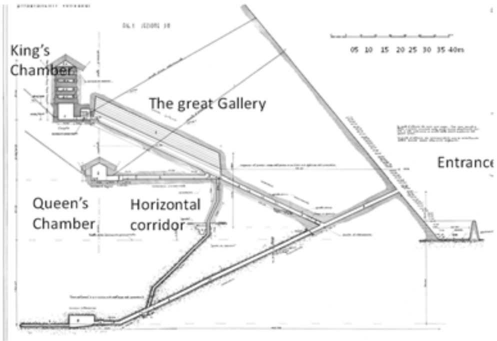

Figure 9. The inner structure of the great pyramid in Egypt.

In order to investigate inside the pyramid structure, we plan to transmit EM wave between a chamber inside the pyramid and the outer surface of the pyramid. The inner structure of the great pyramid is shown in Fig. 9, and we have to achieve transmission of EM wave at least 50m. The transmitter and the receiver have to be synchronized, and we use an optical analog link as shown in Fig.10 for this task. A Vector network analyzer (VNA) is used for the transmitter and receiver and the receiver port is extended by the optical analog link.

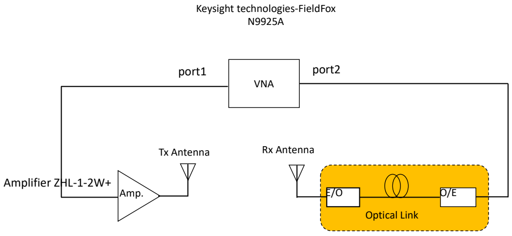

Figure 10. The bistatic radar system.

We started transmission test between the great gallery and the horizontal corridor to the Queen's chamber. However, we found that the electric power cable for lighting inside the tunnel induces current and EM wave propagation is very difficult to observe. Based on these experiments, we could get a permission to remove the conducting cable during our experiment and could receive signal which transmitted through the rock block having 10-20 m distance.

We conducted transmission test in a horizontal corridor connected to the Queen's chamber. The cross section of the horizontal corridor is about 1m x 1m and found dispersion effect in EM wave propagation. We found that this phenomenon is a typical EM wave propagation situation, which show high pass filter effect.

Then we transmitted EM wave from the Tx antenna at the horizontal corridor to the Rx antenna at the great gallery. The configuration is shown in Fig.11.

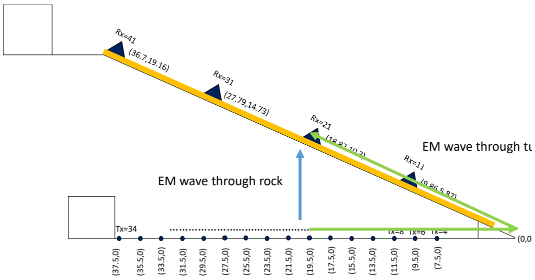

Figure 11. The locations of the transmit and receive antennas in the great pyramid.

The received signal is processed by the matched filter for pulse compression, and an example of the received signal is shown in Fig. 12. The arrival time of the received signal corresponds to the propagation path lengths when we move the antenna positions. We could confirm the transmission up to 20m inside the rock.

We are currently planning to continue this experiment in the pyramid. The use of the optical link made it possible to measure EM wave transmission through more than 20m in the pyramid rock.

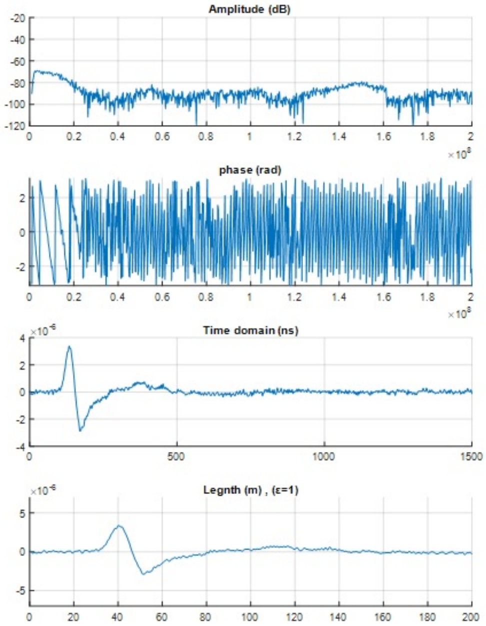

Figure 12. The received signal at Rx=14.5m.

7. Conclusion

In this report, we demonstrated some applications of GPR measurements using the applied photonics instruments including optical EM field sensor and optical signal link. In all the examples, the use of photonics technologies is quite useful, and without the technology, we could not achieve the measurements.

Acknowledgements

This work was partially supported by JSPS KAKENHI Grant Number JP20K20990 and JP19KK0102.

References

[1] M. Sato and R. Thierbach, “Analysis of a borehole radar in cross-hole mode,” IEEE Transactions on Geoscience and Remote Sensing, Vol. 29, No. 6, November 1991.

[2] T.Takayama and M. Sato, “A New DoA Estimation Algorithm for Directional Borehole Radar”, 11th International Conference on Ground Penetrating Radar, June 19-22, 2006, Columbus, Ohio, USA

[3] T.Takayama and M. Sato, “Analysis of Directional Borehole Radar Measurement Data,” 4th International Symposium on Ground Penetrating Radar, Naples, Italy, June 27-29, 2007

[4] T.Takayama and M.Sato, “A Field Measurement with an Array-type Directional Borehole Radar System, “ The 9th Workshop on Subsurface Electromagnetic Measurement, 25th and 26th Oct 2007

[5] M.Sato and T. Takayama, “A Novel Directional Borehole Radar System Using Optical Electric Field Sensors”, IEEE Transactions on Geoscience and Remote Sensing, Volume 45, Issue 8, , pp.2529 - 2535 , Aug.2007.

[6] T.Takayama and M. Sato, “A Novel Direction-Finding Algorithm for Directional Borehole Radar”, IEEE Transactions on Geoscience and Remote Sensing, Volume 45, Issue 8, pp.2520 – 2528, Aug 2007.

[7] M.Sato, G.Pochanin,”Introduction of GPR sensor to Ukraine for Humanitarian Demining,” URSI GASS, Sapporo, Aug. 2023.

[8] Naoki Hayashi, and Motoyuki Sato, “F-k filter designs to suppress direct wave for bistatic ground penetrating radar,” IEEE Transactions on Geoscience and Remote Sensing, Vol.48, no.3, pp.1433 – 1444, Mar. 2010.

[9] M. Sato and, A. El-Hameed, “Consideration of Electromagnetic Wave Propagation Inside the Great Pyramid in Egypt,” URSI GASS, Sapporo, Aug. 2023.

Proceedings of PEM2023
PEM2023-M6

Non-invasive temperature measurement of the porcine cornea-equivalent phantom in THz frequency band

Shota Yamazaki*, Maya Mizuno and Tomoaki Nagaoka
National Institute of Information and Communications Technology, Tokyo 184-8795, Japan.
*Corresponding author: syamazaki@nict.go.jp

Abstract – Since the terahertz (THz) frequency band is expected to be used in the next generation wireless communication system (Beyond 5G), the EMF safety in this frequency band is attracted keen interest. For high-precision exposure estimation, phantoms which imitate the dielectric properties of biological tissues are required. However, tissue equivalent phantoms in THz frequency band are poorly developed. In this study, the complex relative permittivity of porcine cornea was analyzed by the Terahertz time-domain attenuated total reflection (THz TD-ATR) spectroscopy, and we developed porcine cornea-equivalent phantom. Moreover, we improved the porcine cornea-equivalent phantom and enabled non-invasive visualization in that temperature distribution with high spatial resolution.

Keywords – terahertz frequency; porcine cornea-equivalent phantom; temperature measurement

1. Introduction

In recent years, terahertz (THz) technologies over 0.1 THz are emerging for various applications, such as motion sensing, security imaging, and higher speed wireless communications [1]. Also, the electromagnetic filed (EMF) safety in the frequency region has been studied. The dielectric properties of biological tissues in the THz region are necessary for estimating of the power absorption or temperature elevation in the human body. In particular, the dielectric properties of the skin and eyes are crucial, because THz waves are almost absorbed in the body surface due to the intense absorbance of water. However, only a few studies have reported the dielectric properties of the body surface in the THz region [2]. In this study, the complex relative permittivity of cornea from porcine eye was measured by Terahertz time-domain attenuated total reflection (THz TD-ATR) spectroscopy, and we developed the cornea-equivalent phantom.

2. Measurement of the dielectric permitivity in the THz region

THz TD-ATR spectroscopy is employed to determine the complex relative permittivity in the 0.1-1.0 THz region of cornea. In an optical configuration for the ATR spectroscopy, the THz pulses are totally reflected from an interface between air and the silicon prism, and an evanescent wave interacts with a sample placed on the top of the prism (Figure 1). THz time-domain waveforms with and without a sample were detected and Fourier-transformed into an amplitude E(ω) and a phase shift spectrum φ(ω). Subsequently, the complex dielectric constant ε(ω) was calculated from E(ω) and φ(ω) based on the Fresnel's equation. All the measurements of tissues were carried out by a THz TD-ATR spectrometer TAS7500 (Advantest).

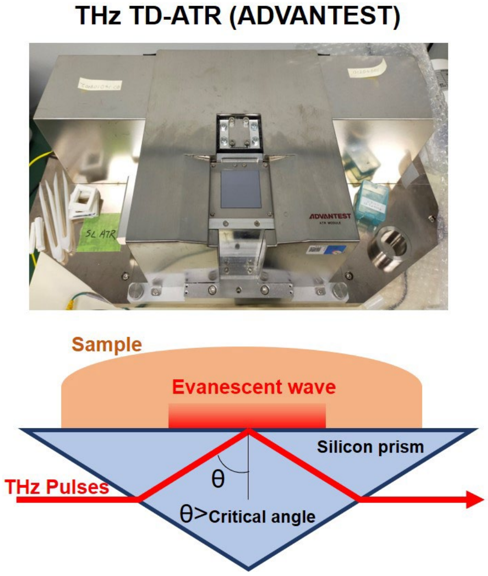

Figure 1. Schematic illustration of THz TD-ATR

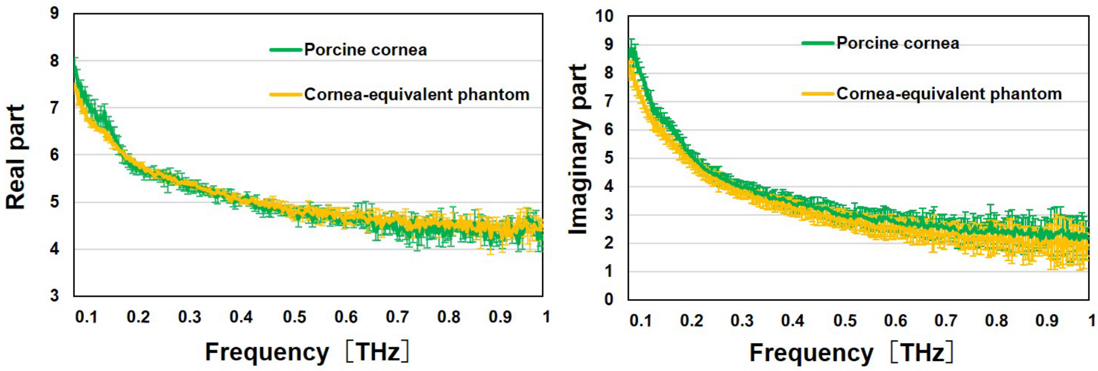

Figure 2. The complex relative permittivity of porcine cornea (green) and cornea-equivalent phantom (yellow).

The complex relative permittivity of cornea was measured at room temperature. Based on the obtained data, we made the cornea-equivalent-phantom, that is composed of 79.5% saline solution, 20% glycerin and 0.5% agar [3]. Figure 2 shows mean values of the complex relative permittivity of porcine cornea (green) and the phantom (yellow) and standard deviation of the 3 samples. The maximum difference in the means of complex relative permittivity between the porcine cornea and that phantom was 6%.

3. Temperature measurement of the cornea-equivalent phantom

The electromagnetic waves in the THz frequency range are strongly absorbed in several hundred micrometers of the body surface [4], and the absorbed energy induces temperature changes. Therefore, temperature measurements in a thin region of the body surface are required to evaluate the thermal effects caused by THz waves. To evaluate temperature changes, we tried to improve the phantom for visualizing temperature distribution using a fluorescent thermoprobe.

Figure 3 shows experimental set-up using confocal laser scanning microscopy for obtain fluorescence images of thermoprobes inside phantom. The temperature of tissue-equivalent phantom was controlled by the glass heater.

Figure 4 shows schematic model of the fluorescent thermoprobe that is a random copolymer composed of distinct units: thermosensitive units, environment-sensitive fluorophores (Fluorescent unit 1, Ex: 458 nm/Em: 560-620 nm) and reference fluorophores (Fluorescent unit 2, Ex: 458 nm/Em: 490-520 nm) [5]. At low temperatures, the thermo-sensitive unit in the fluorescence thermoprobe assumes an extended structure such that neighboring water molecules can quench the water-

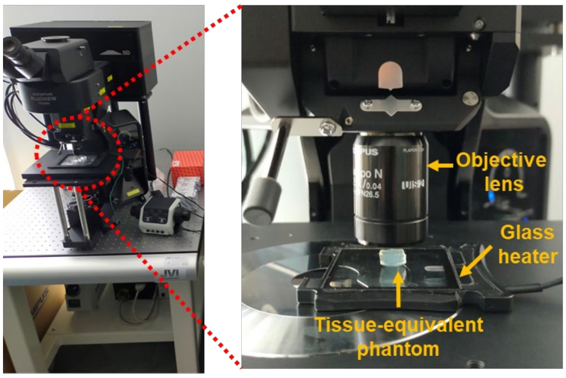

Figure 3. Experimental set-up.

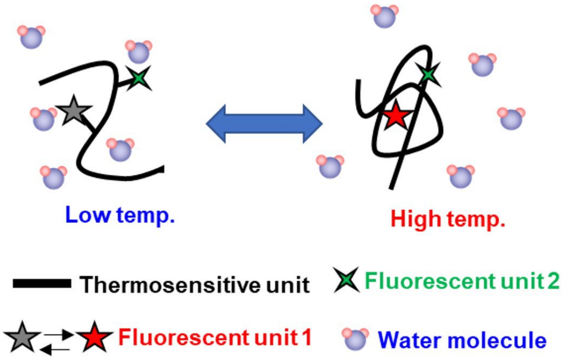

Figure 4. Schematic model of fluorescent thermoprobe.

sensitive fluorescent unit 1. At higher temperatures, the thermo-sensitive unit shrinks because of hydrophobic interactions among the thermo-sensitive units, resulting in the release of water molecules and strong fluorescence from the fluorescent unit 1. In addition, the fluorescence intensity of fluorescent unit 2 is insensitive to the temperature-dependent changes in the thermo-sensitive unit, and its constant fluorescence is utilized as a reference signal. The temperature-dependent fluorescence intensities of the fluorescent thermoprobes enable us to perform highly sensitive and practical ratiometric temperature sensing.

Figure 5 shows the fluorescence images of thermoprobes inside phantom obtained by confocal laser scanning microscopy. The temperature of tissue-equivalent phantom was controlled by the glass heater. Compared to the condition at 22°C, the fluorescence intensity of fluorescent unit 2 was significantly increased in the phantom heated at 40°C. On the other hand, no change was observed in the fluorescence intensity of fluorescent unit 2. The temperature distribution inside the phantom was visualized from the fluorescence intensity ratio of fluorescent unit 1 and 2. Moreover, we analyzed full width at half maximum from obtained fluorescence spectra and confirmed that the temperature distribution inside the phantom can be obtained with a 20 μm spatial resolution in the XY and Z direction.

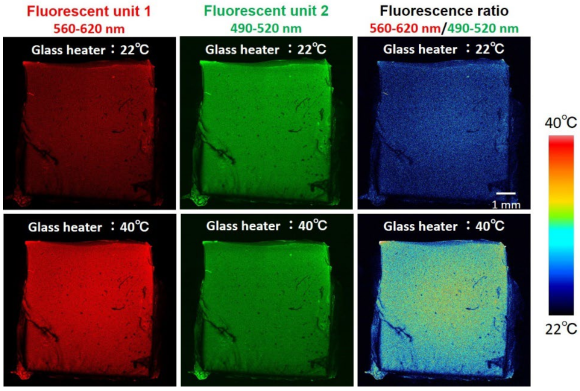

Figure 5. Function of fluorescent thermoprobe in tissue-equivalent phantom.

Figure 6 shows visualized temperature distribution inside the cornea-equivalent phantom heated by the glass heater. We confirmed that this method enables measurement of temperature differences in the phantom with a thickness of 1 cm.

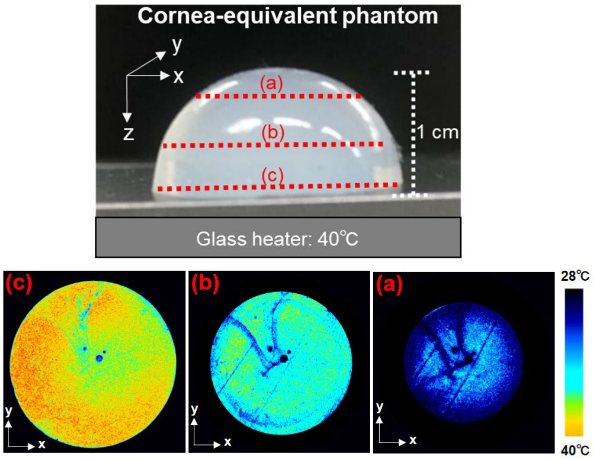

Figure 6. Visualization of temperature inside the cornea-equivalent phantom.

The penetration depth of the THz waves (0.1 THz to 1 THz) into the phantom is less than 500 μm. Therefore, we concluded that the spatial resolution of the thermoprobe is sufficient to measure temperature changes induced by electromagnetic waves in the THz frequency range.

4. Conclusion

In this study, we developed the porcine cornea-equivalent phantom in the THz region and enabled the non-invasive visualization of that temperature distribution with high spatial resolution.

Acknowledgments

Part of this work was supported by the Ministry of Internal Affairs and Communications under Grant Number JPMI10001.

References

[1] O'Hara JF, Ekin S, Choi W, Song I. A Perspective on Terahertz Next-Generation Wireless Communications. Technologies. 7, 43, 2019

[2] Sasaki K., Mizuno M., Wake K. and Watanabe S. Monte Carlo simulations of skin exposure to electromagnetic field from 10 GHz to 1 THz. Phys. Med. Biol. 62, 6993–7010, 2017.

[3] Tomizawa T., Yamazaki S., Mizuno M., Suga R., Yosuke Hashimoto O., and Nagaoka T. The paper of Joint Technical Meeting on Light Application and Visual Science/Instrumentation and Measurement, The Institute of Electrical Engineers of Japan, 11–14., 2023

[4] Yamazaki S., Mizuno M and Nagaoka T. 2022 47th International Conference on Infrared, Millimeter and Terahertz Waves (IRMMW-THz). DOI: 10.1109/IRMMW-THz50927.2022.9896010

[5] Uchiyama S, Tsuji T, Ikado K, Yoshida A, Kawamoto K, Hayashi T, Inada N. A cationic fluorescent polymeric thermometer for the ratiometric sensing of intracellular temperature, Analyst, 140, 4498-506, 2015.

Fundamental Study on THz Irradiation Power Control Using Wire Grids

Maya MIZUNO[1*], Yoshinori TATEMATSU[2], Masafumi FUKUNARI[2], Shota YAMAZAKI[1],Yukihisa SUZUKI[3], Atsushi SUGIMOTO[3], and Tomoaki NAGAOKA[1]
[1]Institute of Information and Communications Technology, Tokyo 184-8795, Japan
[2] University of Fukui, Fukui 910-8507, Japan
[3] Tokyo Metropolitan University, Hachioji, Tokyo 192-0397, Japan
*Corresponding author: mmizuno@nict.go.jp

Abstract – On the basis of THz spectroscopic data for industrial materials and biological substances, various sensing applications are being sought. Furthermore, studies on the effects of exposure to THz waves using high-power THz sources are presently conducted. For precise sensing and exposure experiments, we have fabricated the THz irradiation power control module with wire grids. In this paper, we report the fundamental properties of the power control module.

Keywords – terahertz; power control; wire grid

1. Introduction

In the frequency region over 100 GHz, called the terahertz (THz) region, spectroscopic data have been accumulated for various samples such as industrial materials and biological substances, and the molecular vibrations of the samples have been analyzed using broadband THz spectrometers since the 2000s. On the basis of spectroscopic data, sensing applications are being sought [1, 2]. Furthermore, studies on the effects of exposure to THz waves are presently being conducted at the molecular level using high-power THz sources such as a gyrotron.

Because the THz power variation affects the sensing data and the effects of exposure, THz irradiation power control is required. To enable precise sensing and exposure measurements, we fabricated the THz irradiation power control module with wire grids and verified its fundamental properties.

2. Power control method and measurement results

To control the THz power, we set two wire grids (MWG40-II, Mutsumi Co.) at an incident angle of approximately 30°, as shown in Figure 1. The power of the THz beam was changed by rotating a polarizer.

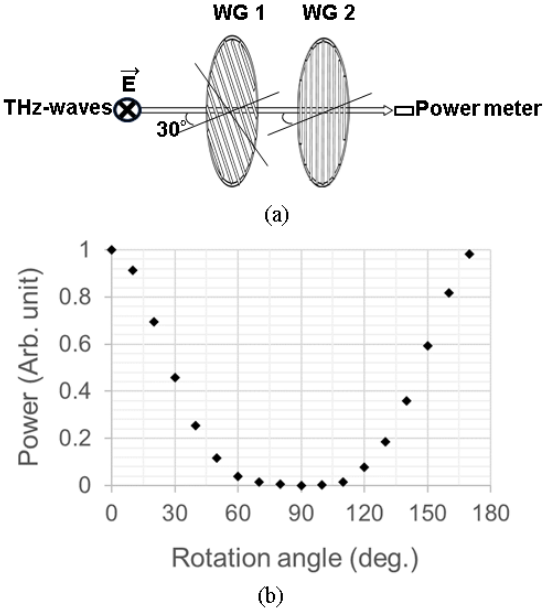

(a)

(b)

Figure 1. (a) Schematic diagram of the terahertz power control module with two wire grids (WGs), and (b) relationship between the terahertz power and rotation angle of wire grid 1 (WG 1).

We firstly checked the relationship between the THz power and the wire grid rotation angle using a 280 GHz IMPATT source (IMPATT-280, Terasense Group inc.) and a power meter (Erickson PM5, Virginia Diodes, Inc.). When the rotation angle of wire grid 1 (WG 1) was vertical to the fixed angle of wire grid 2 (WG 2), the power

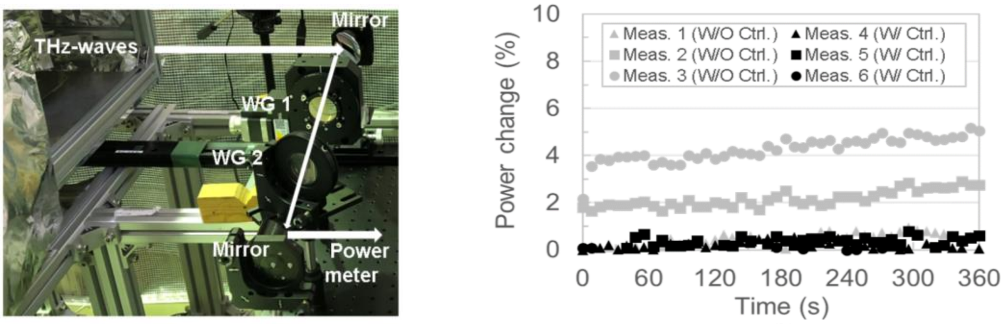

(a) (b)

Figure 2. (a) Photograph of the terahertz power control module with two wire grids (WGs), and (b) changes in the terahertz power without and with control (ctrl.).

became minimum, which agrees with the theory of the orthogonal polarizer method. Also, we confirmed that the change in the power was large at around 30°. Furthermore, there was no significant effect of changing the incident angle. From these results, we determined that the incident and rotation angles should first be set at around 30°, and then the rotation angle should be adjusted only when the power changes.

We attempted to control the power of a gyrotron at 265 GHz (Gyrotron FU CW GV [3]). Parabolic mirrors and two wire grids were set on the THz beamline, as shown in Figure 2(a). WG 1 was rotated, and WG 2 was fixed vertical to the polarization direction of the THz beam (so that transmittance becomes large). The terahertz wave power was monitored using the power meter. Figure 2(b) shows the results of power measurements for 6 min without and with power control. Here, when measurement (meas.) 1 was started, power change was defined to be zero. Without the control module, the powers at the starting time differed between the three measurements. However, with the control module, power change decreased to less than 1% between the three measurements. We found that our power control module is useful for the automatic external control of high-power terahertz sources.

3. Conclusion

A THz irradiation power control module was fabricated. Its property data indicated a possible way of ensuring stable THz power. We intend to measure the THz power distribution using PEM techniques [4, 5], and then to perform precise exposure measurements in the near future.

Acknowledgement

Part of this work was supported by the Ministry of Internal Affairs and Communications Grant Number JPMI10001.

References

[1] Naftaly M, Vieweg N, and Deninger A. Industrial applications of terahertz sensing: State of play. Sensors (Basel) 2019; 19(19): 4203.

[2] Pickwell E and Wallace V. P. Biomedical applications of terahertz technology. J. Phys. D: Appl. Phys. 2006; 39(17): R301–R310.

[3] Tatematsu Y, Yamaguchi Y, Ichioka R, Kotera M, Saito T, and Idehara T. Development of the multifrequency gyrotron FU CW GV with Gaussian beam output. J. Infrared, Millimeter, Terahertz Waves 2015; 36(8): 697–708.

[4] Okada R, Mizuno M, Nagaoka T, Takehara H, Haruta M, Tashiro H, Ohta J, and Sasagawa K. Visualization of THz electromagnetic near field distributions using highly sensitive polarization CMOS image sensor. International Conference on Solid State Devices and Materials. 2023; H-1-05.

[5] Yamazaki S, Mizuno M, and Nagaoka T. High-resolution visualization of the temperature changes in a tissue-equivalent phantom for THz frequencies using fluorescent thermoprobe. 48th International Conference on Infrared, Millimeter and Terahertz Waves (IRMMW-THz) 2023; Mo-P2-58.

Proceedings of PEM2023
PEM2023-M8

Interference-Induced Voltage Measurement for EMI Assessment of Implantable Medical Devices by Exposure to 5G Frequency Radio Wave using Electro-Optical Converter

Funa Tsumura[1*], Shuhei Waki[1], Takashi Hikage[1],
Yoshitoshi Tochikura[2], Takahiro Iyama[2], Junji Higashiyama[2], Yasunori Suzuki[2]
[1] Faculty of Information Science and Technology, Hokkaido University, 060-0813 Sapporo, Japan
[2] NTT DOCOMO INC., 239-8536 Yokosuka, Japan
*Corresponding author: f_tsumura@wtemc.ist.hokudai.ac.jp

Abstract – To investigate the interference implications in the micro/millimeter wave bands of the increasingly popular 5G technology, we have developed a new monitoring tool capable of measuring the interference voltage induced in the pacemaker connector. The new tool enables measurements up to the 5G millimeter wave band, which have not been possible with conventional tools. This tool will be useful for conducting validation studies for numerical simulations to be performed in the future. Our assessment involved the evaluation of interference voltages under near-field exposure conditions in the 5G FR1 frequency bands.

Keywords – Active implantable medical device EMI, Electrical-to-Optical Converter, Fifth generation mobile network, Interference voltage

1. Introduction

Wireless devices have the potential to cause electromagnetic interference (EMI) in other electric appliances. EMI affecting active implantable medical devices (AIMD) like implantable cardiac pacemakers and implantable cardioverter defibrillators (ICDs) represents a critical issue necessitating thorough investigation [1,2]. Numerous studies have been conducted to examine AIMD EMI resulting from various radio devices, leading to the establishment of practical guidelines for preventing AIMD EMI based on experimental findings [3]. However, despite the increasing adoption of the fifth-generation mobile communication system (5G), the EMI characteristics for AIMD in the high-frequency bands used by this system have not been sufficiently investigated.

Moreover, when measuring EMI using actual AIMD devices, even if the presence of EMI can be confirmed, the AIMD itself lacks the capability to measure interference voltage directly. This interference-induced voltage, responsible for the observed effects, cannot be directly assessed.

In this paper, we present interference voltage measurements using voltage sensors integrated into pacemaker internal circuits, along with novel measured results obtained at 3.7 GHz and 4.5 GHz in the frequency band for the 5G FR1. The primary objective of this study is to develop a numerical method to evaluate the electromagnetic influence characteristics of AIMDs, allowing for the prediction of EMI occurrences without relying on actual devices.

2. Artificial pacemaker for interference-induced voltage measurement incorporating an electrical-to-optical converter

The frequency range of conventional EO transducers is from 100 kHz to 6 GHz, and they are not applicable to the millimeter-wave band used as a part of frequency bands for 5G that have been rapidly expanding in recent years [4]. In this report, we insert a compact optically fed EO converter, which can handle higher frequency bands than conventional ones, inside a simulated pacemaker and conduct radio wave exposure tests under similar conditions using the same phantom and experimental system as the artificial pacemaker used in the past and examine the differences in results.

Figure 1 shows the appearance of the electrical-to-optical (EO) converter used in this study. The converter is compact, consumes little power, and does not contain a battery because it is driven by an optical power supply. Therefore, both signal transmission and power supply are performed via an optical fiber cable, enabling stable measurements with almost no electromagnetic field disturbance. The input impedance of the transducer is 50 Ω. The input impedance of the transducer is around 50 Ω in the usable frequency band between 10 GHz to 29 GHz.

Figure 2 shows the configuration of the experimental setup using an artificial pacemaker embedded EO transducer. The housing (CAN) of the pseudo pacemaker is made of titanium and is connected to the lead via an internal connection called a connector block. The leads can be connected to the leads made by the manufacturer used in interference tests. There are two types of leads: unipolar and bipolar. In this paper, the unipolar mode is assumed and connected to the connector block. The unipolar mode is an operating mode of the pacemaker in which the pacemaker CAN and the lead tip are used as electrodes for cardiac sensing and stimulation. The optical signal converted by the EO converter is converted back to an electrical signal through an optical-to-electrical (OE) converter and measured by a spectrum analyzer.

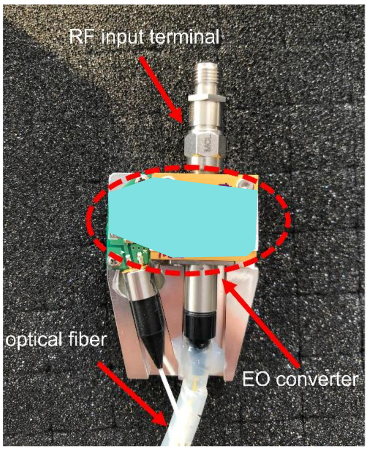

Figure 1. Appearance of EO Converter.

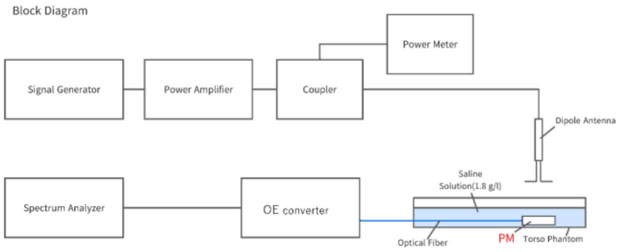

Figure 2. Block diagram of the measurement system.

3. Measurements of interference-induced voltage

A dipole antenna served as the source of radio wave irradiation, positioned approximately 20 mm directly above the pacemaker. The irradiated radio waves are in the 5G FR1 frequency band (3.7 GHz and 4.5 GHz), and measurements are made for both vertically and horizontally polarized waves. In addition, the distance from the surface of the pacemaker to the water surface, i.e., the depth of the salt water, will be 5 mm.

As shown in Figure 3, with respect to the phantom's short direction (X-axis direction), the radio wave irradiation position is varied within a range of ±60 mm at 10 mm intervals, with the connector center position as the origin. Figure 4 and Figure 5 depict the outcomes of the analysis illustrating, the relationship between the antenna position and the interference-induced voltage. The results of interference-induced voltage measurements of a conventionally used artificial pacemaker under similar conditions are also superimposed. Here the power obtained from the measurement is converted to a voltage at an input impedance of 50 Ω.

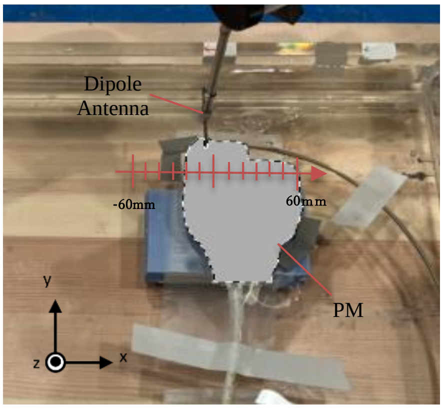

Figure 3. Antenna location directly above pacemaker.

The results show that for both 3.7 GHz and 4.5 GHz, the interference voltage tends to decrease as the radio wave irradiation source moves away from approximately the same position from the connector area. In addition, a comparison of conventional and new products shows a discrepancy of approximately 10 mm with respect to the position of the maximum interference-induced voltage. This variance may be attributed to several factors, including structural differences in the artificial pacemaker, such as the arrangement of the metal wire connecting the pacemaker connector to the internal circuit and the pacemaker's thickness. However, the specific details of these factors are currently under investigation.

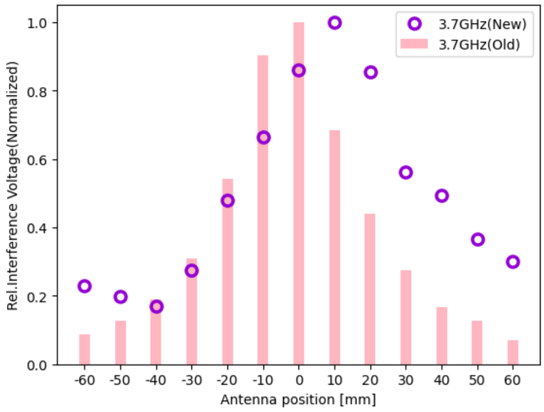

Figure 4. Relation between antenna position and interference-induced voltage at 3.7GHz.

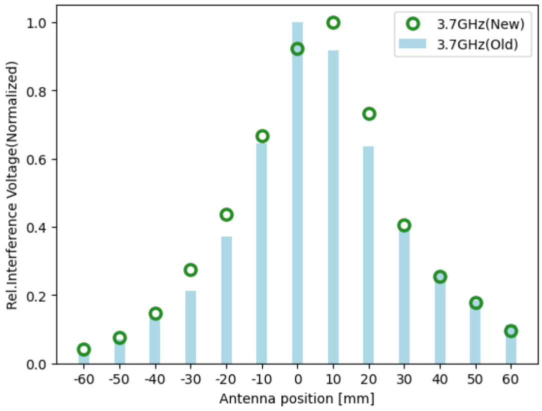

Figure 5. Relation between antenna position and interference-induced voltage at 4.5 GHz.

4. Conclusions

In this study, we sought to assess the electromagnetic interference (EMI) characteristics of implantable medical devices. For this purpose, we devised an interference-induced voltage measurement system incorporating a novel electro-optical transducer with capabilities to operate in the 5G millimeter wave band, a feat beyond the reach of conventional devices. Comparative analyses were conducted between the results obtained from our novel system and those derived from conventional setups.

Looking ahead, we envision utilizing a numerical model comprising a human phantom infused with a 0.18 percent mass saline concentration, along with a meticulously crafted pacemaker model that accurately reproduces the lead connector. Employing electromagnetic field simulation grounded in the Finite-Difference Time-Domain (FDTD) method, we intend to examine the interference voltage induced at the pacemaker's connector when positioned near a half-wavelength dipole antenna. These simulated outcomes will be meticulously compared with the measurement results from our experimental setup to comprehensively evaluate their validity.

References

[1] T. Toyoshima, et al., Japanese J. Cardiac Pacing and Electrophysiology, vol. 12, no.5, pp. 488-497, 1996.

[2] W. Irnich, L. Bats, R. Muller, and R. Tobisch, "Electromagnetic interference of pacemaker by mobile phones", PACE, vol. 19, pp. 1431-1446, Nov. 1996.

[3] Ministry of Internal Affairs and Communications, "Guidelines for Preventing the Influence of Radio Waves from Various Radio Wave Utilizing Devices on Implantable Medical Devices," 2018.

[4] T. Nishikawa, T. Hikage, Takahiro Iyama, Junji Higashiyama, Yasunori Suzuki: "Interference Voltage Measurement for EMI Evaluation of Active Implantable Medical Devices by Exposure to 4G and 5G Frequency Radio Waves using Electro-Optical Converter," IEICE TRANSACTIONS on Electronics, vol. 122, no. 372, EMCJ2022-74, pp.12-16, Jan.2023.

Spatial Synthetic Vertical Local Exposure System to Investigate Thermo-Physiological and Cellular Function Changes Induced by Millimeter-Wave Exposure

Kaito SUGIMURA[1*], Sakura TSURUGA[1], Takashi HIKAGE[1], Hiroshi MASUDA[2], Tasuya ISHITAKE[2], Kun LI[3] , and Akiko NAGAI[4]
[1] Graduate School of Information Science and Technology, Hokkaido University, 〒060-0814, Sapporo, Japan
[2] Department of Environmental Medicine, Kurume University, 〒830-0011, Kurume, Japan
[3] The University of Electro-Communications, 〒182-8585, Chofu, Japan
[4] School of Dentistry, Aichi Gakuin University, 〒464-8650,Nagoya, Japan
*Corresponding author: k_sugimura@wtemc.ist.hokudai.ac.jp

Abstract – In order to study thermo-physiological reactions and changes in cellular functions of living animals and humans induced by millimeter-wave exposure, a novel localized exposure system at 60 GHz was developed using a spatial synthetic technique. We have confirmed that the exposure intensity at the desired area was sufficient to achieve desired temperature rise on the skin surface of living mice.

Keywords – human exposure, millimeter-waves, biological effects, thermal physiology, risk evaluation

1. Introduction

For the coming Beyond-5G and 6G utilization, obtaining biological evidence regarding the safety of exposure to millimeter-wave radiation for humans is important. Conducting research to establish biologically plausible effects and obtaining reliable experimental data to ascertain the international guidelines on the safety of radio wave exposure in frequency bands higher than the millimeter-wave range is crucial [1]-[5]. In this paper, the focus is on the 60 GHz band; a new exposure setup for in-vivo testing in animal experiments is developed, aimed at investigating changes in thermal physiology and cellular function.

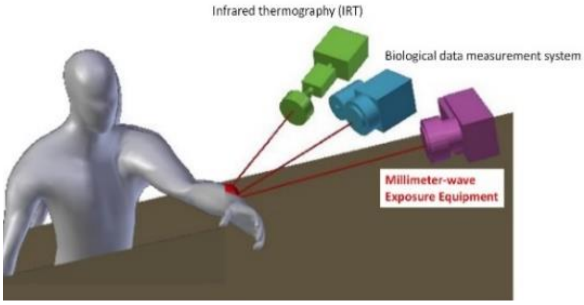

Figure 1. Overview of experimental studies on thermal physiology of human volunteer experiments exposed to MMW.

2. Development of 60GHz Band Exposure Setup.

This study aims to elucidate the dose-response relationship of inflammatory reactions in the skin caused by highly localized exposure to 60 GHz radio waves. Animal experiments using live mice are planned. In previous research, an exposure device was developed using dielectric lens antenna and animal experiments were conducted. Based on our findings, it was deemed necessary to have an exposure device capable of exceeding the 2.5W input power. Therefore, by applying spatial synthesis techniques [6], as shown in Figure 2, a new exposure setup capable of surpassing the required input power was developed.

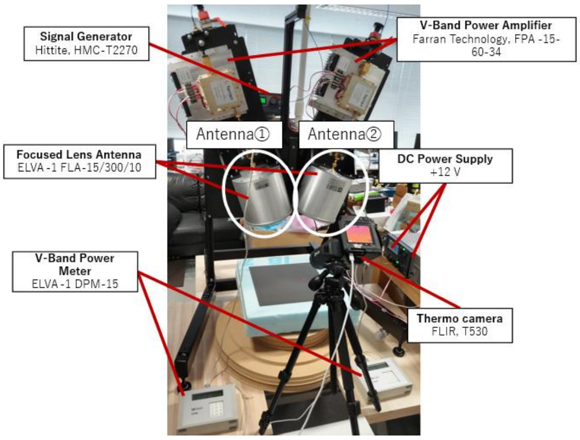

Figure 2. Overview of a 60GHz band exposure setup

3. Characteristics of 60GHz Band Exposure Setup

The 60 GHz signal from the signal generator is distributed into two separate waveguides, amplified by two amplifiers, and radiated from each lens antenna to the same focal point. A block diagram of the exposure system is shown in Figure 3. When the polarization of the antennas is the same, interference fringes are generated in the exposure area. To reduce the interference fringes, we used a method in which the polarizations of the two antennas are orthogonal to each other. When the polarizations are orthogonal, the irradiated radio waves are independent of each other, so interference does not occur. This makes it possible to achieve localized exposure. The angle of incidence of the radio waves from each antenna was set to 17° in order to make the radio waves cross each other. The power absorption rate due to polarization is sufficiently small and negligible.

Next, in order to confirm the relationship between the output of the signal generator and the antenna input power when conducting synthetic spatial exposure, the input power was measured when the output of the signal generator was changed from -30 dBm to 0 dBm. Figure 4 shows the measurement results. In the region where the signal generator output power is below -6 dBm, the input power increases linearly, while above -5 dBm, the input power increases slowly, suggesting that the amplifier is in a saturated state, which is considered the saturation region.

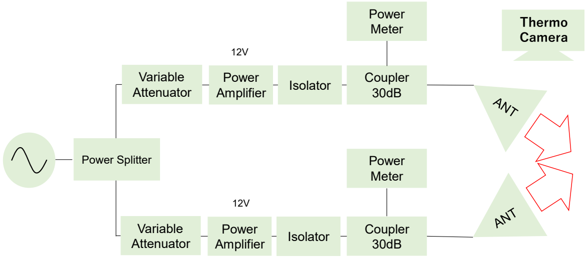

Figure 3. Block diagram of exposure setup

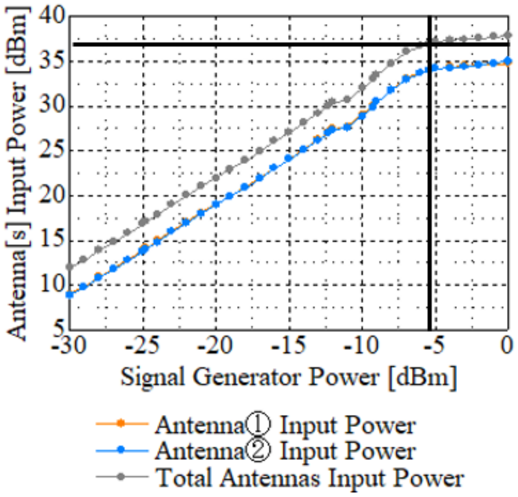

Figure 4. Signal Generator Output and Antenna Input Power

In the saturation region, both two antennas' input power becomes unstable. In addition, it is confirmed that the input power is not stable in the saturated region and fluctuates finely over time, which is difficult to evaluate the quantitative dose-response relationship. Therefore, in-vivo tests of this exposure device were conducted below the saturation region, and the upper limit of the input power was set at 5 W (37 dBm). This is twice the input power required to induce inflammatory response in mouse skin sufficient that the spatial synthesis method has achieved an exposure intensity sufficient for the evaluation of mouse skin inflammatory response.

4. Summary

In this paper, the characteristics of a novel spatial synthetic exposure setup are evaluated. It has been confirmed that the input power was sufficient to achieve the necessary rise in temperature for evaluating heat in the skin of living mice. Based on the results obtained in this study, animal experiments will be conducted in the future.

Acknowledgments

This work was supported by the Ministry of Internal Affairs and Communications in Japan. Grant Number JPMI10001.

References

[1] Alekseev S.I., Radzievsky A.A., Logani M.K., Ziskin M.C.,"Millimeter Wave Dosimetry of Human Skin," Bioelectromagnetics (2007) 29: 65-70.

[2] Kouzai M., Nishikata A., Sakai T., Watanabe S., "Characterization of 60GHz Millimeter-Wave Focusing Beam for Living- Body Exposure Experiments," EMC'09/Kyoto (2009) 22S1-1, Kyoto, Japan.

[3] Laakso I., Morimoto R., Heinonen J., Jokela K., Hirata A., "Human exposure to pulsed fields in the frequency range from 6 to 100 GHz,"Physics in Medicine and Biology (2017) 62.

[4] Foster K. R., D'Andrea J. A., Chalfin S., Hatcher D. J., "Thermal modeling of millimeter wave damage to the primate cornea at 35 GHz and 94 GHz," Health Phys (2003) 84:764–69.

[5] K. Sakakibara, T. Sekiguchi, T. Hikage: "Development of 28 GHz band exposure equipment for studies on thermal perception thresholds of biological effects exposed to millimeter-wave at 5th generation wireless systems candidate frequency band," BioEM 2018, Slovenia 2018.

[6] T. Hikage, R. Ozaki, T. Ishitake, H. Masuda: "Novel 60 GHz Band Spatial Synthetic Exposure Setup to Investigate Biological Effects of 5G and Beyond Wireless Systems on Human Body," Frontiers in Public Health, Volume 9, Article 777712, pp.1-11, Dec.2021.

Comparisons of Averaging Mass of Localized SAR in Estimating Temperature Increase at the Edges of Implanted Metal Plates within the Cellular Radio Frequency Band

Shuhei WAKI[1*], Funa TSUMURA[1], Takashi HIKAGE[1], and Tomoaki NAGAOKA[2]
[1]Hokkaido University, 060-0814 and Sapporo-shi, Japan
[2]National Institute of Information and Communications Technology, 184-8795 and Koganei-shi, Japan
*Corresponding author: s_waki@wtemc.ist.hokudai.ac.jp

Abstract – We performed the numerical simulation in order to evaluate the correlation between local-averaged SAR and temperature increase in the human tissue with the medical metal implant. The FDTD analysis was conducted to evaluate SAR distribution and temperature. In addition, we calculated the 0.1 g-averaged SAR, 1 g-averaged SAR, and 10 g-averaged SAR, and compare them and the temperature increase. As a result, it is found that the 0.1 g-averaged SAR is considered to have a stronger correlation with temperature increase because SAR enhancement due to the metal implant is distributed in a small space.

Keywords –Medical metal implant, Local averaged SAR, Temperature increase, FDTD method

1. Introduction

Metal implants in the human body have been suggested to increase the localized Specific Absorption Rate (SAR) when exposed to radiofrequency (RF) electromagnetic fields [1]. In our previous studies, we confirmed and evaluated the SAR enhancement caused by metal implants using both numerical simulations and measurements [2, 3]. To establish a correlation between the temperature increase and SAR enhancement in the human tissue around implanted metal plates, we conducted a precise examination of the averaged mass dependencies of the local SAR on the temperature rise in this study.

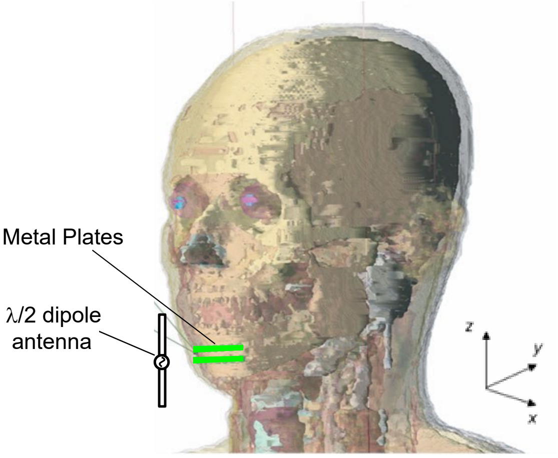

Figure 1. Numerical model

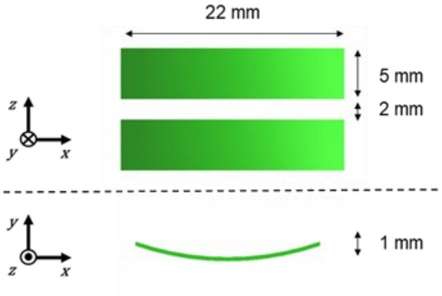

Figure 2. Implanted metal plates

2. Temperature Increase Simulation

SAR in the human tissue was calculated using Finite-Difference Time-Domain (FDTD) simulations, and the steady-state temperature distribution was estimated by solving the bioheat transfer equation, with the SAR distributions serving as the heat source. The numerical models for the simulation are illustrated in Figure 1 and Figure 2 A half-wavelength dipole antenna resonating at 2 GHz was positioned 15 mm away from the implanted metal plates. The minimum voxel size was $0.1 \times 0.1 \times 0.1$ mm^3 whereas the maximum voxel size was $1 \times 1 \times 1$ mm^3 in the FDTD grid. The dielectric properties and thermal properties of human tissue were derived from [4, 5].

The electric conductivity of a titanium alloy $\sigma_{Ti} = 1.3 \times 10^6$ S/m was assigned as the metal plates. The initial temperature of the external air and internal air were 25°C and 31°C, and 37 °C for other tissues.

Results and Summary

Figure 4 illustrates the temperature distribution in the yz-plane passing through the center of the human head as shown in Figure 3 when the incident power of the antenna was 1 W. The green mark indicates the location with the highest temperature, while the red boxes indicate the spaces where the mass-averaged SAR over 10 g, 1 g, and 0.1 g were highest, respectively. Notably, while the 10 g and 1 g averaged SAR were not highest at the location of maximum temperature, the 0.1 g averaged SAR was elevated at that specific location. Consequently, the 0.1 g averaged SAR is considered to have a stronger correlation with temperature increase from the simulation results.

In the future, we plan to conduct further studies with different conditions, including varying the frequency and position of the metal plates.

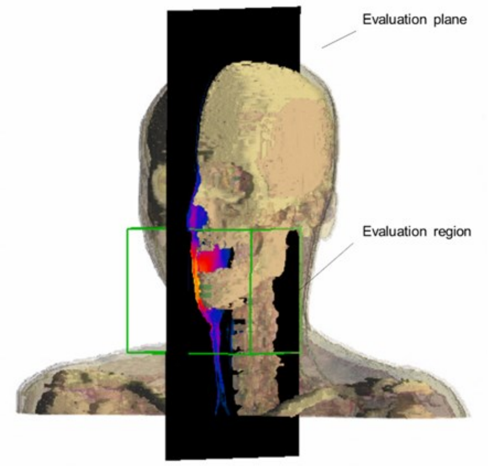

Figure 3. Evaluation plane

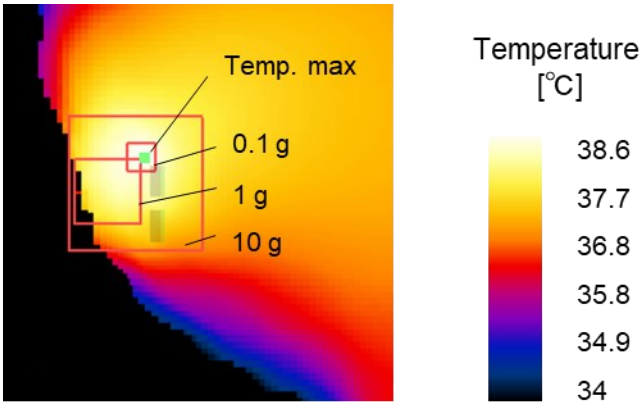

Figure 4. Temperature distribution and mass-averaged SAR around metal plates

Acknowledgments

This work was supported by the Ministry of Internal Affairs and Communications in Japan, Grant Number JPMI10001.

References

[1] H. Matikka, J. Keshvari, and R. Lappalainen, “Temperature changes associated with radiofrequency exposure near authentic metallic implants in the head phantom—a near field simulation study with 900, 1800 and 2450 MHz dipole,” Phys. Med. Biol. vol. 55, no. 19, pp.5867–5881, 2010.

[2] S. Ito, E. Matsuda, T. Hikage, T. Nagaoka, S. Watanabe: "Experimental Estimation on SAR Enhancement Due to Implanted Metal Plates Using Novel Translucent Semi-Solid Phantom," proc. of EMC Sapporo & APEMC 2019, p.765, June 2019.

[3] A. Otsuka, T. Hikage, T. Nagaoka, K. Wake, “Estimation of SAR Enhancement Due to Medical Metal Implants with Screws”, proc. of 2021 IEEE International Symposium on Antennas and Propagation and USNC-URSI Radio Science Meeting, TH-UK.1P.7, Dec. 2021.

[4] C. Gabriel, “Compilation of the dielectric properties of body tissues at RF and microwave frequencies,” Brooks Air Force Technical Report AL/OE-TR-1996-0037, 1996.

[5] Hasgall PA, Di Gennaro F, Baumgartner C, Neufeld E, Lloyd B, Gosselin MC, Payne D, Klingenböck A, Kuster N, “IT’IS Database for thermal and electromagnetic parameters of biological tissues,” Version 2.5, Aug. 1, 2014, DOI: 10.13099/ViP-Database-V2.5. itis.swiss/database.

[Invited Talk] Advanced Millimeter-Wave Electro-Optic Modulator Using Antenna-Coupled Electrode

- Applications for Precise Field Measurement and Signal Processing -

Hiroshi MURATA

Graduate School of Engineering, Mie University
1577 Kurima-Machiya-Cho, Tsu-City, Mie 514-8507 Japan
*murata@elec.mie-u.ac.jp

Abstract – The author has proposed and developed antenna-coupled electrode electro-optic modulators operating in quasi-millimeter/millimeter-wave bands for precise electromagnetic field measurement and wireless data signal reception. In this paper, recent research results on the 5G-band electric field sensor system and the high-speed signal detection/processing are reported. Their further applications for the Beyond-5G/6G wireless systems are also discussed.

Keywords – electro-optic modulator, $LiNbO_3$, radio-over-fiber, 5G, beyond-5G, antenna measurement

1. Introduction

Quasi-millimeter-/millimeter-wave band wireless and optical fusion technologies are attracting a lot of interest in many application fields, such as mobile communication, noncontact imaging for security inspection and diagnosis, molecular fingerprint, environmental sensing, and so on. Especially, the photonic-based electromagnetic field measurement (PEM) technology is rather important in precise antenna measurements for the 5G and Beyond-5G/6G mobile systems owing to its extremely low field distortion characteristics compared with the conventional antenna measurement schemes using a probe and metal cable [1], [2]. Besides, in the Beyond-5G/6G mobile communication systems, the wireless-optical fusion technology is to be indispensable for front-haul links to secure many small cells in the future [3], [4].

We have proposed and developed antenna-coupled electrode electro-optic (EO) modulators using the integration technique of planar antennas on a substrate of high-speed EO modulators [5], [6], which is rather effective for wireless-optical signal conversion with extremely low-signal distortion and reasonable signal-to-noise ratio for precise antenna measurements. A key technical point of these modulators is the coupled structure of the precisely designed planar antenna and standing-wave resonant modulation electrode (operational frequency, impedance, and Q-factor) based on micro-strip lines, which enables to improve wireless-optical conversion efficiency compared to conventional EO sensors.

In this paper, recent research results on the 5G-band EO modulator/sensor system to receive and to discriminate a wireless signal with two orthogonal polarization components [7], [8]. The high-speed wireless signal detection and signal processing for autocorrelation [9] are also reported.

2. EO Modulator for Converting Two Orthogonal Field Components

Figure 1 shows the basic structure of our new antenna-coupled electrode EO modulator/sensor to receive and to discriminate a wireless signal with two orthogonal polarization components simultaneously.

The substrate of the modulator consists of a z-cut $LiNbO_3$ EO crystal substrate and a low-dielectric constant substrate of SiO_2 glass bonded together. The antenna-coupled electrodes are composed of four patch antennas for receiving wireless signals and four standing-wave resonant electrodes for applying an electric field to the $LiNbO_3$ optical waveguides. The antennas and electrodes are coupled by use of micro-strip lines. In this configuration, four patch antennas, four resonant electrodes and optical waveguides are precisely designed and set on the substrate to be in a center-symmetric configuration to discriminate two orthogonal polarization components effectively.

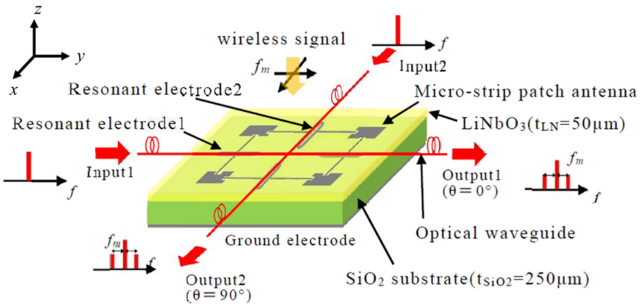

Figure 1. Antenna-coupled electrode EO modulator for converting wireless signals with two orthogonal polarization components.

3. Experiment

The analysis, design, and fabrication of the EO modulators were reported in [7] and [8]. The performance of the fabricated EO modulator/sensor was tested by use of the experimental set-up shown in Figure 2.

Typical examples of the measured frequency responses of the detected and discriminated polarization components are shown in Figure 3. The measured peak-frequency and bandwidth values were in good agreement with the designed ones, and the good signal-to-noise ratio over 30 dB was confirmed as shown in Figure 3, which are suitable for precise analysis and measurement for the 5G-band antenna systems.

The experiments for high-speed wireless-data signal reception and detection were also carried out. A typical example of the measured eye-patterns of the detected base-band signals are shown in Figure 4. The signal detection up-to 5 Gb/s were successfully demonstrated for a single polarization component [8]. By using the QAM format data and polarization multiplexing technique, > 20 Gb/s data reception and detection are expected [8].

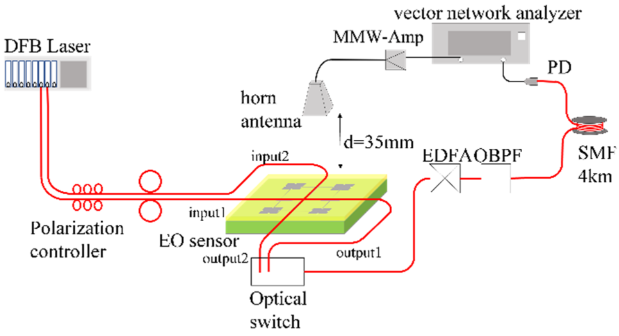

Figure 2. Experimental set-up for testing basic characteristics and polarization discrimination.

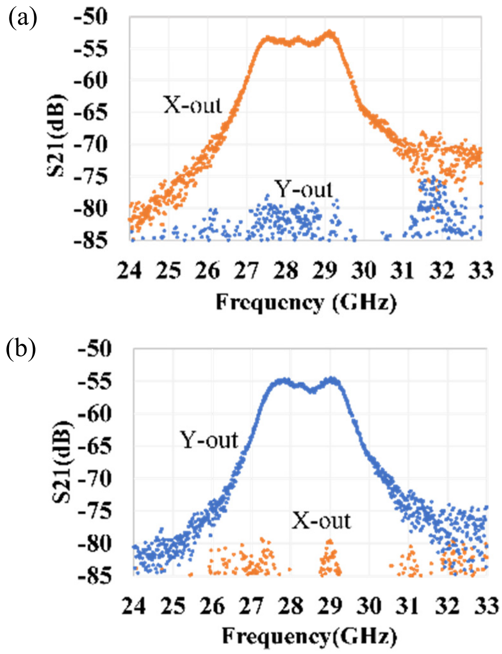

Figure 3. Measured polarization discrimination characteristics of the EO modulator.

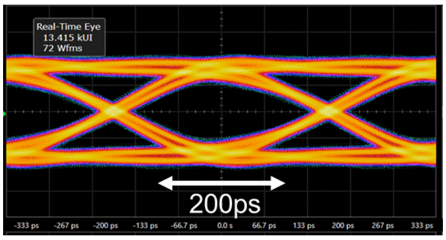

Figure 4. Measured eye pattern for receiving 3 Gb/s ASK signal in 5G band using the EO modulator.

4. Signal Processing Application

The applications to signal processing were also carried out. In the preliminary experiments, the wireless signal detection and auto-correlation using the fabricated EO modulator with supplying the two-optical signals of a tuned wavelength difference were verified experimentally as shown in Figure 5 [9].

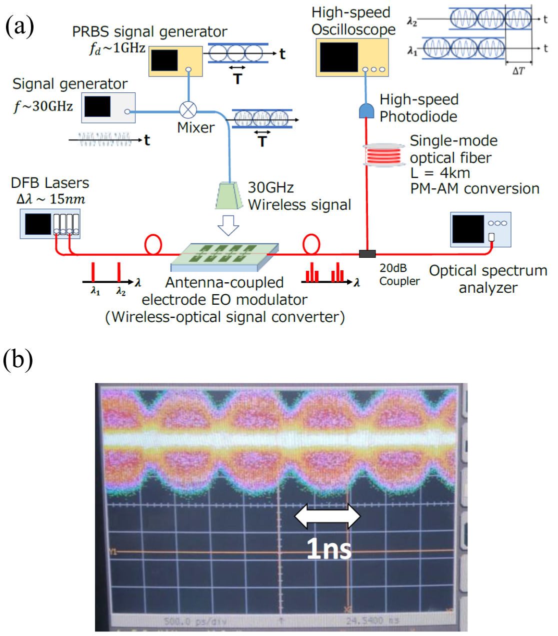

Figure 5. (a) Signal processing experiment using the EO modulator using antenna-coupled electrode with supplying two-optical signals of a tuned wavelength difference.
(b) Measured waveform by use of a high-speed sampling oscilloscope.

5. Conclusions

Good performances of the proposed EO modulator/sensor using antenna-coupled electrodes were verified in the 5G-band.

The applications to the Beyond-5G/6G wireless systems are also underway by adopting a new design of the antenna-coupled electrodes for the operation in > 100 GHz frequency bands.

Acknowledgement

The author thanks Messrs H. Yokohashi, S. Kodama, T. Mori, S. Nakamori, and Dr. Y. Otagaki of Mie University, Japan for their help in analyses and experiments. The author also acknowledges Dr. S. Kurokawa of AIST, Japan and Drs. M. Onizawa and M. Sato of SEIKOH GIKEN Co. Ltd., Japan for their help and support in the EO modulator fabrication and antenna measurements. This work was supported in part by the research and development project entitled with 'THz and optical wireless aggregation research & development for B5G (Toward-B5G)' from NICT, Japan.

References

[1] Kurokawa S, Hirose M, Ameya M. Precision antenna measurement using optical fiber link technologies. 2015 IEEE CAMA, Nov. 2015, Chiang Mai, Thailand.

[2] Kurokawa S, Ameya M, Matsukawa S, Sato M, Onizawa M, Murata H, Hirose M. All optical fiber link antenna measurement system using an industrial robot system. EuCAP 2022, March. 2022, Madrid, Spain.

[3] Vaezi M, Ding Z, Poor HV ed. Multiple Access Techniques for 5G Wireless Networks and Beyond, Springer; 2019.

[4] Ton W, Zhu P ed. 6G: The next horizon, Cambridge University Press; 2021

[5] Murata H. Millimeter-Wave-Band Electro-Optic Modulators Using Antenna-coupled Electrodes for Microwave Photonic Applications. J. Lightwave Technol. 2020; 38(19): 5485-5491.

[6] Murata H, Yokohashi H, Matsukawa S, Sato M, Onizawa M, Kurokawa S. Antenna-coupled electrode electro-optic modulator for 5G mobile applications. IEEE J. Microwaves 2021; 1(4); 902-907.

[7] Yokohashi H, Matsukawa S, Sato M, Onizawa M, Kurokawa S, Murata H. High-Speed Data Transmission Using 28-GHz Antenna-Coupled Electrode Electro-Optic Modulators for 5G Mobile Systems. MWP 2020, P.6, Nov. 24-26, 2020, Matsue, Shimane, Japan.

[8] Nakamori S, Otagaki Y, Sato M, Onizawa M, Kurokawa S, Murata H. 28GHz-Band Antenna-Coupled Electrode Electro-Optic Modulator for Receiving Two Orthogonal Polarization Components Simultaneously. URSI GASS 2023, D09-1-3, Aug. 19-26, 2023, Sapporo, Japan.

[9] Ueda N, Otagaki Y, Murata H. New Signal Processing Technique Using Optical Phase Modulator and Optical Fiber Dispersion Effect. URSI GASS 2023, D09-2-3, Aug. 19-26, 2023, Sapporo, Japan.

[Invited Talk] Photonic Electromagnetic Sensor Technology from DC to THz

Sven KUEHN[1*], Ninad CHITNIS[1], and Niels KUSTER[1,2]
[1]Foundation for Research on Information Technologies in Society (IT'IS), 8004 Zurich, Switzerland
[2]Dept. of Information Technology and Electrical Engineering, ETH Zurich, 8006 Zurich, Switzerland

*Corresponding author: kuehn@itis.swiss

Abstract – Photonic electromagnetic field sensors are the leading technology in applications including reactive near-field measurements, electromagnetic field safety and dosimetry, medical device development, antenna characterization, and traceable electric field calibration setups. This review synthesizes cutting-edge research to illuminate the potential advantages and disadvantages of photonic vs. non-photonic sensing technologies.

Keywords – photonic; electromagnetic field sensors; electro-optical modulators; electro-optical sensing.

1. Introduction

Photonic Electromagnetic Sensor Technology leverages the properties of electro-optic detectors and modulators to enable the detection and analysis of electromagnetic fields across a vast frequency span, from direct current (DC) to extremely high-frequency terahertz (THz). Applications include electromagnetic exposure safety assessment and dosimetry [1],[2],[3], medical technology [4],[5],[7], electromagnetic compatibility measurement (EMC) [1], monitoring and measurement in EM hostile environments [9], antenna characterization [10],[11],[12], photonic sensing in the readout of quantum states [10], to recently even enabling one-step traceability of electric field calibration setups [14].

2. Methods

This review presentation will summarize the requirements for the photonic sensing of electromagnetic fields in diverse applications in the frequency range from DC to THz. We will analyze available photonic sensing technologies, as well as traditional non-photonic technologies, per application, and discuss the advantages and shortcomings of each.

3. Results

A comparison of suitable photonic and non-photonic sensor technologies is presented for the following applications: i) reactive near-field electromagnetic field measurements for distances $r<\max(\lambda, D, D^2/4\lambda)$ with λ the wavelength and D the largest antenna dimension, ii) electromagnetic field measurement in medical applications, iii) characterization of electrically small antennas and devices, and iv) application of photonic technology for traceable electric field calibration.

4. Conclusions

The presentation analyzes photonic electromagnetic field sensing technologies targeted to a set of applications and illuminates the potential of photonic electromagnetic sensor technology, as well as potential disadvantages or shortcomings when selecting a specific photonic or non-photonic sensing technology for each application.

References

[1] Kiminami K, Iyama T, Onishi T, Uebayashi S. Novel specific absorption rate (SAR) estimation method based on 2-D scanned electric fields. IEEE Transactions on Electromagnetic Compatibility. 2008 Nov 7;50(4):828-36.

[2] Calero V, Suarez MA, Salut R, Baida F, Caspar A, Behague F, Courjal N, Galtier L, Gillette L, Duvillaret L, Gaborit G. An ultra wideband-high spatial resolution-compact electric field sensor based on Lab-on-Fiber technology. Scientific Reports. 2019 May 30;9(1):8058.

[3] Burla M, Bonjour R, Salamin Y, Abrecht FC, Haffner C, Heni W, Hoessbacher C, Baeuerle B, Josten A, Fedoryshyn Y, Johnston PV. Plasmonic modulators for microwave photonics applications. InAsia Communications and Photonics Conference 2017 Nov 10 (pp. Su1E-2). Optica Publishing Group.

[4] Kühn S, Kuster N, Kochali B. Active electro-optical probe system for b1-field polarization mapping in magnetic resonance imaging systems. In2014 International Symposium on Electromagnetic Compatibility, Tokyo 2014 May 12 (pp. 666-669). IEEE.

[5] Xu S, Yashchuk VV, Donaldson MH, Rochester SM, Budker D, Pines A. Magnetic resonance imaging with an optical atomic magnetometer. Proceedings of the National Academy of Sciences. 2006 Aug 22;103(34):12668-71.

[6] Kühn S, Kuster N, Kochali B. Active electro-optical probe system for b1-field polarization mapping in magnetic resonance imaging systems. In2014 International Symposium on Electromagnetic Compatibility, Tokyo 2014 May 12 (pp. 666-669). IEEE.

[7] Kühn S, Ponato L, Munz O, Cabanes M, Kuster N. Microphotonic Voltage Probe Used in MRI Environments for Medical Implant Immunity Testing. Proceedings of the the 2nd International Workshop on Photonics Applied to Electromagnetic Measurements (PEM2017), Zurich, Switzerland, October 5- 6, 2017

[8] Kühn S, Pfeifer S, Kochali B, Grobbelaar, E, Sepan P, Kuster N. A Novel Automated Phasor Measurement System for Validated and Traceable EMC/EMI Near-Field Analysis. IEEE Electromagn. Compat. 2016; 5(2): 41–47.

[9] Bohnert, K.; Gabus, P.; Kostovic, J.; Brandle, H. Optical fiber sensors for the electric power industry. Opt. Lasers Eng. 2005, 43, 511–526.

[10] Capstick M, Kuehn S, Kuster N. Measurement technology for electrically small antennas. In 2016 Loughborough Antennas & Propagation Conference (LAPC) 2016 Nov 14 (pp. 1-5). IEEE.

[11] Tanaka Y, Ducournau G, Belem-Goncalves C, Gianesello F, Luxey C, Watanabe I, Hirata A, Sekine N, Kasamatsu A, Hisatake S. Photonics-based near-field measurement and far-field characterization for 300-GHz band antenna testing. IEEE Open Journal of Antennas and Propagation. 2021 Dec 7;3:24-31.

[12] Hirose M, Kurokawa S, Komiyama K. Antenna measurements by one-path two-port calibration using radio-on-fiber extended port without power supply. IEEE Transactions on Instrumentation and Measurement. 2007 Mar 12;56(2):397-400.

[13] Pirandola S, Bardhan BR, Gehring T, Weedbrook C, Lloyd S. Advances in photonic quantum sensing. Nature Photonics. 2018 Dec;12(12):724-33.

[14] Artusio-Glimpse A, Holloway CL, Simons M, Prajapati N, Rotunno D, Berweger S, Campbell K, Jayaseelan M. Rydberg Atoms for One-Step Traceability for Sensing Electric Fields. SMSI Conference, Nuremberg, DE.

Electric Field Distribution Measurement of Indoor Local 5G Using SDR Device

Daiki Imai[1*], Akihisa Tsuchiya[2], Hideaki Sugama[2], Osamu Hashimoto[1], and Ryosuke Suga[1]
[1] Electrical Engineering and Electronics, Aoyama Gakuin University, Kanagawa, Japan
[2] Electrical Engineering, Kanagawa Institute of Industrial Science, Kanagawa, Japan

Abstract – In this research, a visualization system for the electric field distribution in an area of a local indoor 5G network in sub-6 band is fabricated using a software-defined radio (SDR) device. A compact SDR device mounted on a robotic vehicle allows for fast remote-controlled and automated measurements. The measured distributions agreed well with those simulated by ray tracing, attenuations of more than 10 dB in the non-line-of-sight areas.

Keywords – Local 5G, SDR, electric field distribution, ray-tracing.

1. Introduction

A local 5G network in sub-6 band is expected as the infrastructure that enables businesses efficiency in large factories and warehouses. The local 5G network provides more secure, flexible, and robust private networks compared to conventional wireless networks [1]. For indoor applications, multipath reflections from obstructions such as shelf and post can cause unstable communications in the coverage areas. Evaluations of the power distribution and throughput are required for the highly reliable operation of the system. The electromagnetic simulations are difficult due to the above extremely numerous reflections. Therefore, there is growing demand for the measurement visualization of the electromagnetic environment for the local 5G networks.

In this research, a portable spectrum analyzer using a software-defined radio (SDR) device is experimentally validated toward the realization of the automated measurement of the electric field distribution in the local indoor 5G network in the sub-6 band.

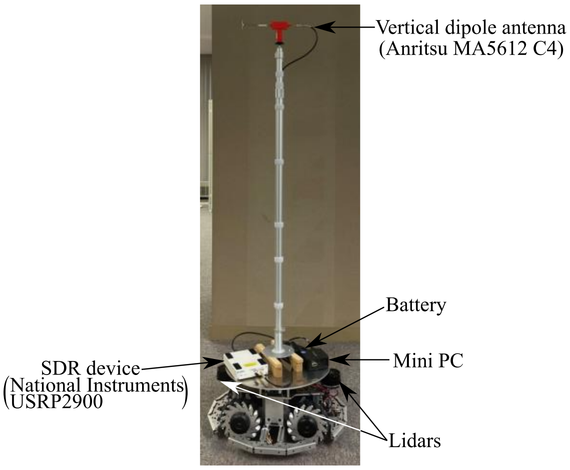

Figure 1. Structure of visualization system.

2. Visualization System and Evaluated Site

Figure 1 shows the picture of the fabricated visualization system and Fig. 2 shows the (a) picture and (b) room layout of a local 5G network site. The visualization system consists of a SDR device, a vertically polarized dipole antenna and two light detection and range (Lidar) systems, and they are mounted on a robot vehicle. The antenna is attached at a height of 1.5 m. A compact SDR device mounted on a robotic vehicle allows for fast remote-controlled and automated measurements [2], [3]. It is well known that the indoor usage of the global positioning system is difficult [4], [5].

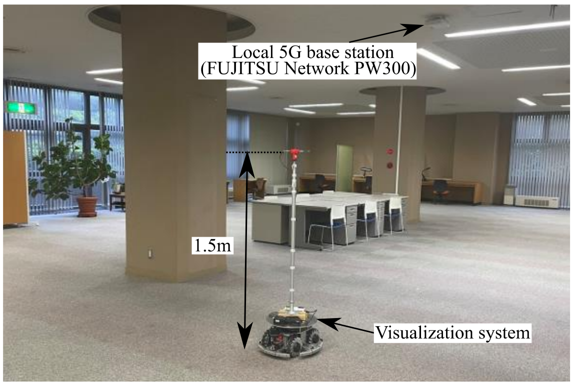

(a) Picture.

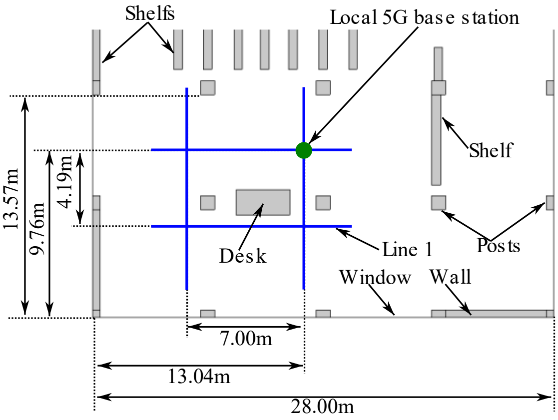

(b) Room layout.

Figure 2. Structure of visualization system.

A local 5G base station with a center frequency of 4.85 GHz and 100 MHz bandwidth (FUJITSU Network PW300) is installed on the 3 m high ceiling as shown in Fig. 2 (a). The room dimensions are 35 m × 28 m × 3 m. The station provides the downlink of 1.6 Gbps and the uplink of 0.3 Gbps.

Observation lines 1 were done 4.19 m and 7.0 m away from the base station. Here, the site has relatively few scatterers, and the ray-tracing simulation is considered possible.

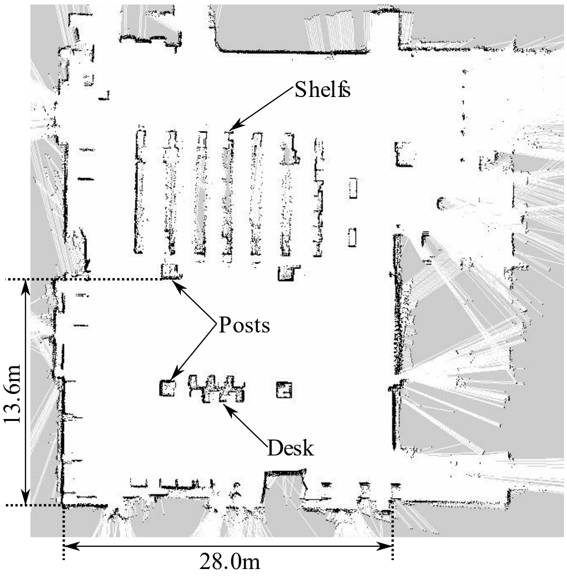

Figure 3. Map generated by using lidars.

3. Electric Field Distribution

3.1 Environmental Mapping

For the safe, accurate, and automated measurements, environmental map was generated by using lidars preliminarily. The vehicle was piloted by a Bluetooth controller to make an environmental map. The lidars provide position, direction, speed of the system and distances from odometry information [4]. The scan angle of the lidar is ±120 degrees and two lidars are mounted on the system.

Figure 3 shows the generated map of the measurement environment and the accurate map is obtained comparing with Fig. 2 (b).

3.2 Measurement and Simulation Conditions

In this measurement, the power spectrum was measured with the center frequency of 4.85 GHz. The measured bandwidth is 50 MHz due to the specifications of the SDR device. The measurement site was mapped for the safe and fast measurement by using the lidar system.

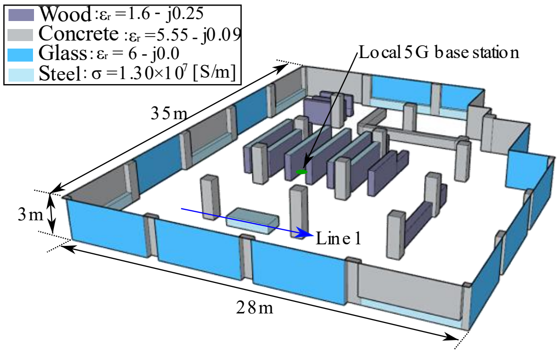

Figure 4. Simulation model.

Figure 4 shows the simulation model with the material constants （permittivity ε_r and conductivity σ） of the objects. The ceiling and floor are assumed as concrete walls. The electric field on the observation line 1 is compared with it by using the ray-tracing simulations. The observation line 1 is in a line of sight (LOS) area and two non line of sight (NLOS) areas are on observation line 1 from -10.0 m to -7.4 m and from 0.5 m to 2.0 m. The frequencies are 4.825, 4.85, and 4.875 GHz, which are included in the measured frequency bandwidth. Three reflections, two diffractions, and two transmissions are applied to the simulation to converge the received power. Here, the antennas and transmit power of the base station are not disclosed and four dipole antennas are applied for the transmitting antenna.

3.3 Results and Discussion

Figure 5 shows the measured electric field distribution plotted on the generated map. The propagation loss and 10 dB attenuation of 10 dB in the NLOS areas are observed.

Figure 6 shows the measured and simulated electric field distributions on the observation line 1. The strengths are normalized to the maximum level on the line 1. The measured distribution including over 10 dB attenuations in NLOS areas agreed well with the simulated one.

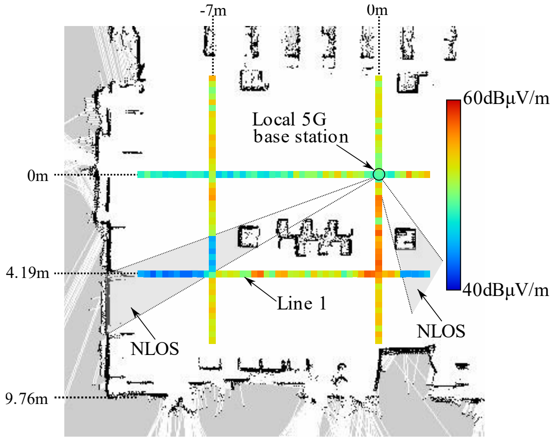

Figure 5. Measured electric field distribution.

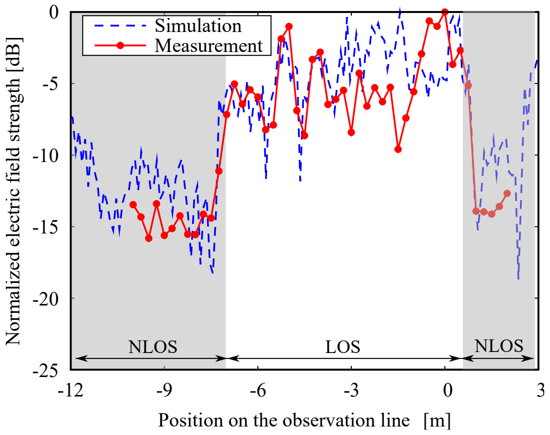

Figure 6. Comparison of electric field strength on the observation line 1.

4. Conclusion

The electric field distribution in an indoor local 5G network site was measured by using a visualization system to confirm the high quality and efficient operation of the local 5G network. The measured distribution agreed well with the simulated one, over 10 dB attenuations in NLOS areas. The measurements in the site having a lot of scatterers are the future work.

References

[1] X. Ji, K. Huang, L. Jin, H. tang, C. Liu, Z. Zhong, W. You, X. Xu, H. Zhao, J. Wu and M. Yi "Overview of 5G security technology," *Sci. China Inf. Sci.*, vol. 61, no. 8, pp. 1-25, Aug. 2018.

[2] D. P. Wright and E. A. Ball, "Highly Portable, Low-Cost SDR Instrument for RF Propagation Studies," *IEEE Trans. Instrum. Meas.* , vol. 69, no. 8, pp. 5446-5457, Aug. 2020.

[3] A. A. Abdallah, J. Khalife and Z. M. Kassas, "Experimental Characterization of Received 5G Signals Carrier-to-Noise Ratio in Indoor and Urban Environments," *2021 IEEE 93rd Veh. Tech. Conf.* , pp. 1-5, Sep. 2021.

[4] I. Makino, J. Terai and N. Miki, "Indoor Local 5G Measurements Employing Automatic Guided Vehicle," *2021 24th Int. Symp. Wireless Personal Multimedia Commun.*, pp. 1-4 Dec. 2021.

[5] M. Quigley, K. Conley, B. P. Gerkey, J. Faust, T. Foote, J. Leibs, R. Wheeler, and A. Y. Ng, "ROS: an open source Robot Operating System," *ICRA workshop on open source software*, vol. 3, no. 3.2, 2009.

Proceedings of PEM2023
PEM2023-T4

Improvement of Prediction Accuracy of Magnetic Field-Based Positioning with a High-Isolation Relay Circuit

Kouga MIYAJI* and Ai-ichiro SASAKI
Dept. of Electronic Engineering and Computer Science, Kindai University, Higashi-Hiroshima, 739-2116 Japan
*Corresponding author: 2333850003v@hiro.kindai.ac.jp

Abstract – Magnetic field-based positioning (MFP) is expected as a method that can establish accurate indoor positioning systems. With MFP, the position of a target device is predicted based on signals received by multiple sensors located at different points around the target area. A key point for accurate positioning is gathering the multiple sensor signals without degrading their quality. One of simple methods to gather the multiple sensor signals is to use a relay circuit. Since a dynamic range of the sensor signals becomes very large in MFP systems, the isolation performance of the relay circuit greatly influences prediction accuracy of the systems. We fabricated a high-isolation relay circuit and investigated the influences of the isolation performance of the circuit upon prediction accuracy of MFP systems.

Keywords – magnetic field; positioning system; machine learning; neural network; relay circuit

1. Introduction

The demand for indoor positioning technologies has been increasing with the popularization of mobile devices. Currently, methods using radio waves are being actively researched for predicting the position of the devices in indoor environments [1, 2]. However, due to the inherent nature of radio waves, it is difficult to avoid the influences of obstacles such as reflections and attenuation, and the positioning accuracy is degraded by these influences.

On the other hand, if the target area is limited to a short distance on the order of several meters, the approach using magnetic fields, which are less susceptible to obstacles, is considered to be promising in terms of prediction accuracy. Because of this advantage, magnetic field-based positioning (MFP) has also been actively studied [3, 4].

In MFP, magnetic field signals emitted by a mobile device (TX) are received by multiple sensors (RX), and the information of the sensor signals is used to predict the Tx position. We previously demonstrated the effectiveness of machine learning for MFP in terms of both prediction accuracy and computational speed [5, 6]. The advantage of applying machine learning to MFP is that the training data, which are the sensor signals, can be easily obtained by calculation. To take this advantage, good agreement between the calculated and real signals is required. In practice, however, it is difficult to realize complete agreement between them.

In real MFP systems, it is necessary to gather the signals received by multiple sensors. One of simple methods to gather the multiple sensor signals is to use relay circuits. It was revealed by our previous research that the main factor of the disagreement is poor isolation nature of the relay circuits [7].

In this study, we investigated the influence of isolation characteristics of the relay circuits upon prediction accuracy of MFP. Furthermore, we fabricated a circuit with physical contact relays (PCRs) and achieved the isolation ratio of 76 dB. The average prediction error obtained with our MFP system was successfully reduced from 24.6 cm to 5.7 cm by introducing the PCR circuit.

2. MFP System with Machine Learning

Figure 1 shows the configuration of an MFP system used in this study. A transmitter (TX) which generates magnetic fields through a uniaxial coil imitates a target mobile device. The position of the TX is predicted based on the magnetic field signals received by multiple sensors (RX1–4). In our system, four RXs are installed, but not limited to four.

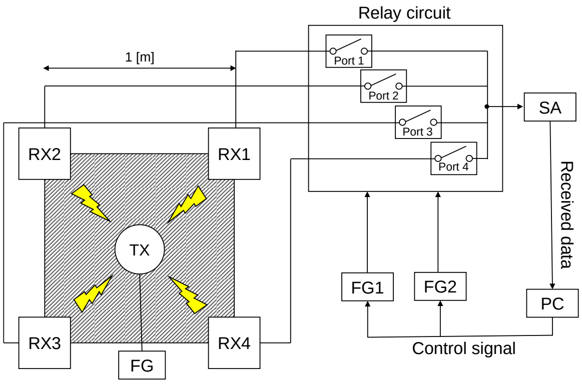

Figure 1. MFP system used in this study.

An AC voltage is applied to the TX from a function generator (FG) to generate magnetic field signals. The signals are received by sensors (RX1–4) placed at four corners of the target area. The four sensor signals are input to a relay circuit, and one of the signals is selected and delivered to a spectrum analyzer (SA). The data signals analyzed by SA are transferred to a PC. It becomes possible to acquire the four sensor signals by switching the relay circuit. The switching operation of the relay circuit is controlled by DC voltage signals generated by function generators (FG1 and FG2). The PC is used for calculating the position of the TX based on the four sensor signals.

Next, we explain the machine-learning approach to MFP systems. As shown in Figure 2, the essence of this approach is generating a predictor function **P** that can output the predicted TX position $\mathbf{r}^{(\mathrm{p})}$ in response to sensor signal information. The superscript (p) means that $\mathbf{r}^{(\mathrm{p})}$ is a predicted position. Obtaining **P** requires a large amount of training data for machine learning. Generally speaking, it is cumbersome and time-consuming to prepare a sufficient number of training data. Fortunately for MFP systems, training data can be computationally obtained, making it easy to prepare a large number of training data.

The training data can be written as

$$\left(B_{\mathrm{calc}}^{(1)}, B_{\mathrm{calc}}^{(2)}, B_{\mathrm{calc}}^{(3)}, B_{\mathrm{calc}}^{(4)};\ \mathbf{r}^{(\mathrm{t})}\right), \tag{1}$$

where $B_{\mathrm{calc}}^{(k)}$ and $\mathbf{r}^{(\mathrm{t})}$ are the calculated values of the received signal of k-th RX and the true position of the TX, respectively.

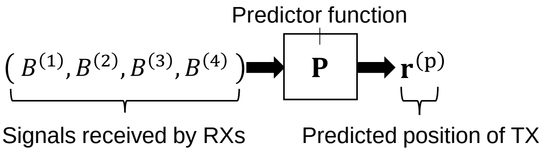

Figure 2. Calculation of TX position by using a predictor function obtained with machine learning.

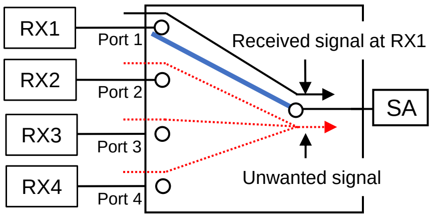

Figure 3. Conceptual diagram of unwanted signal contamination within a relay circuit.

A large number of training data can be prepared easily by calculating $B_{\mathrm{calc}}^{(k)}$ for various $\mathbf{r}^{(\mathrm{t})}$. After machine learning with the training data, we can obtain **P** having the following property.

$$\mathbf{r}^{(\mathrm{p})} = \mathbf{P}\left(B^{(1)}, B^{(2)}, B^{(3)}, B^{(4)}\right) \tag{2}$$

Here $B^{(k)}$ is the received signal of k-th RX. Since $\mathbf{r}^{(\mathrm{p})}$ is the predicted position of TX, it can be regarded as an approximation of the true position $\mathbf{r}^{(\mathrm{t})}$. For evaluating the performance of **P**, we define the prediction error by

$$d \triangleq \left\|\mathbf{r}^{(\mathrm{t})} - \mathbf{r}^{(\mathrm{p})}\right\|_2. \tag{3}$$

In this study, we used “Wolfram Mathematica 12.0” for machine learning and adopted “Neural Network” as the learning method.

3. Prediction Accuracy and Isolation Characteristics of Relay Circuits

Figure 3 shows a conceptual diagram of unwanted signal contamination that degrades the isolation ratio of relay circuits. In MFP systems, the received signal of each RX is delivered to SA via the relay circuit that switches the route (Port 1–4). Figure 3 shows the situation where the path is connected to Port 1. It is considered that the signal received by RX1 is delivered to SA in this situation. However, in practice, signals received by other sensors are slightly transmitted to SA because of incomplete isolation nature of relay circuits.

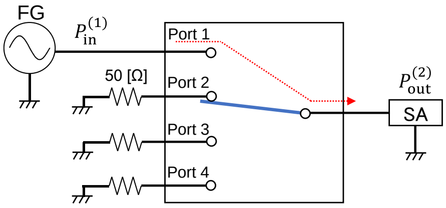

Figure 4. Setup to measure S_{21}.

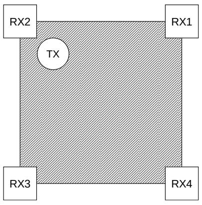

Figure 5. Situation where unwanted signals make the greatest impact on $B^{(4)}$ which is the signal received by RX4.

To quantitatively express the isolation performance of the relay circuit, we define S-parameters as

$$S_{ij}\ [\text{dB}] = P_{\text{out}}^{(i)}\ [\text{dBm}] - P_{\text{in}}^{(j)}\ [\text{dBm}], \quad (4)$$

where $P_{\text{in}}^{(j)}$ is the power input to Port j, and $P_{\text{out}}^{(i)}$ is the power delivered to SA when it is connected to Port i. The S_{ij} $(i \neq j)$ represents the degree of the unwanted signal contamination. As an example, the setup to measure S_{21} is depicted in Figure 4. By measuring S_{ij} for all i and j, the isolation performance of the relay circuit can be determined.

In MFP systems, the negative impact brought about by the unwanted signals becomes maximum when TX is existing in the vicinity of one of RXs. Figure 5 shows the situation where unwanted signals have the greatest impact on the received signal $B^{(4)}$, which is the signal received by RX4. Since $B^{(2)}$ and $B^{(4)}$ respectively become maximum and minimum in this situation, the negative impact of the unwanted signals on $B^{(4)}$ becomes maximum.

To quantitatively investigate the influence of the unwanted signals on prediction accuracy, we define the prediction error D by

$$D(\delta B) = \left\| \mathbf{P}\left(B^{(1)}, B^{(2)}, B^{(3)}, B^{(4)} + \delta B\right) - \mathbf{P}\left(B^{(1)}, B^{(2)}, B^{(3)}, B^{(4)}\right) \right\|_2, \quad (5)$$

where δB is the received-signal error caused by the unwanted signal contamination.

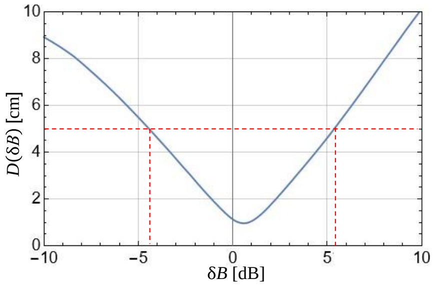

Figure 6. Relationship between the unwanted signal contamination and prediction error.

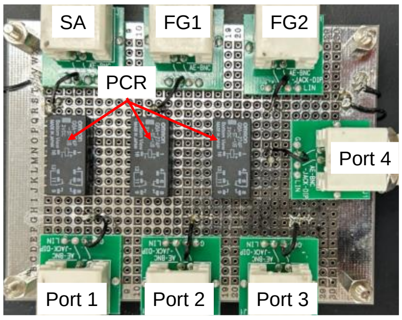

Figure 7. High-isolation relay circuit.

Figure 6 shows $D(\delta B)$ calculated for the situation shown in Figure 5. By considering practical applications, it is desired that the prediction error falls within 5%, which corresponds to $D \leq 5$ cm for our system because the dimension of the target area is 1 m. It is seen from Figure 6 that the received-signals error must satisfy

$$|\delta B| \lesssim 5\ [\text{dB}]. \quad (6)$$

By applying (6) to the situation shown in Figure 5, we obtained the following requirement for a relay circuit.

$$S_{ij} \lesssim -60\ [\text{dB}] \quad (\text{for } i \neq j\,) \quad (7)$$

4. High-Isolation Relay Circuit

We fabricated a relay circuit that meets the requirement given in (7). A photograph of the relay circuit is shown in Figure 7. A remarkable feature of the newly developed relay circuit is that it is equipped with PCRs. Owing to the PCRs, it becomes possible to greatly improve isolation ratio in comparison with circuits equipped with semiconductor relays (SCRs) in which quite large leakage currents exit.

Figure 8 shows measured S-parameters of both the PCR and SCR circuits. The performances of the PCR and SCR circuits are

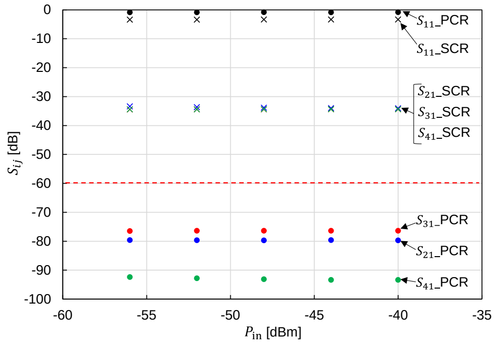

Figure 8. *S*-parameters measured for the PCR and SCR circuits.

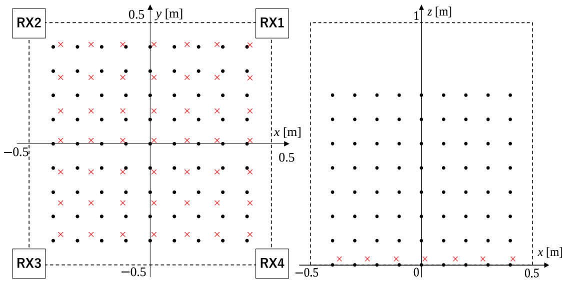

Figure 9. Locations used for training (circle) and validation (cross).

expressed by dots and crosses, respectively. It can be confirmed that the fabricated PCR circuit sufficiently meets the requirement because $S_{ij} \ll -60$ dB for $i \neq j$.

5. Evaluation of Prediction Accuracy of MFP System

We experimentally evaluated the performance of our MFP system with the PCR and SCR circuits. Figure 9 shows TX locations used for training (black dots) and validation (red crosses).

Figures 10(a) and (b) represent prediction errors *d* within *x*-*y* plane ($z = 3$ cm) obtained with our MFP system equipped with the PCR and SCR circuits, respectively. It is confirmed that the prediction accuracy is greatly improved by using the high-isolation relay circuit. Figure 11 shows a histogram of the prediction error *d* obtained with our MFP system equipped with the PCR and SCR circuits. It is seen that the probability of the prediction error *d* being within 5cm, which is the target value of this study, increased from 6.1% to 44.9%. Additionally, the average of *d* was successfully decreased from 24.6 cm to 5.7 cm.

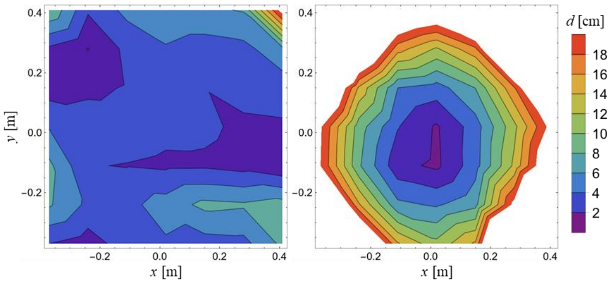

(a) (b)

Figure 10. Prediction errors (*z* = 3 cm) obtained with the MFP system equipped with the (a) PCR and (b) SCR circuits.

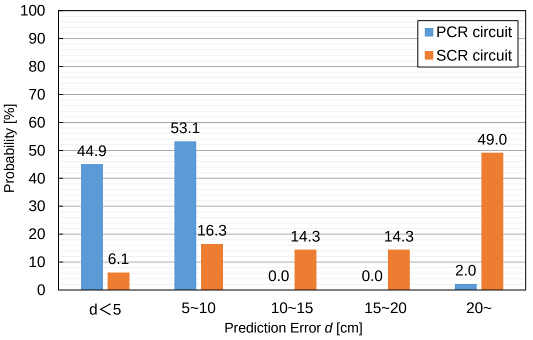

Figure 11. Histogram of prediction errors.

6. Conclusion

We developed a high-isolation relay circuit by using PCRs instead of SCRs. The isolation ratio of the PCR circuit reached 76 dB, which is 42 dB higher than that of the standard SCR circuit. Owing to the high-isolation nature of the PCR circuit, the average prediction error obtained with our MFP system was successfully reduced from 24.6 cm to 5.7 cm.

Acknowledgements

This work was supported in part by JSPS KAKENHI Grant Number 23K03889.

References

[1] A. Nessa *et al.*, IEEE Access **8**, 214945 (2020).
[2] X. Guo *et al.*, IEEE Commun. Surveys Tuts. **22**, 566 (2020).
[3] V. Pasku *et al.*, IEEE Commun. Surveys Tuts. **19**, 2003 (2017).
[4] A. Sheinker *et al.*, IEEE Trans. Instrum. Meas. **68**, 116 (2018).
[5] A. Sasaki and E. Ohta, IEEE Sensors J. **20**, 7292 (2020).
[6] A. Sasaki and K. Fukushima, IEICE Trans. Fundamentals **E105-A**, 994 (2022).
[7] K. Miyaji and A. Sasaki, IEICE Tech. Rep. **PEM2022-14**, 5 (2023). (in Japanese)

Development of Magnetic Measurement and Source Localization System with a Drone and AI

- Aiming for Magnetic Material Detection -

Yu Takemoto*, Sunao Sadahiro, Yoshimi Hatsukade
[1]Faculty of Engineering, Kindai University, 1 Takaya-Umenobe, Higashi-Hiroshima, Hiroshima, 739-2116 Japan

*Corresponding author: 2333850041w@hiro.kindai.ac.jp

Abstract – In this study, we developed a remote sensing system, which measures magnetic field distributions based on a fluxgate sensor mounted on a drone, drone position detection program combining depth sensor ZED and deep neural network (DNN) for object detection, and a program to localize the magnetic field source from the magnetic field distributions using another DNN for regression analysis. Using the system, we measured magnetic field distributions using a magnet as the magnetic source. As a result, the measured magnetic field distributions agree well with the magnetic field distributions from a magnetic source assumed to be a magnetic dipole. The latter DNN program, which estimates position and magnetic moments of the magnetic field source, was used to localize the magnetic source within an error range of about 150 mm from the measured magnetic field distribution.

Keywords – drone; fluxgate magnetometer; neural network; magnetic material

1. Introduction

Because of WWII, unexploded ordnances (UXOs) remain in Japan especially in Okinawa. The UXO detection is still ongoing. In the UXO detection, human-power inspection using metal detectors and ground penetrating radar are used. However, it can be found only small UXOs near the surface by the metal detectors and both the methods are dangerous tasks.

Therefore, we are developing a system that enables the UXO exploration without contact with the ground and without danger to the inspector by installing a highly sensitive fluxgate sensor on a drone and remotely sensing from a low altitude. Here, we develop a magnetic survey system with a highly-sensitive 3-axis vector-type fluxgate, drone position detection program combining depth sensor and deep neural network (DNN) for object detection, and a program to localize the magnetic field source from the magnetic field distributions using another DNN for regression analysis. We constructed the system with the programs, and conducted filed tests on magnet and magnetic material.

2. Magnetic Measurement System

We developed the system for magnetic survey by remote sensing from low altitude in the air using a drone for safe UXO detection. To determine the accurate location of UXO, it is necessary to localize a location of magnetic field source of the UXO from magnetic field distributions measured by the magnetic survey system. In addition, redundant magnetic field distributions data is necessary to perform localization by inverse problem analysis using DNN. For that reason, it is necessary to use vector magnetic sensor, and to detect sensor positions with good accuracy and to eliminate the effects of attitude changes such as drone swaying. Therefore, we mounted the 3-axis vector fluxgate on the drone and used the depth camera ZED for sensor position detection. In addition, we mounted a 9-axis sensor MPU-9250 to eliminate noise origination from the rocking and tilting of the drone, which contaminates the magnetic field data.

The system consists of the 3-axis vector-type fluxgate with sensitivity from 10 ~ 100 pT/Hz$^{1/2}$ up to 1 kHz, 24-bit ADC, Raspberry Pi3 (RPi3), the 9-axis sensor MPU-9250, Li-ion battery to drive RPi3, the depth sensor ZED. Also a drone detection system combined with the DNN for object detection is included. The magnetic field data of B_x, B_y, and B_z, which is sensed by the fluxgate, is measured by RPi3 using the 24-bit ADC. The 9-axis sensor MPU-9250 measures the drone's acceleration and angular velocity. The depth sensor ZED is combined with the DNN to detect the drone position. Both the magnetic field data and the attitude data obtained from the MPU-9250 are wirelessly transferred to another PC. If necessary, the attitude data is transferred after processing the acceleration and angular velocity data through a Kalman filter to remove noise. Using the transferred attitude data, correction of magnetic field component is performed by a C++ program developed on the PC. The drone position detection and the magnetic field measurement system combines the depth sensor ZED using the DNN to detect the drone position. When the drone enters vicinity of center of set measurement point box, it automatically measures the magnetic field. The magnetic field data is averaged by adding 10 times and the result is recorded. Combining these methods, redundant magnetic field distributions data can be obtained by using the drone to measure the magnetic field from the air, accurately detect the drone position while eliminating noise caused by the drone's rocking motion.

We mounted the above system on the drone to measure the magnetic field distributions.

3. Signal Source Localization Program

Current human-power UXO detections make it difficult to eliminate danger to inspectors. However, the danger can be reduced if the location of UXOs can be accurately localized in advance. In this study, we localize the location of the magnetic sources assuming UXO from the magnetic distributions measured by the magnetic survey system. In magnetic field measurement, it is necessary to consider the influence of noise such as vibration by drone. Therefore, using the MPU-9250 described in Chapter 2, we aim to obtain an accurate magnetic field distributions by correcting the directionality of the measured magnetic field. To localize the magnetic field source, we use a CNN (Convolutional Neural Network) for regression analysis, which is relatively robust against noise.

In order to perform inference with the CNN, it is necessary to train with training data in advance. Therefore, we determined 25 magnetic dipole locations based on actual measurement range, and virtually placed dipoles with a magnetic moment of 20 ~ 70 A/m by varying the intensity by a step of 5 A/m. We computed the magnetic field distributions for the 17,325 patterns and used them as training data. In the calculation of the magnetic dipole, we assume that the length d [m] between the N and S poles of the magnetic source is sufficiently short and has magnetic moment $m = (m_x, m_y, m_z)$(unit [Am^2]). When the length d is sufficiently short relative to the measurement point $r = (r_x, r_y, r_z)$, it can be approximated by a magnetic dipole. The magnetic field of a magnetic dipole at the origin position (0, 0, 0) is obtained by Equation (1).

$$B(r) = \frac{\mu_0}{4\pi}\left(\frac{3(m\cdot r)r}{r^5} - \frac{m}{r^3}\right) \tag{1}$$

while r is expressed by Equation (2)

$$r = \sqrt{r_x^2 + r_y^2 + r_z^2} \tag{2}$$

The distributions of $B_x, B_y, and\ B_z$ were calculated numerically using the Equations (1)-(2).

Next, we prepared correct labels corresponding to the computed magnetic fields and built the CNN to perform the training. The correct labels corresponding to the magnetic dipoles were the position of the magnetic source (x, y, z) and the magnetic moment (m_x, m_y, m_z). We prepared the 17,325 datasets. The inference performed by the system is a regression analysis, which predicts a numerical value for the magnetic field distributions. Therefore, the model was created to have the activation function of the final layer is an identity function. A diagram of the model we created is shown in Figure 1.

The training data, correct labels, and model described above were used for training. Among the training data we prepared, 10% were used as validation data, and the number of training cycles was 10,000 times.

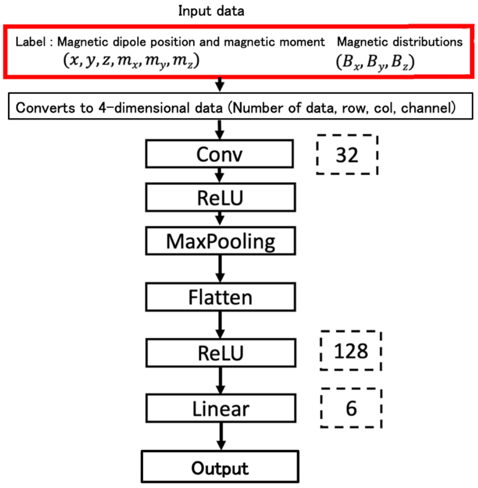

Figure 1. CNN Configuration Chart

The training results were displayed as the error between the inference results and the actual 1,732 parameters using the validation data, calculated using the root mean square error (RMSE). The RMSE can be calculated by following Equation (3). The results were obtained by inputting the 1,732 parameters for x_i and the inferred results for y_i.

$$RMSE = \sqrt{\frac{1}{n}\sum_{i=0}^{n-1}(x_i - y_i)} \tag{3}$$

As a result, the RMSE was 0.05.

4. Measurement and Source Localization of Magnet

We measured the magnetic field distributions generated by the magnet to evaluate the magnetic survey system and the signal source localization program developed in this study. We set up 25 measurement points on a 2 m x 2 m @ 0.6 m horizontal plane with 0.5 m spacing in both *x* and *y* directions. The magnetic signal source (surface magnetic flux density of approximately 630 mT) was placed at the center of the measurement plane, and its coordinate was the center at the origin (0, 0, 0) (unit [m]). We measured the magnetic field distributions at a height of 0.6 m above the ground with the magnetic source facing N-pole upward (+*z* direction). In the magnetic measurements, the background magnetic components, i.e. the geomagnetic field, were measured in advance. The geomagnetic field was approximately uniformly distributions with intensity ranging from -35.9 ~ -34.9 µT. After doing so, the geomagnetic component was subtracted from the measurement results when the magnet was installed. We created magnetic maps from the measured magnetic fields B_x, B_y, B_z at each of the 25 measurement point coordinates. The measured magnetic field distributions of B_x, B_y, B_z is shown in Figure 2, along with the calculation results (using the Equations (1) – (2)) assuming a magnetic dipole of 29.5 Am^2 at the origin. The magnetic components of the experimental and analytical results were in qualitative agreement.

Next, we inferred the source of the measured magnetic field distributions with the trained CNN network in Chapter 3. The (x, y, z) (unit [m]) coordinates and magnetic moment (m_x, m_y, m_z) (unit [Am^2]) were localized from the magnetic field distributions data of (B_x, B_y, B_z) (unit [µT]) measured by the magnetic field distributions measurement. As a result, the CNN inferred the source as $(0.00, 0.07, 0.15)$ (unit [m]) at $(0.37, 0.45, 27.76)$ (unit [Am^2]). Therefore, it can be said that the magnetic source could be localized with high accuracy.

5. Magnetization, Measurement and Source Source Localization of Magnetic Material

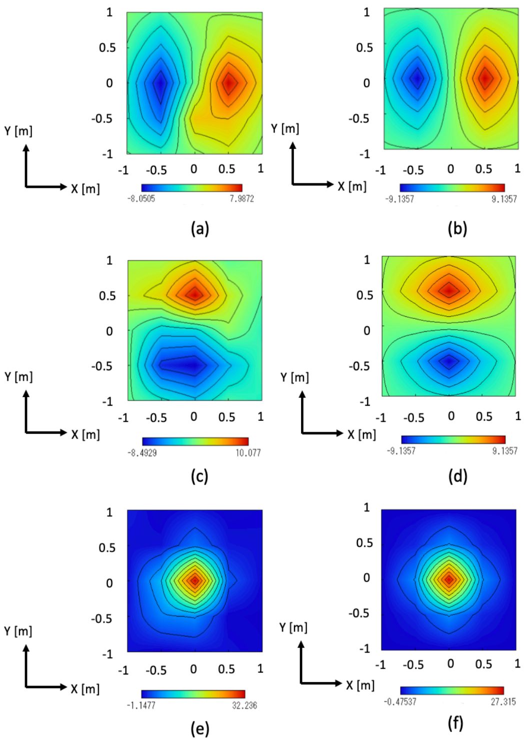

Figure 2. Contour map of fluxgate sensor measurement and simulation results

(a) Measured B_x (b) Calculated B_x
(c) Measured B_y(d) Calculated B_y
(e) Measured B_z (f) Calculated B_z

Next, we used an iron array as a magnetic material. In order to give remnant field to it, an excitation coil with 100 turns was made around the array, and 10 A DC current was applied to the coil to magnetize the iron array. The magnetization period was 1 s. The magnetized iron array was installed in the center of the measurement plane, and measurements were made in the same manner as with the magnet. The only difference was the rift-off distance of the measurement plane, which was conducted at 0.4 m in the z-direction. As a result, magnetic signal peak was measured above the array in the B_z component, and its peak value was about 5.76 μT. The measured distributions of the geomagnetic component B_z the B_z component with the magnetic material are shown in Figure 3.

Next, we inferred the source of the measured magnetic field distributions with the CNN network trained in Chapter 3. A magnetic dipole with moments of $(-0.29, 0.81, 7.06)$ (unit $[\mathrm{A/m^2}]$) at $(-0.10, -0.31, 0.14)$ (unit [m]) was inferred as a magnetic source from the magnetic field distributions, with the subtraction of the geomagnetic field. The positional errors were within about 0.3 m.

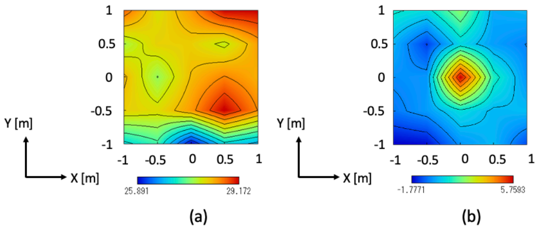

Figure 3. Contour map for magnetic measurement

(a) Geomagnetic component B_z
(b) Measured B_z distributions

6. Conclusion

In this study, we measured the magnetic field distributions from the magnetic sources and estimated the magnetic moments and locations of the signal sources using the developed magnetic survey system and signal source localization program. In the magnetic field distributions measurement, each component was in qualitative agreement with the analysis in the case of the magnet. In the signal source localization program, the positional error was within about 150 mm for the magnet, while that was within about 300 mm in the case of the magnetized material.

References

[1] Ikuo Arai, Yoshiyuki Tomizawa, Shinji Goto, “Impulse Mine Detection Radar with Array Antenna”, Measurement and Control, Volume 45, No. 6, pp498-503, 2006.

[2] P. Calou and M.Munschy, "Airborne Magnetic Surveying With a Drone and Determination of the Total Magnetization of a Dipole," IEEE TRANS.ACTIONS ON MAGN.ETICS, vol.56, no,6pp.6000409, June 2020.

[3] Seiji Masumitsu, Sunao Sadahiro, Wenxu Sun, Yoshimi Hatsukade, “Development of an Airborne Magnetic Measurement System with a High Sensitive Vector Magnetic Sensor and a Drone”, 2022-10-PEM.

[Invited Talk] Development of Antenna-Coupled Optical Modulators Using Electro-Optic Polymer Waveguides

Takahiro KAJI[1*]
[1]Advanced ICT Research Institute and Beyond 5G Research and Development Promotion Unit,
National Institute of Information and Communications Technology (NICT),
588-2 Iwaoka, Nishi-ku, Kobe, Hyogo 651-2492, Japan
*Corresponding author: kaji@nict.go.jp

Abstract – Electro-optic (EO) polymers have large EO effects and operate at ultra-high speeds of several hundred GHz or higher, so they are expected to be used in wireless-to-optical signal conversion devices in wireless communication systems such as 6G and beyond. This report describes the development of antenna-coupled optical modulators using EO polymer waveguides and non-coplanar patch antennas, and those using EO polymer waveguides, microstrip patch antennas and resonant electrodes.

Keywords – electro-optic polymer; optical modulator; radio-over-fiber

1. Introduction

In wireless communication systems such as 6G and beyond, the radio-over-fiber (RoF) technology that transmits signal waveforms of terahertz waves (0.1-10 THz) using optical fibers is expected to become important. In the RoF systems, when receiving a wireless signal from a user terminal with a remote antenna unit (RAU), or when receiving a wireless signal in a part of the wireless section of the mobile fronthaul connecting the base station and RAUs, the wireless signals must be converted to optical signals (Fig. 1).

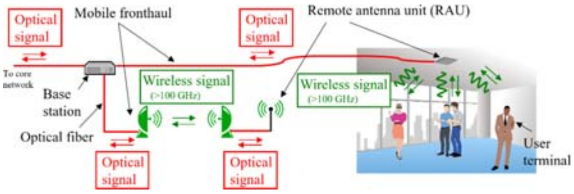

Figure 1. Schematic diagram of signal conversions expected in 6G and beyond.

To convert such a wireless signal into an optical signal, a method has been proposed in which the wireless signal is first converted to an electrical signal with an intermediate frequency using a radio frequency (RF) mixer, and then the electrical signal is converted to an optical signal using an optical modulator [1, 2]. However, these methods have problems such as a complicated mechanism, high power consumption, and high manufacturing costs. Therefore, wireless-to-optical signal conversion devices that directly convert wireless signals to optical signals without converting them to electrical signals are attracting attention. Thus far, 60-GHz-band [3], and 300-GHz-band [4] plasmonic waveguide-type electro-optic (EO) polymer optical modulators, 60-GHz-band lithium niobate ($LiNbO_3$) optical modulators [5] etc. have been reported. These devices have advantages such as a simple operating mechanism, no external power supply, and ultra-low latency. However, it is still difficult to develop devices that satisfy all requirements such as signal conversion efficiency, high-frequency operation, and mass productivity.

Aiming to resolve these issues, we are developing antenna-coupled optical modulators using EO polymer waveguides [6-8]. In this report, we will explain the EO polymer film transfer method needed to fabricate the optical modulators with suppressed high-frequency loss, and we will also describe the EO polymer optical modulators using non-coplanar patch antennas [7] and those using microstrip patch antennas and resonant electrodes [8], which are currently being developed to improve optical modulation efficiency.

2. Transfer Method of Poled EO Polymer Film

EO polymers can have large EO coefficients (r_{33} >~100 pm/V) and the large figure of merit (n^3r_{33}) for optical modulation compared with lithium niobate and realize ultra-high-speed optical modulation of several hundred GHz or more. In the conventional device manufacturing processes using the EO polymers, a device structure including an EO polymer layer, conductive clad layers, and poling electrodes is first manufactured, and then a voltage is applied to pole the EO polymer layer through the clad layers. However, it has been difficult to fabricate highly efficient devices due to the absorption of terahertz waves by the conductive cladding and constraints on the device structure due to the need for poling electrodes. Against this background, we have developed a method of transferring the EO polymer film that has been poled in advance onto a substrate and fabricated devices that combine the EO polymer film with the terahertz wave low absorption loss materials made of cyclo-olefin polymers (COPs) (Fig. 2) [9].

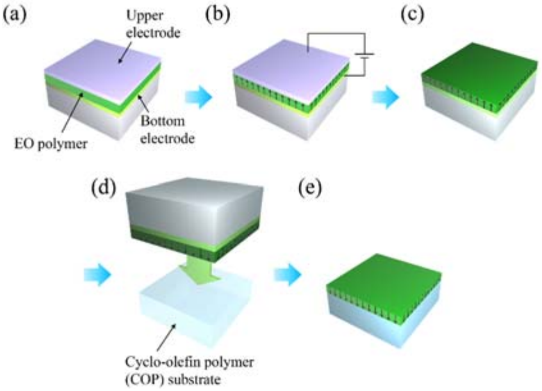

Figure 2. Device fabrication process using EO polymer film transfer method.

3. Antenna-Coupled Optical Modulators Using Non-Coplanar Patch Antennas

In our previous research, we reported W-band (75–110 GHz) antenna-coupled optical modulators with EO polymer waveguides and coplanar gap-embedded patch antennas [6]. On the other hand, in the coplanar gap-embedded patch antennas, the electric field applied to the EO polymer waveguide in the vertical direction (z-direction) was not sufficient. Therefore, with the aim of improving the electric field applied to the waveguide in the vertical direction, we proposed the devices with non-coplanar patch antennas. Figures 3(a)-(c) show schematic diagrams of the D-band (110–170 GHz) antenna-coupled optical modulators with non-coplanar patch antennas and a microscopic image of the fabricated device. The results of electromagnetic field simulations using the finite element method show that by using the non-coplanar antennas type, the electric field enhancement factor (E_z/E_0) in the vertical direction at the waveguide position is approximately 120 times, which is approximately 3 times higher than that of the coplanar antenna type [7]. Figure 3(d) shows the optical spectrum under irradiation with 150 GHz electromagnetic waves. The carrier-to-sideband ratio (CSR) during 150 GHz electromagnetic wave irradiation was 42.3 dB (irradiation power density: 34.3 W/m^2), corresponding to an optical phase shift of 15.3 mrad. Figure 3(e) shows the frequency

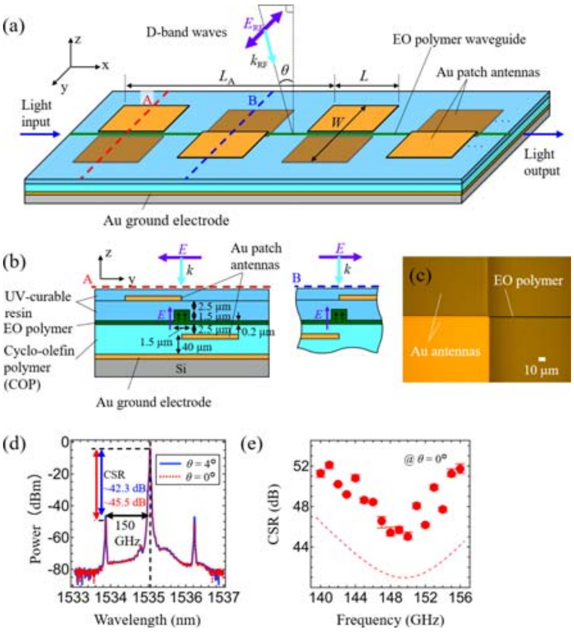

Figure 3. Schematic diagrams and microscope image of D-band antenna-coupled optical modulators using non-coplanar patch antennas and measurement results.

dependence of the CSR. The dashed line shows the value calculated assuming that the EO coefficient of the EO polymer is 36 pm/V, and it was confirmed that the calculated values roughly match the experimental values. Furthermore, toward the application of the device to wireless communication, we demonstrated carrier conversion from THz waves to dual-wavelength NIR light using a W-band EO polymer optical modulator with non-coplanar patch antennas [10].

4. Antenna-Coupled Optical Modulators Using Microstrip Patch Antennas and Resonant Electrodes

Aiming to further improve optical modulation efficiency, we prototyped D-band antenna-coupled optical modulators using EO polymer waveguides [8], microstrip patch antennas and resonant electrodes [11]. Figure 4 shows a schematic diagram of the optical modulators and an example of the results of the electromagnetic field simulations. The resonant electrode to which microstrip patch antennas are connected is placed along the EO polymer waveguide, and the standing wave electric field generated at the resonant electrode phase-modulates the light propagating in the EO polymer waveguide. As a result of electromagnetic field simulations, the electric field enhancement factor (E_z/E_0) relative to the incident electric field (E_0) at the waveguide position was estimated to be more than 130 times [8]. These results indicate that it is possible to obtain performance equivalent to or better than non-coplanar type devices even with devices having coplanar structures that can be manufactured more easily.

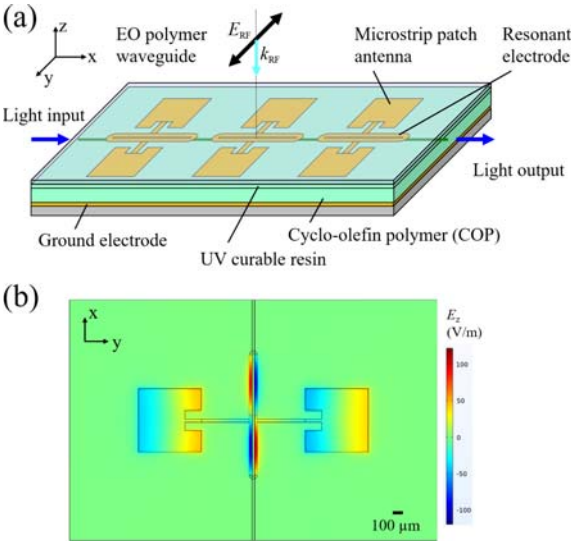

Figure 4. Schematic diagram of antenna-coupled optical modulators using microstrip patch antennas and resonant electrodes and example of electromagnetic field simulation results.

5. Conclusions

By using the transfer method of the EO polymer film, we fabricated highly efficient antenna-coupled optical modulators with EO polymer waveguides and non-coplanar patch antennas and demonstrated carrier conversion from THz waves to dual-wavelength NIR light using the fabricated device. Furthermore, we showed the possibility of a highly efficient antenna-coupled EO polymer optical modulators using microstrip patch antennas and resonant electrodes. Optimization of the antenna structures and poling process is expected to further improve optical modulation efficiency, and the device is expected to be applied to wireless communication experiments.

Acknowledgments. This research has been partly conducted under the contract "R&D of high-speed THz communication based on radio and optical direct conversion" (JPJ000254) made with the Ministry of Internal Affairs and Communications of Japan.

References

[1] Koenig S, Lopez-Diaz D, Antes J, Boes F, Henneberger R, Leuther A, Tessmann A, Schmogrow R, Hillerkuss D, Palmer R, Zwick T, Koos C, Freude W, Ambacher O, Leuthold J, Kallfass I. Wireless Sub-THz Communication System with High Data Rate. Nat. Photonics 2013; 7(12): 977–981.

[2] Nagatsuma T, Ducournau G, Renaud CC. Advances in Terahertz Communications Accelerated by Photonics. Nat. Photonics 2016; 10(16): 371–379.

[3] Salamin Y, Baeuerle B, Heni W, Abrecht FC, Josten A, Fedoryshyn Y, Haffner C, Bonjour R, Watanabe T, Burla M, Elder DL, Dalton LR, Leuthold J. Microwave Plasmonic Mixer in a

Transparent Fibre-Wireless Link. Nat. Photonics 2018; 12(12): 749–753.

[4] Salamin Y, Blatter T, Horst Y, Fedoryshyn Y, Heni W, Chelmus ICB, Baumann M, Haffner C, Watanabe T, Burla M, Elder DL, Dalton LR, Leuthold J. 300 GHz Plasmonic Mixer. Proc. 2019 International Topical Meeting on Microwave Photonics: 1–4.

[5] Murata H. Millimeter-Wave-Band Electro-Optic Modulators Using Antenna-Coupled Electrodes for Microwave Photonic Applications. J. Lightwave Technol. 2020; 38(19): 5485–5491.

[6] Kaji T, Morohashi I, Tominari Y, Sekine N, Yamada T, Otomo A. W-Band Optical Modulators Using Electro-Optic Polymer Waveguides and Patch Antenna Arrays. Opt. Express 2021; 29(19): 29604–29614.

[7] Kaji T, Morohashi I, Tominari Y, Ohara M, Yamada T, Otomo A. D-Band Optical Modulators Using Electro-Optic Polymer Waveguides and Non-Coplanar Patch Antennas. Opt. Express 2023; 31(11): 17112–17121.

[8] Kaji T, Morohashi I, Yamada T, Otomo A. Fabrication of 150-GHz-Band Antenna-Coupled Optical Modulators Using Electro-Optic-Polymer Waveguides and Resonant Electrodes. The Institute of Electronics, Information and Communication Engineers (IEICE), Society Conference September 12–15, 2023, Higashiyama Campus, Nagoya University, C-14-4.

[9] Kaji T, Tominari Y, Yamada T, Saito S, Morohashi I, Otomo A. Terahertz-Wave Generation Devices Using Electro-Optic Polymer Slab Waveguides and Cyclo-Olefin Polymer Clads. Opt. Express 2018; 26(23): 30466–30475.

[10] Matsumura Y, Tokizane Y, Hase E, Kuse N, Minamikawa T, Fujikata J, Kishikawa H, Haraguchi M, Okamura Y, Kaji T, Otomo A, Morohashi I, Kanno A, Hisatake S, Yasui T. Carrier Conversion from Terahertz Wave to Dual-Wavelength Near-Infrared Light for Photonic Terahertz Detection in Wireless Communication. Opt. Express 2023; 31(20): 33103–33112.

[11] Murata H, Miyanaka R, Okamura Y. Wireless Space-Divisionmultiplexed Signal Discrimination Device Using Electro-Optic Modulator with Antenna-Coupled Electrodes and Polarization-Reversed Structures. Int. J. Microwave & Wireless Technol. 2012; 4: 399–405.

Measurement of Antenna Radiation Pattern using Single-Cut Method with Optical Fiber

Yuanfeng SHE[1*], and Michitaka AMEYA[1]
[1]Electromagnetic Fields standards Research Group, National Institute of Advanced Industrial Science and Technology (AIST), 305-8563, Tsukuba, Japan
*yuanfeng.she@aist.go.jp

Abstract –In this paper, we introduce a simplified method for measuring antenna radiation patterns by combining the cylindrical scanning system with the single-cut method using optical fibers. The experimental setup, data acquisition process, and analysis methodology for obtaining the antenna's radiation pattern are presented. The single-cut method offers the advantage of time-saving, although it is limited to obtaining patterns in the cutting direction.

Keywords – single-cut scanning, cylindrical scanning, radiation pattern

1. Introduction

The optical fiber is a good alternative to the coaxial cable in the measurement of the antenna gains and the radiation patterns. The optical cables can reduce the influence of phase error caused by movement and loss caused by cable aging on the measurement [1-3]. Antenna radiation pattern is important in designing and evaluating of wireless communication systems. This paper introduces a simple antenna radiation pattern measurement system using the single-cut method with optical fiber. It is simplified by the cylindrical scanning device, which can greatly reduce the scanning time. Since for most antennas, we only need the radiation pattern of the main radiation direction to show its performance, this simplified setup can reduce the measurement time.

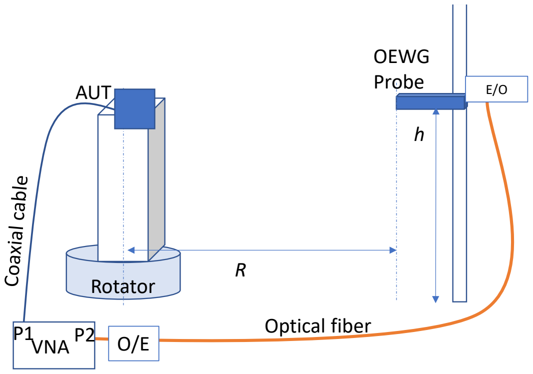

Figure 1. Setup of the measurement system.

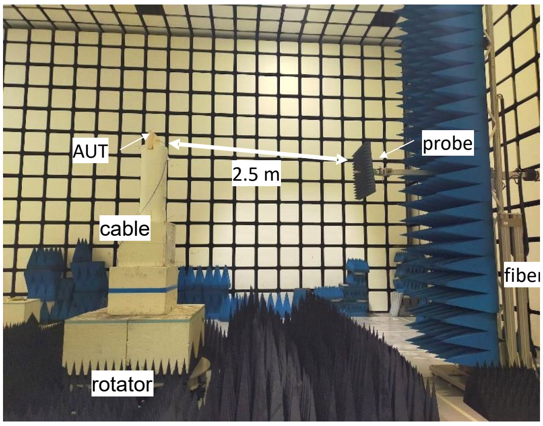

Figure 2. Photo of the measurement system.

2. Measurement System

Figure 1 shows the setup of the measurement system. It is same as the cylindrical scanning system while the height of the probe is fixed in the direction of the radiation pattern of the antenna to be measured.

Figure 2 shows the photo of the measurement system. The antenna under test (AUT) is a microstrip array antenna, size: 18 cm x 18 cm, frequency: 9.5 GHz. It is an electromagnetically long antenna. The distance of the probe to the antenna is near to the Fraunhofer distance. The main polarization of AUT is set along to the rotate direction and the height of the probe is set as same as the main beam of the AUT.

In the calculation, single-cut method uses the same algorithm with the cylindrical near field method. The far field radiation pattern of the antenna is obtained by the near-far field transformation algorithm of the cylindrical near field method while the data is filling from the data of the single-cut method.

3. Measurement Results

Figure 3 and 4 show the measured results of the radiation pattern in the main beam in main polarization and the difference near the main beam. P_{hCNF} shows the radiation pattern by the cylindrical near field method, P_{hSC} shows the radiation pattern by the single-cut method. The difference is very small in the main beam.

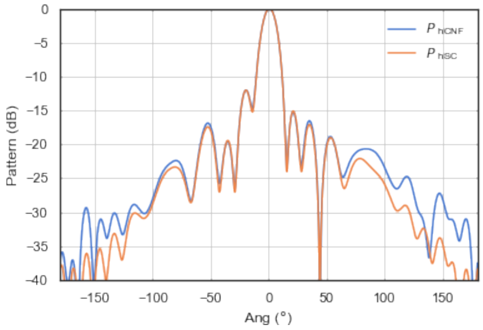

Figure 3. Radiation pattern by single-cut method and by cylindrical scanning. (Microstrip antenna, size: 18 cm x 18 cm, 9.5 GHz)

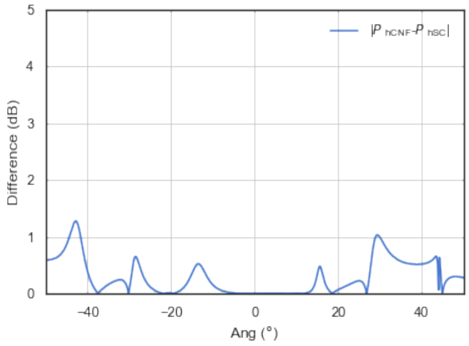

Figure 4. Difference near main beam (Microstrip antenna, size: 18 cm x 18 cm, 9.5 GHz)

4. Conclusions

This paper demonstrates the potential of employing a combination of the cylindrical near field technique and the single-cut method for antenna radiation pattern measurements. The pros and cons can by conclude as follows:

Pros:

- It effectively utilizes existing devices and can reduce modification time and cost.
- It can be used for near-field measurement of large antennas.
- It can greatly shorten the measurement time.

Cons:

- It is limited to measuring the radiation pattern of a certain plane.
- Large sidelobe errors.
- Large errors for pencil-beam radiation patterns.

These will be further study of this study.

References

[1] Kurokawa S, Hirose M, Toba Y, Antenna Measurement system Using Bi-directional Optical Fiber Link system. In Proc. EuMC 2016, Oct. 2016.

[2] Kurokawa S, Hirose M, Nishikawa K, Antenna Measurement System using Low Power Consumption Optical Fiber Link up to 40 GHz. International Symposium on Antennas and Propagation (ISAP) 2019.

[3] She YF, Ameya M, Hirose M, Kurokawa S, Hirokawa J, Ando M. Stability of Coaxial Cable Transmission and Measurement System Using Optical Fiber Link Technologies. Microwave Opt. Technol. Lett. 2017; 59(1): 201–204.

Image-Sensor-Based Microwave Electric-Field Imaging System Using LiNbO$_3$ Sensor

Kiyotaka SASAGAWA[1*], Ryoma OKADA[1], Maya MIZUNO[2], Hironari TAKEHARA[1],
Makito HARUTA[1,3], Hiroyuki TASHIRO[1,4], and Jun OHTA[1]

[1]Division of Materials Science, Nara Institute of Science and Technology,
630-0192, Ikoma, Nara, Japan
[2]Radio Research Institute, National Institute of Information and Communications Technology,
184-8795, Koganei, Tokyo, Japan
[3]Department of Opto-Electronic System Engineering, Chitose Institute of Science and Technology,
066-8655, Chitose, Hokkaido, Japan
[4]Faculty of Medical Sciences, Kyushu University,
812-8582, Maidashi, Fukuoka, Japan

*sasagawa@ms.naist.jp

Abstract –In this study, we demonstrated an electro-optic (EO) imaging system using a polarization image sensor with an *x*-cut LiNbO$_3$ (LN) crystal as a sensor for electric fields. The retardation due to the LN birefringence was corrected by the combination of λ/4 and λ/8 plates. By using an image sensor, all measurement points were measured simultaneously, and phase detection was performed by signal processing a large number of images. The electric field at 3 GHz was imaged by the proposed configuration.

Keywords – electric field imaging; image sensor; polarization image sensor; signal processing

1. Introduction

In microwave measurements, optical imaging using the EO effect has several advantages, such as less invasiveness to the electric field under observation [1, 2] and the possibility of spatially parallel measurements by using light [3].

Recently, we have proposed a method to significantly improve the detection sensitivity in image sensor-based electric field imaging by combining a unique on-pixel polarizer with a uniform polarizer [4-6]. In this technique, a polarized image sensor with a polarizer of different orientations per pixel is combined with a uniform high extinction ratio polarizer [7].

In our previous works, we demonstrated that a ZnTe crystal plate can be used as a sensor for microwave electric field distribution. However, ZnTe crystals are relatively difficult to produce in large sizes. In this study, we constructed an electric field imaging system using LN, for which the technology for manufacturing high-quality optical grade crystals is mature.

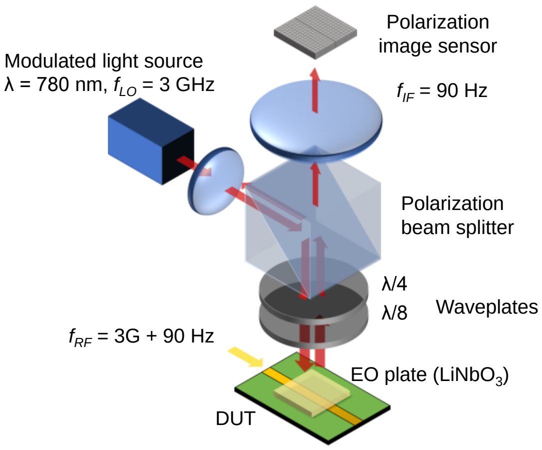

Figure 1. Schematic diagram of the proposed electric field imaging system.

2. Proposed System

LN is also widely used in waveguide optical modulators, and high-quality crystals are readily available compared to ZnTe. This advantage is significant for large-area imaging. Also, the electro-optic coefficient of the r_{33} axis is larger than that of ZnTe.

Table1. Image sensor specification

Technology	0.35-μm 2-poly 4-metal standard CMOS
Polarizer	Line/Space 0.7 μm/0.7 μm (two layers)
Pixel size	30 μm × 30 μm
Fill factor	25%
Array size	80 × 60（40 × 60 pairs）
Chip size	2.70 mm × 2.65 mm

However, the birefringence of LN should be compensated in electric field measurement systems based on the measurement of polarization rotation In order to apply our proposed high-sensitivity method, the polarization component must be greatly reduced by using a uniform polarizer. To compensate for the effect of birefringence when no electric field is applied, we used a λ/8 plate in this study.

Figure 1 shows the configuration of the optical system. The light output from the modulated light source is linearly polarized and reflected by the polarization beam splitter (PBS) toward an LN-based EO plate, which has an anti-reflection coating on its upper surface and high-reflection coating on its lower surface, and the light is transmitted through the EO plate, reflected, and returned to the PBS. The λ/4 and λ/8 plates inserted between the EO plate and the PBS transmit the light twice in the round trip. These waveplates are used to set the polarization when the light re-enters the PBS to the state with the lowest PBS transmittance. The polarization is set to the state with the lowest PBS transmittance when the light is returned to the PBS.

The PBS can be regarded as a kind of polarizer, but it is not an ideal polarizer. In this study, PBS with an extinction ratio of about 800 was used, and some polarized light with minimal transmittance was transmitted.

When an electric field is applied to the LN plate, the polarization rotates slightly, and transmittance increases. Since the direction of polarization rotation depends on the direction of the electric field applied to LN, it includes the phase information of the high-frequency electric field.

In this technique, most of the irradiated light is reflected by the PBS and does not reach the image sensor. However, the component generated by the refractive index change of LN is transmitted to the image sensor with high efficiency because its polarization direction corresponds to the high transmittance polarization axis of the PBS. As a result, this optical system increases the modulation depth of the polarization modulation signal generated by the EO plate while reducing the total light intensity. In general, image sensors are not suitable for optical measurement due to the low pixel saturation light intensity, but this method avoids the problem and allows image sensor to achieve high sensitivity in detecting polarization changes.

3. Experiment

By using the proposed system, electric field imaging was performed. The device-under-test (DUT) was a microstrip line. The EO plate crystals are 0.1-mm-thick *x*-cut LN plate, which is highly sensitive to electric field vectors parallel to the *c*-axis. It was placed to make the *c*-axis orthogonal to the line. The image sensor was a polarization image sensor in which neighboring pixels were equipped with polarizers in mutually orthogonal directions. The specification of the image sensor is shown in Table 1. The frame rate was set to 360 fps, which is much lower than microwave frequencies. To obtain images of high frequency electric field, an optical heterodyne method was used. In this experiment, a 3G + 90 Hz signal was input to the DUT, and the irradiation light was intensity-modulated at 3 GHz. The intermediate frequency component at 90 Hz was measured by the image sensor. We acquired 10,000 frames and performed phase detection for 90 Hz in each pixel. As a result, the electric field images were obtained, as shown in Fig. 2. It can be seen that electric fields exist on both sides of the microstrip line, with the center of the line as the boundary. The phases of the electric fields

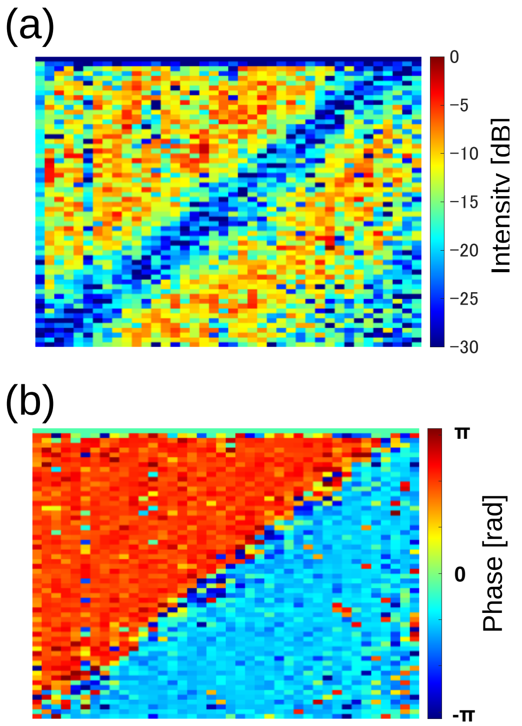

Figure 2. (a) Intensity and (b) phase images of electric filed obtained by using the LN sensor. The input signal frequency was 3 GHz. Microstrip lines were placed diagonally from top right to bottom left with respect to the imaging area. Electric field vector components parallel to the imaging plane and perpendicular to the microstrip lines were observed.

are opposite to each other, indicating that the directions of the electric fields are different.

4. Conclusion

In this study, we demonstrated that *x*-cut LN can be used for an electric field imaging system utilizing a polarization image sensor. The birefringence of *x*-cut LN was compensated by the combination of λ/4 and λ/8 plates. It is expected to be possible to expand the application to batch measurement over a wide area.

Acknowledgment

This research and development work was supported by the MIC/SCOPE #JP225007001. The chip design was supported by the activities of d-lab. VDEC, The University of Tokyo, in collaboration with Cadence Design Systems and Mentor Graphics..

References

[1] K. J. Weingarten, M. J. W. Rodwell, and D. M. Bloom, "Picosecond optical sampling of GaAs integrated circuits," IEEE J. Quantum Electron., vol. 24, no. 2, pp. 198-220, Feb. 1988.

[2] D. J. Lee, N. W. Kang, J. H. Choi, J. Kim, J. F. Whitaker, "Recent advances in the design of electro-optic sensors for minimally destructive microwave field probing," Sensors, vol. 11, no. 1, 806-824, Jan. 2011.

[3] K. Sasagawa, A. Kanno, T. Kawanishi, and M. Tsuchiya, "Novel millimeter wave near field resistivity microscope," *IEEE Trans. Microw. Theory Tech.*, vol. 55, no. 12, pp. 2782–2791, December 2007.

[4] R. Okada, K. Sasagawa, M. Haruta, H. Takehara, H. Tashiro, and J. Ohta, "A polarisation-analysing CMOS image sensor for sensitive polarisation modulation detection," *Electron. Lett.*, vol. 57, no. 12, pp. 472–474, June 2021.

[5] K. Sasagawa, R. Okada, M. Haruta, H. Takehara, H. Tashiro, and J. Ohta, "Polarization image sensor for highly sensitive polarization modulation imaging based on stacked polarizers," *IEEE Trans. Electron Dev.*, vol. 69, no. 6, pp. 2924–2931, June 2022.

[6] R. Okada, K. Sasagawa, M. Mizuno, H. Takehara, M. Haruta, H. Tashiro, and J. Ohta, "Improvement of on-pixel polarizer with 0.35 μm CMOS process for electro-optic imaging systems," *Jpn. J. Appl. Phys.*, vol. 62, no. SC, SC1052, Mar. 2023.

[7] K. Sasagawa, R. Okada, M. Haruta, H. Takehara, H. Tashiro, and J. Ohta, "Reflective high-sensitivity polarization change imaging using a dual polarizer structure," *Opt. Continuum*, vol. 2, pp. 758–768, Mar. 2023.

36-GHz electric field imaging using an electro-optic imaging system based on polarization CMOS image sensor

Ryoma OKADA[1], Maya MIZUNO[2], Hironari TAKEHARA[1], Makito HARUTA[1,3],
Hiroyuki TASHIRO[1,4], Jun OHTA[1] and Kiyotaka SASAGAWA[1*]

[1]Division of Materials Science, Nara Institute of Science and Technology, 630-0192, Ikoma, Nara, Japan
[2]Radio Research Institute, National Institute of Information and Communications Technology,
184-8795, Koganei, Tokyo, Japan
[3]Department of Opto-Electronic System Engineering, Chitose Institute of Science and Technology,
066-8655, Chitose, Hokkaido, Japan
[4]Faculty of Medical Sciences, Kyushu University, 812-8582, Maidashi, Fukuoka, Japan

*sasagawa@ms.naist.jp

Abstract – In this study, we developed an imaging system that can detect polarization modulation with high sensitivity and demonstrated the distribution measurement of a millimeter-wave electric field at 36 GHz by combining it with an electro-optic crystal using the electro-optic (EO) effect. To detect weak polarization changes caused by the birefringence of the EO crystal owing to the EO effect, we proposed a system in which a uniform polarizer is mounted directly above the polarization image sensor. We also developed a system combining an intensity modulator and a booster optical amplifier (BOA) as a local oscillator signal for optical heterodyne and demonstrated the generation of 36 GHz modulated light by DSB-SC modulation at 18 GHz. We performed the electric near-field imaging of a microstrip line at 36 GHz using the fabricated imaging system. We used a (100)-ZnTe crystal as the EO crystal and successfully obtained its intensity and phase distribution.

Keywords – Electro-optic imaging system, Polarization CMOS image sensor, On-pixel polarizer, Millimeter-wave imaging

1. Introduction

An electro-optic (EO) probe that uses the EO effect has been demonstrated as a method for detecting high-frequency electric fields [1]. The EO probe is less invasive than antenna-based electric field measurements because it does not use metal for detection. Therefore, the EO probe can visualize extremely near electric fields that are difficult to accurately measure accurately using antenna scanning. Furthermore, EO crystals have broadband characteristics up to the THz waveband [1].

Combining the EO crystal and the image sensor enables to measure the electric field distribution without probe scanning. Therefore, high-sensitivity measurement of the polarization change of polarized light irradiated on the EO crystal enables more sensitive imaging of the electric field distribution. We proposed a technique to significantly improve the sensitivity of polarization imaging using the structure shown in Figure 1 [2-5]. In this method, a uniform polarizer is stacked above a polarization image sensor, with wire-grid polarizers made of CMOS metal wiring on each pixel, resulting in a dual-polarizer structure. Figure 1 shows a reflective polarization imaging system that uses a

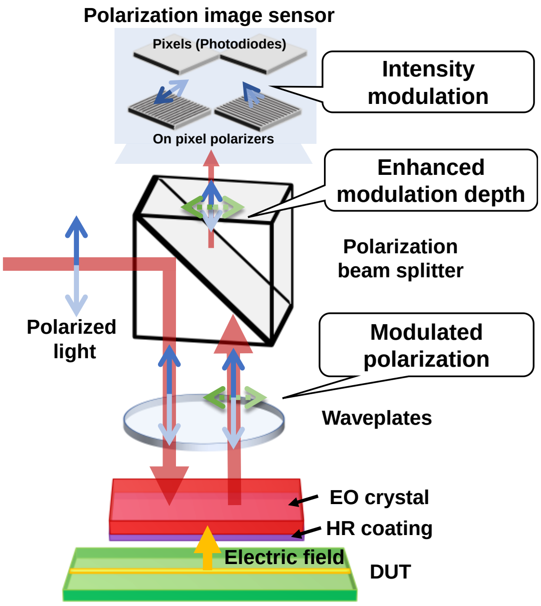

Figure 1. Conceptual diagram of an electric field imaging system based on a dual-layer polarizer

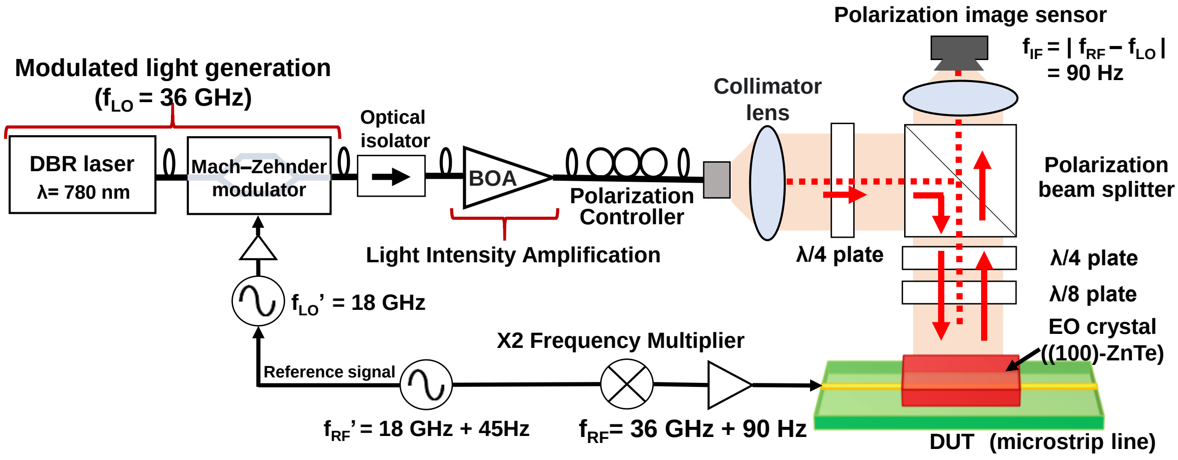

Figure 2. Conceptual diagram of an electric field imaging system.

polarization beam splitter (PBS) as a uniform polarizer and reflects the incident polarization through a high-reflection (HR) coating on the bottom of the EO crystal. This method increases the polarization modulation and reduces the incident light intensity of the polarization-modulated light transmitted through the EO crystal, enabling highly sensitive detection of weak polarization changes using a detector with low light saturation, such as an image sensor pixel.

In addition, the electric field to be imaged is significantly higher than the frame rate of the image sensor; therefore, it cannot be directly imaged. Hence, in this study, we used optical heterodyne technique with an EO crystal as a mixer to solve this problem. The optical heterodyne technique modulates the incident light intensity at the frequency of f_{LO} and irradiates it onto an EO crystal. Using the EO crystal as an optical mixer, intermediate frequency component $f_{IF} = | f_{LO} - f_{RF} |$, which is the absolute value of the difference between the frequency component f_{RF}, of the electric field under observation and the frequency of the incident light, appears in the signal. If the modulation amplitude of the incident light is constant, then the amplitude of the intermediate frequency component, f_{IF}, is proportional to the amplitude of the electric field intensity. Therefore, by observing the intermediate frequency component, information on the input signal at that frequency can be obtained. Because this technology enables to set the intermediate frequency extremely low, it can be measured using an image sensor.

In this study, we developed and demonstrated a system for imaging millimeter-wave near fields at 36 GHz with high sensitivity.

2. 36 GHz electric field imaging system

Figure 2 shows a conceptual diagram of a 36 GHz electric field imaging system based on the proposed method. The 1.55 µm band, a communication wavelength band, is often used for single-point EO measurements. However, image sensors generally comprise Si and have sensitivity from visible light to near-infrared up to approximately 1 µm. This system, used a single CW laser with a wavelength of 780 nm as the light source. A 36 GHz modulated light was generated by 18 GHz DSB-SC modulation using a LiNbO3-based Mach–Zehnder modulator (MZM), as described in detail in Section 3. The modulated light was amplified using a booster optical amplifier (BOA), and the polarization state was adjusted using a polarization controller and quarter-wave plate before entering the optical system. The incident linearly polarized light was folded back toward the EO crystal by the PBS, transmitted through the 1/4- and 1/8-wave plates, and irradiated on the EO crystal. The extinction ratio of the PBS was approximately 900. In reflective imaging based on the proposed method, light passed through each waveplate twice; therefore, the 1/4- and 1/8-waveplates acted as half- and quarter-waveplates, respectively. A microstrip line fabricated on a high-dielectric substrate was used as the device under test (DUT) for the incident electric field. The DUT was input at a frequency of 36 GHz +90 Hz using a 2x frequency multiplier, amplified using an RF amplifier, and then input into the DUT. An intermediate frequency of 90 Hz was obtained by optical heterodyne using an EO crystal as the mixer.

The polarization image sensor for electric field imaging was fabricated using a 0.35-µm 2-poly 4-metal standard CMOS process. The extinction ratio in the 780 nm wavelength band was improved to 3.3 using the second and third layers of the CMOS metal wiring of the on-pixel polarizer [4,5]. The image sensor is equipped with two types of polarizers on the pixel: one in the 0° direction and the other in the 90° direction. By considering the difference between these pairs of orthogonal polarizers, the common-mode noise component caused by the incident light could be reduced.

3. 36 GHz local oscillation modulated light generation system

To generate 36 GHz local oscillation modulated light in the millimeter-wave band, the optical modulator was supplied with 18 GHz, and DSB-SC modulation was performed by adjusting the bias point. Because the MZM used has a bandwidth of 25 GHz, 36 GHz modulated light cannot be generated using the typical method. Thus, this study used the DSB-SC modulation at 18 GHz to generate intensity-modulated light at 36 GHz. In DSB-SC modulation, the bias voltage to the MZM was set to the lowest transmittance voltage to suppress the DC component of the modulated light, thereby suppressing the carrier component and allowing only the sideband component to be obtained. This enabled to double the MZM bandwidth. Figure 3 shows the results of the modulation operation using an optical spectrum analyzer when DSB-SC modulation was performed at 18 GHz. The MZM modulated the modulated light measured by the optical spectrum analyzer that passed through an optical isolator and was amplified by the BOA. Thus, the modulated light irradiating on the EO crystal was measured. The wavelength resolution was set to 0.01 nm, corresponding to approximately 5 GHz, and notably, the 18 GHz DSB-SC modulation suppressed the carrier component and generated 36 GHz modulated light between the sidebands. Because the ratio between the sideband and carrier components was approximately 15 dB, sufficiently high optical intensity modulation was achieved. The light intensity incident on the optical system was approximately 17 mW after optical amplification using the BOA. Further increasing the intensity incident on the EO crystal is expected to improve the sensitivity of electric field imaging. Therefore, a large increase in light intensity and a significant improvement in the SNR are expected by connecting a high-power SOA or tapered amplifier in the subsequent stage.

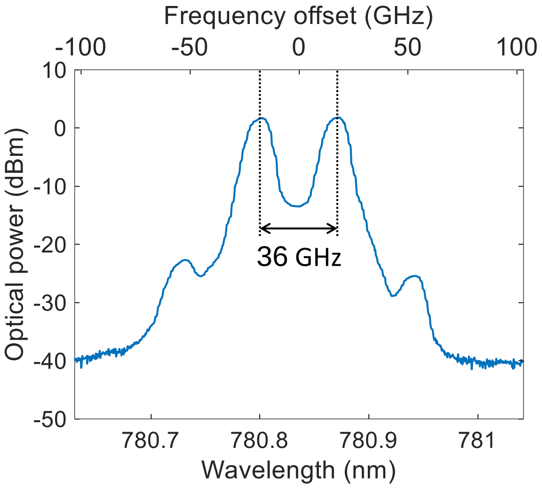

Figure 3. Optical spectra obtained from the 36-GHz optical local oscillator signal source.

4. 36 GHz electric field imaging results

The electric field imaging system shown in Figure 2 was used to image the 36 GHz near-field of the electric field above the microstrip line. The imaging was set to 360

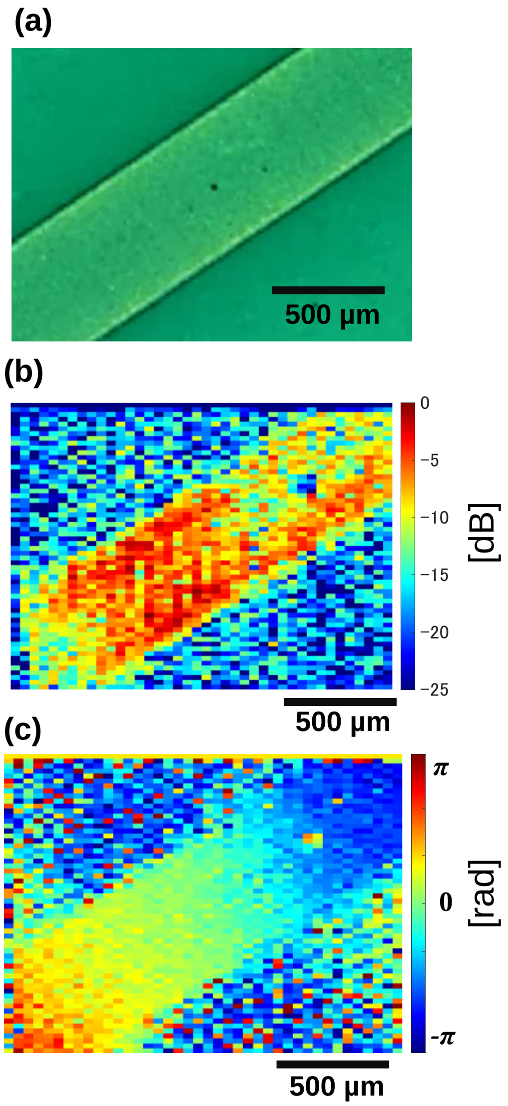

Figure 4. (a) Optical image of the DUT, (b) Intensity distribution, (c) Phase distribution.

FPS, which is four times the intermediate frequency, and the intermediate frequency component was extracted by calculating the FFT for all pixels using 36,000 frames. Figure 4 shows the electric field intensity and phase distributions. The EO crystal used was a 3 × 3 × 0.1 mm (100)-ZnTe crystal. The crystal is vertically sensitive to the electric field from the DUT. The electric field intensity on the microstrip line increased, and the phase distribution exhibited a phase shift of π rad between the inside and the outside of the line.

5. Conclusion

In this study, we developed a 36 GHz electric field imaging system using a high-sensitivity polarization imaging system based on the proposed method. We successfully generated a 36 GHz modulated light by DSB-SC modulation at 18 GHz, demonstrating a significant increase in the bandwidth of the MZM. We used an electric field imaging system to visualize the electric field in the near field directly above the microstrip line. Because EO crystals are sensitive up to the THz waveband, the wideband modulation technique is expected to be extended to the imaging of high-frequency electric fields up to the THz waveband [6-7].

ACKNOWLEDGMENT

This work was funded by the SCOPE project of the Ministry of Internal Affairs and Communications (MIC) of Japan (Grant Number #JP225007001) and supported by the activities of the d-lab. VDEC, the University of Tokyo, in collaboration with Cadence Design Systems and Mentor Graphics.

References

[1] X. Wang, Y. Cui, W. Sun, J. Ye, and Y. Zhang, "Terahertz polarization real-time imaging based on balanced electro-optic detection," J. Opt. Soc. Am. A, 27(11), 2387–2393, 2010.

[2] R. Okada, K. Sasagawa, M. Haruta, H. Takehara, H. Tashiro, and J. Ohta, "A polarisation-analysing CMOS image sensor for sensitive polarisation modulation detection," Electron. Lett., 57(12), 472–474, June 2021.

[3] K. Sasagawa, R. Okada, M. Haruta, H. Takehara, H. Tashiro, and J. Ohta, "Polarization image sensor for highly sensitive polarization modulation imaging based on stacked polarizers," IEEE Trans. Electron Dev., 69(9), 2924–2931, June 2022.

[4] R. Okada, K. Sasagawa, M. Mizuno, H. Takehara, M. Haruta, H. Tashiro, and J. Ohta, "Improvement of on-pixel polarizer with 0.35 µm CMOS process for electro-optic imaging systems," Jpn. J. Appl. Phys., 62(SC), SC1052, March 2023.

[5] K.Sasagawa, R. Okada, M. Haruta, H. Takehara, H. Tashiro, and J. Ohta, "Reflective high-sensitivity polarization change imaging using a dual polarizer structure," Opt. Continuum, 2(4), 758–768, March 2023.

[6] T. Sakamoto, T. Kawanishi, and M. Izutsu, "Asymptotic formalism for ultraflat optical frequency comb generation using a Mach-Zehnder modulator," Opt. Lett., 32(11), 1515–1517, 2007.

[7] M. Fujiwara, M. Teshima, J. Kani, H. Suzuki, N. Takachio, and K. Iwatsuki, "Optical carrier supply module using flattened optical multicarrier generation based on sinusoidal amplitude and phase hybrid modulation," J. Lightwave Tech., 21(11), 2705–2714, November 2003.

PEM 2023

5th International Workshop on Photonics applied to Electromagnetic Measurement

Technical committee on Photonics-applied Electromagnetic Measurement

https://www.ieice.org/~pem/